POLITECNICO DI MILANO
DEPARTMENT OF ENERGY
DOCTORAL PROGRAMME IN ELECTRICAL ENGINEERING

COMPUTATIONAL INTELLIGENCE FOR ELECTROMAGNETIC DRIVES

Doctoral Dissertation of:
Linh Ho Manh

Supervisor and Tutor:
Prof. Riccardo E. Zich

The Chair of the Doctoral Program:
Prof. Alberto Berizzi

Year 2014 – Cycle 27

Acknowledgements

I would like to express my dearest appreciation and thanks to my principal advisor, Professor Riccardo Enrico Zich for his patience, motivation and enthusiasm in mentoring me. Professor Zich not only gives me priceless advice to encourage my research, but also persuasively conveys me the idea of expanding my research field and I utterly appreciate that. Secondly, I would like to show my sincerest gratitude to my supervisor, Professor Piergiorgio L.E Uslenghi, whose immense knowledge and unequivocal support were invaluable to me during the time I stayed as a visiting student at the University of Illinois at Chicago. I would like to thank Professor Chien Dao Ngoc for his guidance during the time I stayed in Vietnam and his supports by sending me abroad.

I would like to thank Professor Marco Mussetta for his brilliant comments, suggestions and guidances everytime I got stuck in my analytical models. While working at University of Illinois at Chicago, I benefited of MATLAB computation scheme of spheroidal wave functions from Dr.Amir Nader Askarpour. I am grateful to the suggestions from Professor Danilo Erricolo to construct a set of Mathieu's functions and how to model a scattering problem. I would like to thank Professor Erricolo for spending his precious time in reviewing my thesis. Without their helps, a majority of this thesis would be impossible.

I am grateful to all academic and technical staffs in both Politecnico and University of Illinois at Chicago, especially Professor Francesco Grimaccia, each one of them helped me in different way. While pursuing my degree at Politecnico di Milano, this period of my lifetime was made enjoyable thanks to all my colleagues. Together with their kindness and hospitality, I did have unforgetable memories and joys from wonderful lunchtimes, coffee breaks to road trips. Last

but not least, I would like to thank my family for their abiding love in the moments when there is no one to answer my queries. Above all, this thesis is dedicated to my beloved grandpa, who rested in heaven eight years ago.

Abstract

ELECTROMAGNETIC (EM) theory, serves as an important branch of physics, and its applications are always interesting objects penetrating our daily life, from telecommunication, biology to mobile devices. Recent developments of embedded electronic system in the last several decades have shown the needs of designing and optimizing electromagnetic drives such as antennas, filters and resonators...The solution to these problems always consists of two different parts: optimization algorithms and building up representative cost function. Each cost function describes one specific electromagnetic problem, it also indicates the design constraints and how to model EM system from geometrical parameters.

In the first half of this thesis, the author concentrates on optimizing different structures from microstrip antenna and meta-material inspired antennas to frequency selective surfaces. However, when dealing with those sophisticated problems, engineers always have too many degrees of freedom to adjust. In order to tackle this issue, stochastic approach by evolutionary algorithms has been implemented. Afterwards, with the aim of fastening up the process, a surrogate-based technique by the use of Artificial Neural Network (ANN) with different training schemes has been employed. Regarding this methodology, all the EM structures have been modeled and EM fields have been calculated by full-wave analysis software. When an ANN is used as a substitution model, prior knowledge to train this adaptive system is still gained from already available full wave EM simulator.

In the world of engineering, there are a number of canonical structures and problems that can be properly described and studied with a close form analysis. Such geometries are the analysis of scattering from bodies of revolution such as

prolate and oblate spheroids. In the second half of this thesis, exact solutions for the radiation of primary sources on confocal spheroids are introduced. This typical problem of physic is interpreted by a large number of mathematical formulas and the solution seems to be very complicated. However, by using separations of variables into infinite series, abstract equations turn out to be visible. In other words, the author is trying to build the representative cost functions from the theoretical point of view. Once an exact solution is obtained, the optimization of scattered field are becomes feasible and practical effectiveness.

In the scope of this research, many techniques have been implemented , such as Particle Swarm Optimization (PSO), Genetic Swarm Optimization (GSO), Meta-PSO Artificial Neural Network and a large set of spheroidal wave functions have to be used. The properties and the use of those methods are much different from each other however they serve on purpose. Once an EM prolem is properly described, the best solution to one specific constraint should be obtained.

Summary

In recent years, wireless communication has been growing exponentially in embedded electronic systems, from cell phone, satellite mobiles to medical area. Thanks to the advantage of being small, lightweight and capable of conforming to the shape of the body, microstrip structures have been adopted successfully in the wide range of applications. In general, when designing a system, engineers always have to deal with difficult EM problems such as obtaining desired radiation pattern and usable bandwidth. Such problems require plenty of degrees of freedom to adjust; from geometrical parameters to a proper exciting source. The trade-off among those variables becomes quite complex and standard analytics or direct synthesis are often not applicable. In this context, it is reasonable to exploit the advantages of evolutionary algorithms which allow to effectively and simultaneously manage several parameters due to one specific constraint of a certain problem. Chapter 1 provides brief information about all the stochastic methods; conventional Particle Swarm Optimization (PSO), Genetic Algorithm (GA), a hybrid technique of PSO and GA namely Genetic Swarm Optimization (GSO) as well as a class of variation of PSO called Meta-PSO. All the algorithm in this discipline show a great capability of exploring solution domain without being trapped in local minima.

Chapter 2 illustrates how the heuristic optimizations have been applied to EM applications. Various types of EM structures from multilayer microstrip antenna and metamaterial inspired antenna, to frequency selective surface are optimized. In this section, all the objects have been modeled and evaluated by a commercial full-wave analysis. All the optimal designs for these structures as well as the comparison of effectiveness between algorithms have been provided rigorously.

On the other hand, the approach by full-wave simulator is always computationally expensive. In addition the dynamic memory required for each assessment is relatively big. Therefore, with the aim of reducing computational efforts and memory consumption, an equivalent surrogate model for antenna design by Artificial Neural Network (ANN) is intepreted in this thesis. All the architecture and training algorithms for ANN are discussed in chapter 1. Afterwards, ANN is used as a surrogate model to substitute completely full-wave characterization. Two different optimization schemes: Regular Sampling and Irregular Sampling are explained in detail in chapter 3, which also marks the end of the first half for this thesis.

During the first part, all the simulations of conventional scheme in chapter 2 or extracting prior knowledge for ANN in chapter 3 are based on commercial software. However, various structures in Electromagnetism, representing an indispensable part of physics, cannot be always described by simulators. This issue is more obvious in scattering problem when intepreting complex objects and materials, the use of mathematic tools is strongly needed. The research carried out in this context is a boundary-value problem where the aim is to determine radiation field of primary sources illuminating spheroidal structures. Primary sources are Hertzian electric and magnetic dipoles; spheroidal structures are two confocal prolate/oblate dielectric layers (either made of isorefractive or anti-isorefractive material) coating a metallic prolate/oblate spheroid. In order to solve the problem of dual layer coating, it is needed to impose boundary conditions on the surface of each layer. Chapter 4 brings a brief introduction of spheroidal coordinates and spheroidal wave functions such as radidal and angular functions. Chapter 5 and chapter 6 provide all the exact solutions of two problem prolate and oblate respectively. All the analytical formulations are retrieved by separations of variables, whereby the field components are expressed as infinite series of products of radial and angular spheroidal wave functions. Numerical results in these sections also exhibit the profound influences of thickness and material properties of coating layers on both far-field and near-field regions. Conclusions and discussions on the outcomes of each problem can be found at the end of each chapter.

Contents

1 Driving optimization tools **1**
1.1 Evolutionary algorithms 2
1.1.1 Particle Swarm Optimization 2
1.1.2 Genetic Algorithm 4
1.1.3 Genetic Swarm Optimization 5
1.1.4 Variations on the PSO algorithm 7
1.2 Artificial Neural Network 9
1.2.1 Neural Network architecture 10
1.2.2 Training Algorithms 12

2 Applying evolutionary algorithms in EM designs **15**
2.1 Microstrip structure 17
2.2 Dual-ring proximity coupled feed 19
2.3 Frequency selective surface as a Spatial Filter 23
2.4 Meta-material inspired antennas 32

3 Surrogate-driven optimization **39**
3.1 Regular training 40
3.1.1 Interpretation of Methodology 40
3.1.2 Numerical results 42
3.1.3 Multi ANN approach 46
3.2 Irregular training 49
3.2.1 Interpretation of the method 49
3.2.2 Applying to the case of Dual Rectangular Ring Antennas . 51

3.2.3 Optimization of Dual Annular Ring Antenna by New Scheme 52

4 Electromagnetic Modeling by the use of Special Functions 57
4.1 Introduction . . . 57
4.1.1 Introduction to Prolate and Oblate coordinates . . . 59
4.1.2 The case of one layer coating . . . 65
4.2 Dual-Layer Coating on Spheroidal Coordinates . . . 68

5 Dual-layer coating on Prolate Spheroids 71
5.1 Geometry of the problem . . . 72
5.2 Electric dipole source . . . 73
5.2.1 Interpretation of the fields . . . 73
5.2.2 Applying Boundary Conditions . . . 76
5.2.3 Exact solutions . . . 77
5.2.4 Numerical results . . . 79
5.3 Magnetic dipole source . . . 82
5.3.1 Interpretation of the fields . . . 82
5.3.2 Applying Boundary Conditions . . . 83
5.3.3 Exact solutions . . . 84
5.3.4 Numerical results . . . 86
5.4 Stochastic Optimization of the Far field . . . 89
5.4.1 Problem description and analysis . . . 89
5.4.2 Stochastic optimization and numerical results . . . 91

6 Dual-layer coating on Oblate Spheroids 95
6.1 Geometry of the problem . . . 95
6.2 Electric dipole source . . . 96
6.2.1 Interpretation of the fields . . . 96
6.2.2 Applying Boundary Conditions . . . 99
6.2.3 Exact solutions . . . 100
6.2.4 Numerical results . . . 102
6.3 Magnetic dipole source . . . 106
6.3.1 Interpretation of the fields . . . 106
6.3.2 Applying Boundary Conditions . . . 107
6.3.3 Exact solutions . . . 108
6.3.4 Numerical results . . . 110

CHAPTER 1

Driving optimization tools

The general aim of optimization algorithms is to find a solution that represents a global maximum or minimum in a suitably defined solution domain, that means to find the best solution to a considered problem among all the possible ones [1]. Traditional optimization approaches, Newton-based methods or any algorithms related to gradient descent are better known as local optimization class. Given an objective function, they can generally compute many derivatives. When dealing with a problem of many variables, those methods exhibit difficulties in finding the best solution among the Pareto domain, as reported in [2] and [3]. The techniques based on global search approaches such as evolutionary algorithms, show a great capability of finding global optimum without being trapped in local minimas and they can cope with non-linear and discontinous problems. Evolutionary algorithms apply a direct synthesis, by randomly choosing parameters of interest [4], [5]. Afterwards, the algorithm itself evolves the cost value towards the optimal solution of a specific constraint [6]. It is worth noting that fitness function is the only link between the physical model and global optimizer.

1.1 Evolutionary algorithms

Even though different evolutionary optimizations have been widely accepted for solving a number of engineering applications, it is practically impossible to define which one is the best candidate approach overpowering all the rests on any possible problem; in accordance with the *No Free Lunch Theorem* [7]. In fact, it is possible to try to understand which approach is better on the considering problem, in which the effectiveness of evolutionary algorithms is defined by the *exploitation* and *exploration* relationship kept through the run. *Exploration* ability is determined by the reliability of results and how the algorithm avoids premature convergence to local minima. *Exploitation* is the key aspect to concentrate the search effort and to reduce the number of requested fitness function evaluations. From these two perspectives, it is difficult to formulate a universal optimization algorithm that could solve effectively all problems. However, it is possible to try to make the proper choice for the considering problem

Hybridization might be the solution to this issue in terms of improving the performance and increasing the quality of solutions. In this context, an optimization technique is presented as the combination of two well-known algorithms: Particle Swarm Optimization (PSO) and Genetic Algorithm (GA). Another solution to speed up the search in solution space is by deriving a variation of conventional PSO, namely Meta-PSO. All the details of this method are described in Section 1.1.3.

1.1.1 Particle Swarm Optimization

In recent years, Particle Swarm Optimization (PSO) has gained immediate popularity [8–10]; especially because of its simplicity in implementation, its robustness and its *optimization capability* for both single objective and multi-objective problems [11,12]. PSO was proved to be in all considered cases at least comparable [15, 17], and often superior, to its most famous ancestor and now competitor, the GA [13, 14]. Besides the easiness of the implementation [16, 18], the PSO presents the advantage of being well suited for optimization problems with both discrete and continuous parameters [19, 20], and for parallel computing implementation [21–23]

The standard PSO algorithm is an iterative procedure in which a set of $i = 1, ..., N_p$ particles, or agents, are characterized by their position $\mathbf{X}_i$ and velocity $\mathbf{V}_i$ with which they move in the M-dimensional space domain $\mathcal{D}$ of a cost function $\mathcal{F}$. A full treatment of the method can be found in [10] but for sake of clarity and uniformity of notation it is briefly summarized in the following equations 1.1

and 1.2:

$$\mathbf{V}_i{}^{(k+1)} = \omega^{(k)}\mathbf{V}_i{}^{(k)} + c_1\eta_1(\mathbf{P}_i - \mathbf{X}_i{}^{(k)}) + c_2\eta_2(\mathbf{G} - \mathbf{X}_i{}^{(k)}) \tag{1.1}$$

$$\mathbf{X}_i{}^{(k+1)} = \mathbf{X}_i{}^{(k)} + \mathbf{V}_i{}^{(k+1)} \tag{1.2}$$

with $\mathbf{P}_i$ being the best position ever attained by particle i itself (personal knowledge) and $\mathbf{X}$ the best position ever attained by the particle swarm (social knowledge); $\omega^{(k)} = \omega_0 e^{-\alpha k} + \omega_1$ is a friction factor slowing down particles, η_1 and η_2 are positive parameters tuning the pulls towards the personal and global best positions, as depicted in Figure 1.1. c_1 and c_2 are random numbers of uniform distribution in the [0,1] range. The dependence of the friction factor on k was proposed in [24] starting the optimization process with a high value for k and reducing it as k increases encourages the particles to initially explore the whole space domain in the beginning, in search of the global minimum, and then allow them to better investigate the region in which this minimum is supposed to be located.

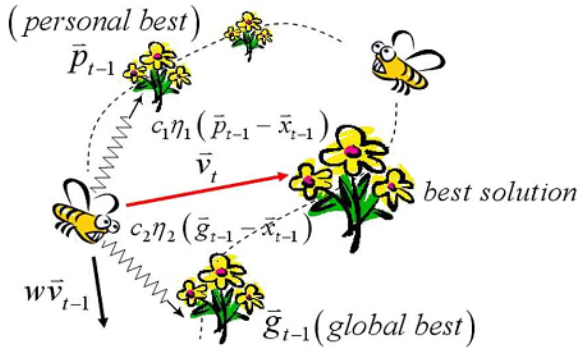

Figure 1.1: *Updating velocity rules for Conventional Particle Swarm Optimization*

An important aspect connected with the efficiency of the PSO is the way in which the particles moving towards the border of the solution space are handled. In [15] three different solutions have been proposed: the first one consists in setting to zero the velocity of the particles arriving at the domain boundary, the second one models the boundaries as perfect reflecting surfaces, so that the particles impinging on them are reflected back in the solution space; finally the third one allows the particles to fly out from the solution space, without evaluating the cost-function any more, until the particle eventually gets back in the domain. Throughout this thesis, the second technique is adopted, since trials seem to suggest that this is the one that guarantees the faster convergence, at least on problems of our interest.

1.1.2 Genetic Algorithm

One of the most effective evolutionary algorithms developed until now certainly is the GA, that is now quite popular among researchers in the electromagnetic community and widely used [25, 26]. GA simulates the natural evolution, in terms of survival of the fittest, adopting pseudo-biological operators. The set of parameters that characterizes a specific problem is called an individual, or **chromosome**, and it is composed of a list of genes. Each gene contains a suitable encoding of a parameter itself and each chromosome represents a point in the search space. For each individual of the population a fitness function is therefore evaluated, resulting in a score assigned to the individual [27, 28]. Based on these fitness scores, a new population is generated iteratively with each successive population referred to as a generation [29]. The GA uses basically three operators (selection, crossover, and mutation), as illustrated in Figure 1.2 to manipulate the genetic composition of the population.

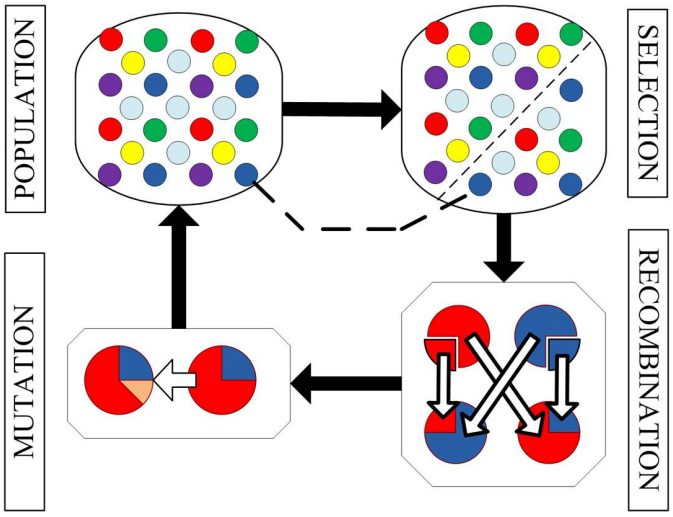

Figure 1.2: *The main operators of conventional Genetic Algorithm*

1. *Selection* is the stage of a GA in which individual chromosomes are pseudo-randomly chosen from a population for generating offsprings.

2. In *one-point crossover*, a single crossover point on both parents' chromosome strings is selected. All data beyond that point are swapped between the two parent chromosomes. In *two-point crossover*, two points are selected on each parent string. Everything between the two points is swapped between the parents. In the *uniform crossover* scheme individual bits in the

parents strings are compared and swapped with a fixed probability.

3. Mutation is analogous to biological mutation and it is used to maintain genetic diversity from one generation of a population of chromosomes to the next. The purpose of mutation is to allow the algorithm to avoid local minima by preventing the population of chromosomes from becoming too similar to each other, thus slowing or even stopping evolution being trapped in local suboptimal solution.

1.1.3 Genetic Swarm Optimization

Some comparisons of the performances of GAs and PSO can be found in literature, underlining the reliability and the convergence speed of both methods, but continuing to keep them separate [14, 16]. Both of them have shown a good performance for some particular applications [30, 31]; however we cannot choose which one outperforms the other. This is due to the different search methods adopted by two algorithms, the typical selection-crossover-mutation approach versus the velocity update one. Anyway, the population-based representation of the parameters that characterizes a particular solution is the same for both the algorithms; consequently, it is possible to implement an hybrid technique in order to effectively exploit both the qualities and uniqueness of the two algorithms.

The new hybrid approach here proposed, called **G**enetic **S**warm **O**ptimization (GSO), [33] consists in a stronger co-operation of GA and PSO, maintaining the integration of them for the entire optimization run. In this algorithm in fact, during each iteration the population is divided into two parts and it is evolved with the two techniques respectively; the two parts are then recombined in the updated population for the next iteration. After that it is again divided randomly into two parts for the next run, in order to take advantage of both genetic and particle swarm operators. Figure 1.3 show the ideas standing behind the algorithm and the way to mix the two main techniques.

The population update concept can be easily understood thinking that a part of the individuals has been substituted by newly generated ones by means of GA, while the remaining are the same of the previous generation but have been moved on the solution space by PSO. This kind of updating results in an evolutionary process where individuals not only improve their score for natural selection of the fitness or for good-knowledge sharing, but for both of them at the same time. In Figure 1.4 it is possible to better understand the key steps of the GSO algorithm through an intuitive diagram. The algorithm stops after a predefined number of iterations. In the proposed procedure, the driving parameter is introduced, called the *Hybridization Coefficient*, expressing the percentage that in each iteration evolved with GA. $hc = 0$ means the procedure is a pure PSO (the whole

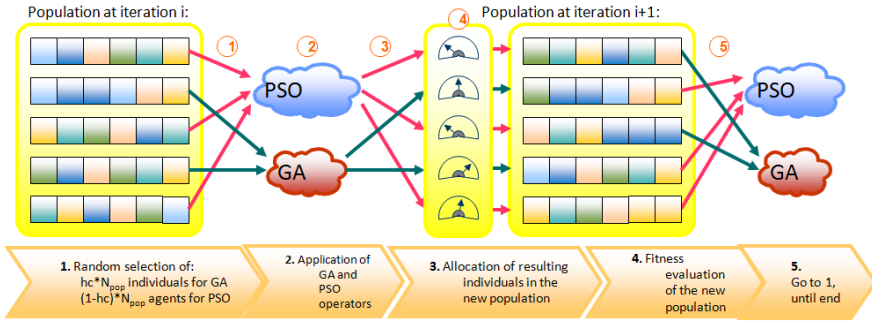

Figure 1.3: *GSO paradigm in splitting the population into subgroups during the iteration*

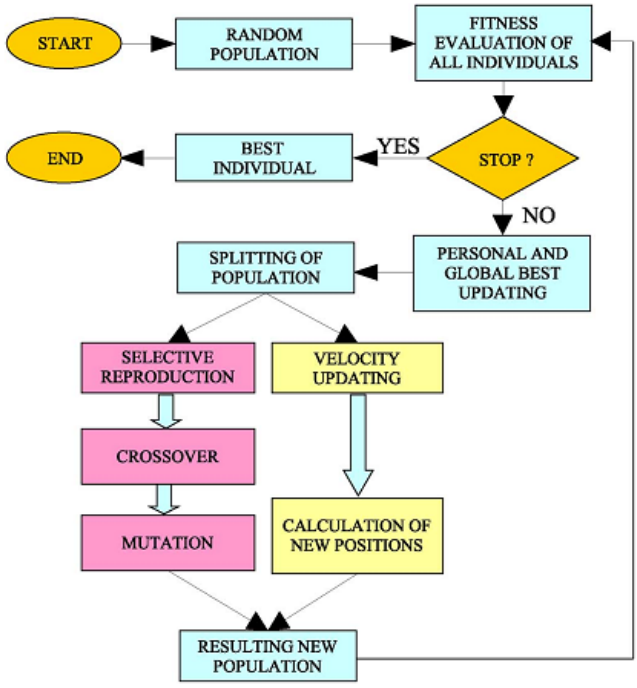

Figure 1.4: *Typical flowchart illustrating the steps of the GSO and the interactions between GA and PSO*

population is processed according to the PSO operators), $hc = 1$ means pure GA (the whole population is optimized according to the GA operators), while $0 < hc < 1$ means that the corresponding percentage of the population is developed by GA, while the rest with PSO technique. In particular, it is worth noticing

that GSO is a *self-adaptive strategy*. There are situations where a fixed *hc* is the right choice, and others where a variable $hc(i)$ during the run is better. In this thesis, the writer would like to consider two adaptive rules in order to select the best value of *hc(i)*.

The first one is the so-called *Dynamical GSO*, as referred in [32]; in this implementation the *hc* parameter is updated during iterations according to the following rule:

$$hc(i') = \begin{cases} hc(i) + \nu^{\frac{e^{-\xi\frac{i'}{N}}}{K}} & \text{if } \Delta\hat{f}(i') < \Delta\hat{f}(i) \\ hc(i) & \text{if } \Delta\hat{f}(i') \geq \Delta\hat{f}(i) \end{cases} \tag{1.3}$$

in Equation 1.3, *N* is the total number of iterations, *K* is the number of individuals in the population, $i' = i + \Delta i$, $\nu = \pm 1(versus)$, $\xi = 2(damping)$ and $\Delta\hat{f}(i') = \hat{f}(i') - \hat{f}(i)$, here $\hat{f}(i')$ is the best fitness value obtained after i' iterations and $\Delta i = 5$. The second implemented technique is the so-called *Self-Adaptive GSO*, that derives the *hc* updating rule from the traditional PSO technique: in fact, if we consider the value of $hc(i')$ in the *i'*-th iteration, then we can call $V_{hc}(i')$ the variation between *hc(i')* and *hc(i)* and so we can write:

$$hc(i') = hc(i) + V_{hc}(i') \tag{1.4}$$

Therefore, the problem is simply to find the right *velocity update* to properly change *hc(i)* during the run; following the PSO similarity, we can define a personal best P_{hc} value obtained during the run and therefore:

$$V_{hc}(i') = \omega.V_{hc}(i) + \phi.\eta.\left(P_{hc} - hc(i)\right) \tag{1.5}$$

In Equations 1.4 and 1.5, P_{hc} is chosen by analyzing the slope of fitness score during the iteration, i.e. if at the iteration $\bar{i}$ the increment of fitness is higher than in the previous history, then $P_{hc} = hc(\bar{i})$.

In [33]; preliminary results over different optimizers have been performed, showing a high effectiveness of *GSO* in exploring problem hyperspace, especially for the optimization of large objective functions. This feature makes *GSO* suitable for a wide class of electromagnetic problems.

1.1.4 Variations on the PSO algorithm

Some PSO-based techniques have been presented in [34, 35] , however their implementations are similar to Cooperative Particle Swarm Optimization [36]. In this section, three variations over the standard PSO algorithm are described. All of them use multiple swarms to enhance the capabilities of global search, but adopt different simple rules for describing the interactions among them [37, 38].

Meta-PSO

Meta-PSO (MPSO) is the most straightforward of the methods here presented and simply consists in using more than a single swarm. Particles are now characterized by two indices: an index $j = 1, ..., N_s$ defining the swarm they belong to and an index $j = 1, ..., N_{pj}$, within the swarm. For sake of simplicity in the following all swarms will be considered as having the same number of particles $N_p = N_{pj} \forall j = 1, ..., N_s$. The MPSO velocity update rule introduced in 1.6

$$\mathbf{V}_{j,i}{}^{(k+1)} = \omega^{(k)} \mathbf{V}_{j,i}{}^{(k)} + \phi\eta_1(\mathbf{P}_{j,i} - \mathbf{X}_{j,i}{}^{(k)}) + \phi\eta_2(\mathbf{G} - \mathbf{X}_{j,i}{}^{(k)}) \tag{1.6}$$

where $\mathbf{P}_{j,i}$ is the particle personal best position, $\mathbf{S}_j$ is the global best position of swarm *j* (swarm social knowledge) and $\mathbf{G}$ is the global best position of all swarms (racial knowledge), while the other symbols have the same meaning as in 1.1. Position update and boundary handling are the same as in standard PSO with just one more index.

Modified Meta-PSO

As an enhancement to MPSO aimed at keeping swarms apart from each other, and hence widening the global search, an inter-swarm repulsion is introduced and a Modified MPSO (M^2PSO) produced. The velocity update rule becomes:

$$\begin{aligned} \mathbf{V}_{j,i}{}^{(k+1)} &= \omega^{(k)} \mathbf{V}_{j,i}{}^{(k)} + \phi\eta_1(\mathbf{P}_{j,i} - \mathbf{X}_{j,i}{}^{(k)}) + \\ &+ \phi\eta_2(\mathbf{G} - \mathbf{X}_{j,i}{}^{(k)}) + \sum_{s \neq j} \phi\xi \frac{\mathbf{B}_s{}^{(k)} - \mathbf{X}_{j,i}{}^{(k)}}{|\mathbf{B}_s{}^{(k)} - \mathbf{X}_{j,i}{}^{(k)}|^{\gamma}} \end{aligned} \tag{1.7}$$

In equation 1.7 the last term is a sum of the repulsions between each single particle and all the other swarms bacycentra $\mathbf{B}_j{}^{(k)} = \left(\frac{1}{N_p}\right) \sum_{i=1}^{N_p} \mathbf{X}_{j,i}{}^{(k)}$ weighted by a random value ϕ and a fixed weight ξ. The repulsive force introduced is a function of distance according to the power γ. If $\gamma = 2$, as used here, force decays as the inverse of distance.

Stabilized Modified Meta PSO

As a further enhancement to the M^2PSO it can be ruled that the swarm which is performing best, i.e., the swarm *j* whose social knowledge coincides with the racial knowledge $\mathbf{S}_j = \mathbf{G}$, is not repelled by other swarms, or, in other words, stabilizes itself. This allows for the best swarm to keep exploring the surroundings of the current best position, refining it, whereas other swarms extend the search in other points of the space, hence greatly enhancing the possibility of escaping a local minimum. Figure 1.5 shows graphically the basics of all these algorithms.

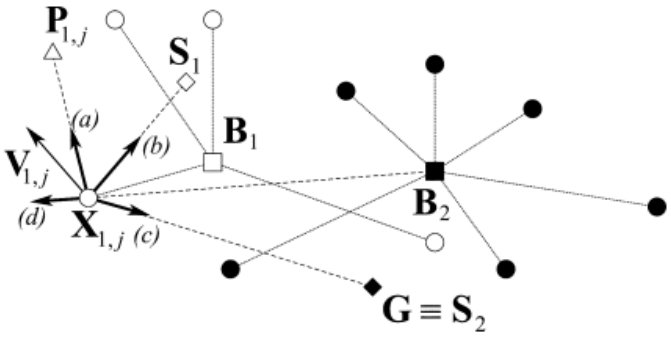

Figure 1.5: *Forces over a particle $\mathbf{X}_{1,j}$:(a) pull toward personal best $\mathbf{P}_{1,j}$; (b)pull toward swarm best $\mathbf{S}_1$; (c) pull toward global best $\mathbf{G}$ (belonging to swarm 2); (d) repulsion from the other swarm's batrycentrum $\mathbf{B}_2$*

Only two swarms are depicted, for sake of clarity. Swarm 1 is represented via white symbols, swarm 2 via black symbols. Only forces on a single particle $\mathbf{X}_{1,j}$, with velocity $\mathbf{V}_{1,j}$ belonging to swarm 1 are shown. Of course not all these forces are present, depending on the algorithm.

1.2 Artificial Neural Network

An artificial neural network (ANN) is a well known computational model that simulates the features and behaviors of human brain neurons [39, 40]. As depicted in Figure 1.6, a typical neuron collects signals from others through a host of fine structures called *dendrites*. The neuron sends out spikes of electrical activity through a long, thin stand known as an *axon*, which splits into thousands of branches. At the end of each branch, a structure called a *synapse* converts the activity from the axon into electrical effects that inhibit or excite activity from the *axon* into electrical effects that inhibit or excite activity in the connected *neurons*. When a neuron receives excitation input that is sufficiently large compared with its inhibitory input, it sends a spike of electrical activity down its *axon*. Learning occurs by changing the effectiveness of the synapses so that the influence of one neuron on another changes. Instead of dealing with a large number of integral equations like a commercial solver, after being successfully trained, ANN executes only binary blocks. As a result, a huge amount of time and computational effort are saved. Therefore, throughout this research, ANN is employed as an equivalent model in order to substitute the full-wave analysis. In order to estimate the electromagnetic field, ANN has been used rather than full-wave analysis, and

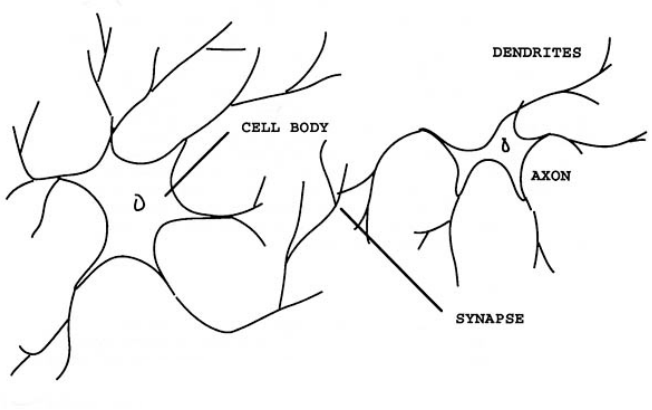

Figure 1.6: *ANN as a biologically inspired model from the human brain*

(a) Neuron model for ANN (b) Neuron as a basic component

Figure 1.7: *Adopting the idea of human brain for ANN*

good agreement was shown in [41] between the predictions and measurements. Thanks to the immense potential of ANN, it has been intensively employed in many applications such as control of non-linear system function of its parameters using Multiple Layer Perceptron Neural Network (MLP) [42] Moreover, in [43] a neural network-based solution is carried out to predict the phase characterization of reflect waves by varying the size of radiating elements.

1.2.1 Neural Network architecture

As can be seen from Figure 1.7, similar to human brain, an ANN consists of a pool of simple processing units (neurons or cells) which communicate by sending signals to each other over a large number of weighted connections, as illustrated in Figure 1.7(b). It is also known that ANN is a self-adaptive modeling tool that changes its structure on the basis of external or internal information that flow through the network during the learning phase. In many practical terms neural networks are non-linear statistical data modeling tools that can be used to build up the complex relationship between inputs and outputs.

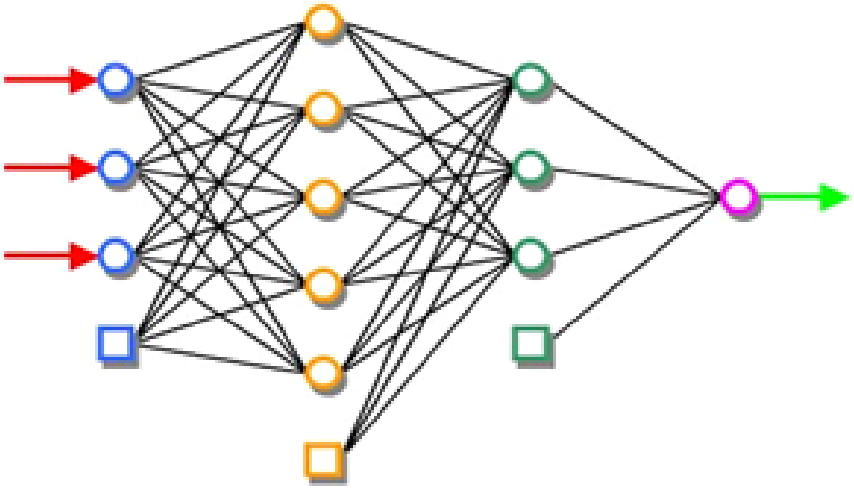

Figure 1.8: *An example of multi-layer feed-forward ANN model*

There are two types of ANN: *Feed-forward network* and *Recurrent network*. *Feedfoward* model is where the data flows strictly from the inputs to outputs whereas *recurrent* ones do contain feedback connections. The implemented ANN in this thesis is a feed-forward **multi-layer perceptron** (MLP) topology, which consists of an input layer, one or more hidden layer, and an output layer. The resulting network structure is that depicted in Figure 1.8 , where the dependencies between variables are represented by the connections among neurons. The input composition in each neuron is made by a nonlinear weighted sum:

$$f(x) = \mathcal{F}\left(\sum_j w_{jk} y_j\right) \tag{1.8}$$

Function $\mathcal{F}(x)$ in 1.8 and 1.9 is the nonlinear activation function which emulates the activity of biological neurons in the brain. This function must be always normalized and differentiable. The most common function for this purpose is the sigmoid, which is:

$$\mathcal{F}(x) = \frac{1}{1 + e^{-x}} \tag{1.9}$$

In Figure 1.8, the network comprises three inputs and one output; three hidden layers of five and three neurons respectively. Bias is added to the input and hidden layers.

1.2.2 Training Algorithms

We can categorize the learning situations in two distinct sorts. These are:

1. *Supervised learning* or *Associative learning* in which the network is trained by providing it with input and matching output patterns.These input-output pairs can be provided by an external teacher, or by the system which contains the network (self-supervised).

2. *Unsupervised learning* in which an (output) unit is trained to respond to clusters of pattern within the input. In this paradigm, the system is supposed to discover statistically salient features of the input population. Unlike the *supervised learning* paradigm, there is no *a priori* set of categories into which the patterns are to be classified, but the system has to develop its own representation of the input stimuli.

Error backward propagation

Among different learning rules, Error Back-Propagation (EBP) is a well known analytical algorithm used for neural networks training [44,45]. In literature, there are several forms of back-propagation, all of them requiring different levels of computational efforts. The conventional back-propagation method is, however, the one based on the gradient descent algorithm [46]. EBP propagates error backwards through the network to allow the error derivatives for all network weights to be efficiently computed. In other words, network weights are optimized in order to reach a good and accurate output and this objective is reached typically minimizing the mean-squared error between the output of the network, $f(x_i)$, and the target value y_i over all the N example pairs. Training is time- and memory-consuming and it is the most critical phase in the ANN setup, since it must provide continuous feedback on the quality of solutions obtained thus far [48, 49]. To test the ANN generalization capability, a Validation Set (VS) is defined too, containing known (x_i, y_i) pairs not used in the TS, in order to check the correct association between unknown input and output data. In general, Backpropagation algorithms update weights between layers based on the gradient of error function:

$$E = \frac{1}{2}\|f(x,i) - y(i)\| \tag{1.10}$$

Levenberg-Marquardt (LM) Method

EBP could be regarded as one the most significant breakthroughs for training neural networks. However, EBP is also considered not efficient because of the slow convergence when dealing with huge validation data set problems [50, 51].

There are two main reasons for this drawback: the step size is always adequate to the gradients, so when the gradient is gentle, the training process is very slow. The second reason is that the curvature of the error surface may not be the same in all directions, so the classic error valley problem may occur and may result in slow convergence [50]. This disadvantage can be greatly solved by the use of second-order derivative of total error function for weight updates. Levenberg-Marquardt has been implemented in non-linear and multi-variable optimization in recent years [51]. In this technique, the Hessian matrix gives the proper evaluation on the change of gradient vector. In order to simplify the calculating process in 1.11, the LM makes the approximation of Hessian matrix by means of Jacobian Matrix

$$H \approx J^T J + \mu I \tag{1.11}$$

where I is the identity matrix, J is the Jacobian Matrix, μ is always positive, called combination coefficient. The update rule of LM method in 1.12 can be derived as:

$$w_{k+1} = w_k - \left({J_k}^T J + \mu I\right)^{-1} J_k e_k \tag{1.12}$$

CHAPTER 2

Applying evolutionary algorithms in EM designs

In chapter 1, the brief information on theory of driving optimization tools were presented and their very preliminary results are reported in [52–54]. Most of those foregoing results are considered over the number of swarms and particles within a swarm; or the speed and reliability of convergence as a function of various parameters of the algorithms [55–57]. Most common analytical cost function in the literature is:

$$\mathbf{F}(x) = 1 - \prod_{n=1}^{N} \frac{sin(\pi(x_i - q_i))}{\pi(x_i - q_i)} \tag{2.1}$$

In equation 2.1, $\mathbf{X} = [x_1, x_2, ..., x_N]$ is a point in the *N*-dimensional solution space and $\mathbf{Q} = [q_1, q_2, ..., q_N]$ the minimum of the cost function. It is worth noting that this cost function has several local minima making the problem quite difficult to solve. The analyses carried out for Meta-PSO algorithm can be found in [37, 38], which explain clearly how the parameters affect the convergence of solutions.

Another validation of effectiveness of proposed methods is the optimization of a linear array of 100 elements. This application has been already considered in literature in order to compare different algorithms. The complex phased

array weights A_n must be determined to best meet a specified far-field sidelobe requirement. The antenna is a linear phased array of one hundred half-wavelength spaced radiators. The far-field radiation pattern to be optimized is $F.F.(\theta) = E.P.(\theta) \times A.F.(\theta)$, where

$$A.F.(\theta) = \sum_{i=1}^{N} A_n e^{j2\pi n(d/\lambda)sin(\theta)} \tag{2.2}$$

is the array factor in which the number of radiative elements and the complex elements weights to be determined. The voltage element pattern, according to [14] is assumed to be

$$E.P.(\theta) = \sqrt{cos^{1.2}\theta} \tag{2.3}$$

The cost measure in 2.3 to be minimized is the arithmetic mean of the squares of the excess far-field magnitude above the specified sidelobe level. The sidelobe mask is the same used in [14] which includes a 60 dB notch on one side. The test of GSO performance on this specific cost function can be found in [33], with good results. The literature demonstrates the ability of GSO and Meta-PSO in offering different routes through the solution hyperspace. Therefore, they appear to be promising candidates for large domain objective functions and a wide class of EM applications.

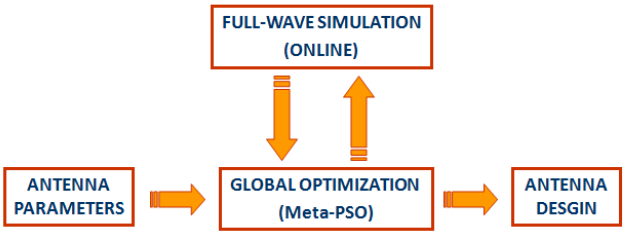

Figure 2.1: *The conventional optimization scheme with the participation of full-wave analysis*

In this chapter, several particular EM structures are optimized by proposed optimizers, all the procedures are depicted in Figure 2.1. The optimization mechanism follows exactly the same as [33, 37, 38], which is so-called **Conventional Scheme**, however there are differences in corresponding cost functions. The test cost functions are described in formulations 2.1, 2.2; in this chapter complex EM structures are built up by full-wave analysis. Assuming that an antenna has **N**-parameters to be optimized due to an objective and this antenna is represented by

a particle in **N**-dimension solution domain. Particle $\mathbf{X} = [x_1, x_2, ..., x_N]$ serves as an antenna configuration and the analysis of this structure is carried out by full-wave analysis. The outputs could be usable bandwidth or radiated far-field. As can be seen from the Figure 2.1, global optimizers can control both jobs: randomly choose antenna parameters and link with full-wave analysis. Afterwards, optimizer will evolve the whole population toward a particular constraint which is defined by engineering requirements. After a certain number of iterations, the global best configuration is obtained. The theory behind EM structures and details of numerical validation are introduced in the following.

2.1 Microstrip structure

Microstrip is one of the most planar structures, primarily because it can be fabricated by photolithographic processes and it is easily integrated with other passive devices [58]. In high-performance aircraft, spacecraft, satellite, and missile applications, where size, weight, cost, performance, ease of installation, and aerodynamic profile are constraints, low-profile antennas may be required. Presently there are many other government and commercial applications, such as mobile radio and wireless communications, that have similar specifications. To meet these requirements, microstrip antennas can be used [59]. These antennas are low profile, conformable to planar and non-planar surfaces, simple and inexpensive to manufacture using modern printed-circuit technology, mechanically robust when mounted on rigid surfaces, compatible with MMIC designs, and when the particular patch shape and mode are selected, they are very versatile in terms of resonant frequency, polarization, pattern, and impedance. In addition, by adding loads between the patch and the ground plane, such as pins and varactor diodes, adaptive elements with variable resonant frequency, impedance, polarization, and pattern can be designed [60].

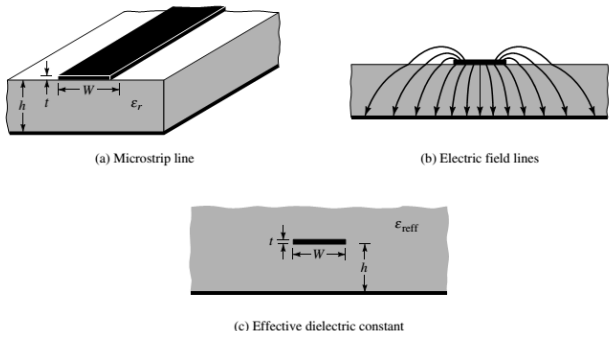

Figure 2.2: *Microstrip line and its electric field lines, and effective dielectric constant geometry.*

The typical geometry of a microstrip line is shown in Figure 2.2; with a conductor of the width W; thickness of grounded dielectric substrate d and a relative permittivity ϵ_r. The sketch of the field is also shown in Figure 2.2, the effective dielectric constant is given approximately by:

$$\epsilon_{reff} = \frac{\epsilon_r + 1}{2} + \frac{\epsilon_r - 1}{2} + \frac{1}{\sqrt{1 + 12d/W}} \tag{2.4}$$

Equation 2.4 expresses the dependence of ϵ_{reff} on the geometrical parameters. The details on characteristic impedance and attenuation can be found in [58].

There are various configurations that can be used to feed microstrip antennas. The four most popular ones are microstrip line, coaxial cable, aperture coupling and proximity coupling. The details on efficiency, usable bandwidth and feasibility of fabrication of these methods can be found in [61, 62]. Of four feeding types mentioned, proximity coupling, as a vialess multiple-layer structure, has the largest bandwidth and low spurious radiation. As illustrated in Figure 2.3, the length of feeding stub and the width-to-line ratio of the patch can be used to control impedance matching. In this thesis, two antennas of this particular type have been optimized and then they have been used as the test objects in validation of numerical techniques.

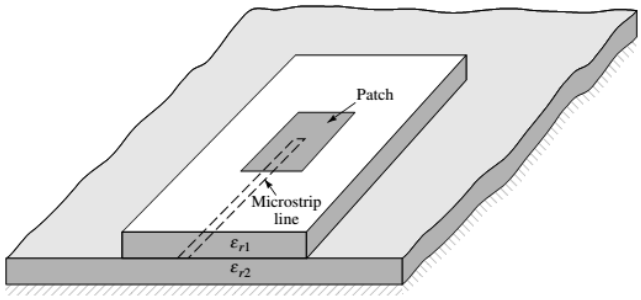

Figure 2.3: *One particular feeding structure of microstrip antennas, proximity coupling.*

There are many methods to analyze microstrip antennas. Among them, the most popular models are transmission lines and cavity, which are quite accurate and give good physical insights [59, 63]. Generally, in order to apply properly to engineering problems, full-wave analysis based on *Finite Element Method* (FEM) is highly precise and versatile. FEM approach can treat single elements, finite and infinite arrays, stacked elements and arbitrary shaped elements. In this chapter, the optimization scheme as depicted in Figure 2.1 linked with full-wave model for three complex EM structures will be discussed in detail.

2.2 Dual-ring proximity coupled feed

In antenna design, engineers always have to deal with difficult electromagnetic problems like obtaining desired radiation pattern and usable bandwidth, or ad-hoc phase and amplitude profiles. In order to properly understand and solve such problem, designers should every time adjust several degrees of freedom tuning electrical parameters and appropriately choosing the structure exciting source. The trade-off among all the degrees of freedom becomes quite complex and standard analysis or direct antenna synthesis are often not applicable. In this context, it is possible to exploit advantages of computational intelligence which allows to effectively and simultaneously manage several parameters to maximize an objective function which represents the desired configuration of a certain problem. Moreover in this discipline, Meta-PSO shows a great capability of exploring the solution domain without being trapped in local optima and the possibility of facing non-linear and discontinuous problems.

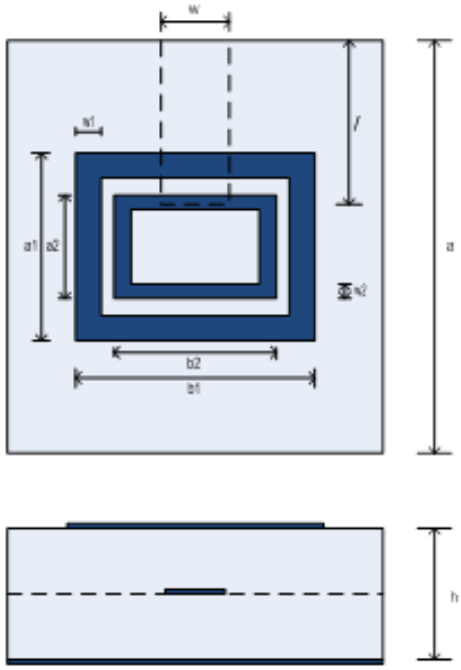

Figure 2.4: *Dual square ring proximity coupled feed antenna*

Thanks to its resonant behavior, the microstrip ring structure has been studied and applied with research interests into a wide range of applications from biomedical to satellite mobiles [3 4]. In the literature, annular patch was used as the

main radiator on the top layer and the analysis of this structure was conducted by *Method Of Moments* (MoM) approach in [60]. In this work, in order to add more degrees of freedom, we investigate the multi-layer structure with dual square ring on the top layer proximity coupled to feeding microstrip line located in the middle of the two layers has been investigated. The ground plane is situated on the bottom layer with the aim of preventing noise from the radiating patch to the circuit board behind in some specific electrical appliances. The antenna is designed to resonate at ISM band (Industrial, Scientific and Medical) where frequency ranging from 2.4 GHz to 2.48 GHz). The value of **return loss** is derived from the full-wave analysis to be used as the **merit parameter** in the cost function. With the purpose of improving resonant bandwidth over ISM band requirement, the bandwidth extension is related to cost value according to the formula:

$$Cost\ Value = 100 + BW/2 \tag{2.5}$$

Initially, one rectangular ring patch is considered; afterwards, with the aim of improving bandwidth, another ring is added in. At this point, eight geometrical parameters need to be optimized. As shown in Figure 2.4, they are: dimensions of the patch (a, b), width and length of external ring (a_1, b_1), width and length of internal ring (a_2, b_2) and thickness of the rings (t_1, t_2). Microstrip feed line is fixed with $w = 4.1mm$ and $l = 17mm$ in order to have 50Ω impedance matching. The comparison of two best solutions for two antenna configurations is shown in Figure 2.5, indicating the external ring contributes a considerable additional bandwidth to the structure. Increasing the substrate thickness could be the solution to enhance the bandwidth but it will boost up the fabrication cost as well as the whole antenna dimension. The optimal values for dual-ring proximity

Table 2.1: *Optimal solutions for 8 variables of dual rectangular proximity coupled feed antenna*

a	b	a_1	b_1	a_2	b_2	t_1	t_2
35.12	46.42	8.33	11.63	3.29	5.02	2.83	2.92

coupled fed which are found by two different operators are presented in Table 2.1. Figure 2.6 shows the radiation pattern of the optimized antenna at the center resonant frequency band, 2.45 GHz. The maximum value of gain recorded is 4 dB, satisfying the constraint for indoor electrical appliances.

Comparison on the efficiency of optimization tools

In order to investigate how the number of swarms and population for each one of them can influence results, the authors increase the whole population in Meta-Swarm. Each group now consists of 10 particles and the whole population is

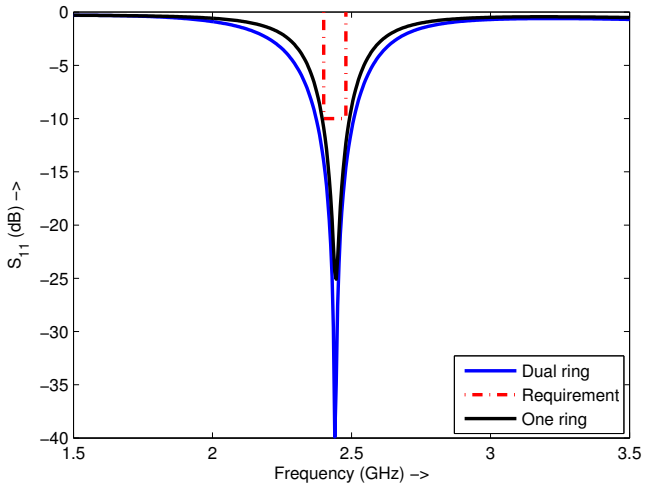

Figure 2.5: *Comparison of one ring and two ring antenna configurations over the bandwidth requirement*

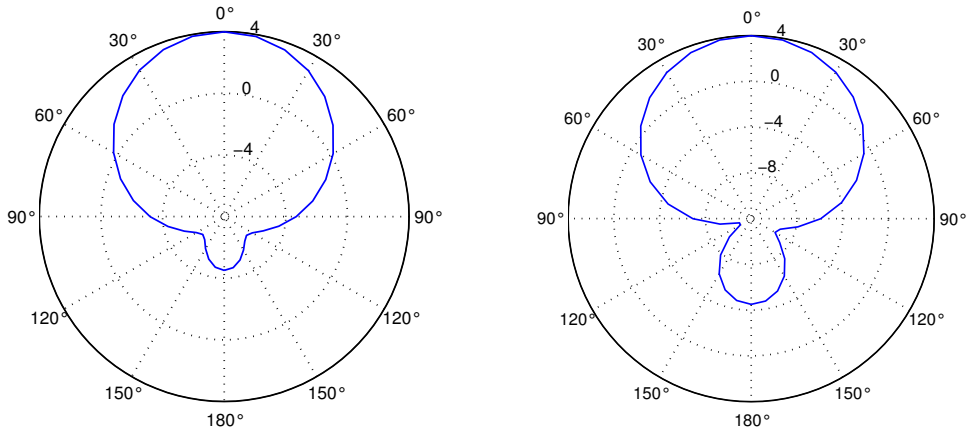

(a) xOz (b) yOz

Figure 2.6: *Radiation Pattern of the optimal antenna*

made of 100 agents. However, the optimization lasts for 6 iterations. The behavior of cost value is presented in the Figure 2.7 The result in Figure 2.8 shows the comparison of the effectiveness of two global optimizers: Meta-PSO and GSO on the same EM problem. The total numbers of particles for GSO and Meta-PSO are the same so the number of evaluations are the same too. The whole popula-

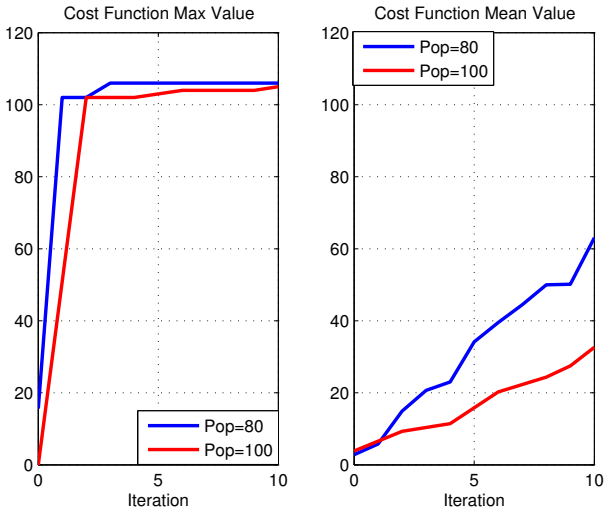

Figure 2.7: *The influence of population in the search of Meta-PSO algorithm*

tion for GSO is 100 particles with the **hybridization coefficient** $hc = 0.5$. On the other hand, population for Meta-PSO is divided into 10 swarms, each swarm has 10 agents.

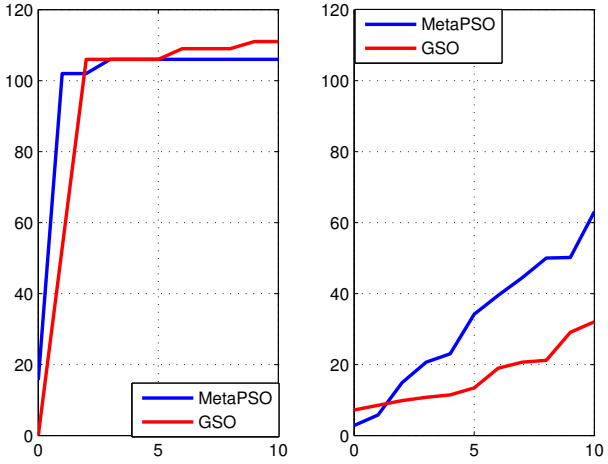

Figure 2.8: *The effectiveness of Meta-PSO and GSO in optimizing antenna structure*

2.3 Frequency selective surface as a Spatial Filter

Theory of frequency selective surface (FSS) and Floquet's theorem

Filters play an important role in electronic and radio frequency (RF) circuit, they can control the frequency content of signal for mitigating noise and unwanted interference. Once being exposed to electromagnetic radiation, a FSS behaves like a spatial filter, some frequency bands are transmitted and some are reflected. In a way, a FSS can be a cover for hiding communication facilities. This is probably the first potential application of FSS structures, as they have actually been used as covers named radomes. Radomes, in Figure 2.9, are bandpass FSS filters that are used to reduce the radar cross-section (RCS) of an antenna system outside its frequency band of operation.

Figure 2.9: *Radomes at the Cryptologic Operations Center, Misawa, Japan*

FSS, as depicted in Figure2.10, is usually a multilayer structure that comprises periodic arrays of metal patches or apertures supported by dielectric substrates [64]. As formed by planar, periodic metal-dielectric arrays in two-dimensional space, frequency behavior of an FSS can be determined by the geometry of the surface in one period (unit cell) provided that the surface size is infinite. For such periodic arrangement of the cells, **Floquet's theorem** then can be applied. Based on Floquet's theorem, any planar periodic function can be expanded as an infinite superposition of Floquet harmonics. The simplest case is 1D periodic structure, that is investigated herein by following formulas.

Considering a 1D periodic surface in x with the period d, in which $u(x)$ stands

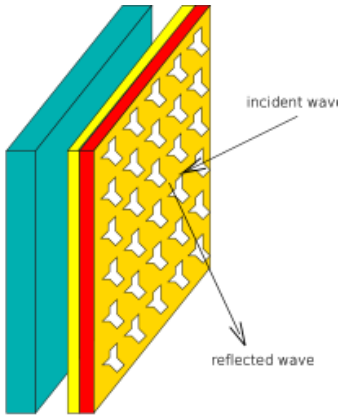

Figure 2.10: *Multi layer structure of Frequency Selective Surface*

for a field reacting with this structure.

$$\begin{aligned} u(x+d) &= Cu(x) \\ u(x+2d) &= Cu(x+d) \\ &\dots \\ &\dots \\ u(x+nd) &= Cu(x+(n-1)d) \end{aligned} \tag{2.6}$$

The formulas in equation 2.6 can be expressed generally as:

$$u(x+nd) = C^n u(x) \tag{2.7}$$

For boundedness and EM fields: $C = e^{+jkd}$. We can define a periodic function $P(x)$, where

$$P(x) = e^{-jkx}u(x) \tag{2.8}$$

Consequently from equation 2.8, we have:

$$\begin{aligned} P(x+d) &= e^{-jk(x+d)}u(x+d) = e^{-jk(x+d)}Cu(x) = e^{-jkx}e^{-jkd}\left(e^{jkd}\right)u(x) \\ &= e^{-jkx}u(x) = P(x) \end{aligned} \tag{2.9}$$

Similarly, $P(x+nd) = P(x)$

1. P(x) is a periodic function in x, with the period d
2. Since $P(x)$ is periodic in x, we can express it via Fourier Series

$$P(x) = \sum_{n=-\infty}^{\infty} p_n e^{j\frac{2\pi n}{d}x} \tag{2.10}$$

Substituting equation 2.8, then

$$u(x) = \sum_{n=-\infty}^{\infty} p_n e^{jk_{x_n}x} \tag{2.11}$$

in which:

$$k_{x_n} = k + \frac{2\pi n}{d} \tag{2.12}$$

Equation 2.12 represents harmonic expansion of the field $u(x)$, each term in 2.11 stands for a spatial *Floquet Harmonic*, which propagates along the periodic axis. Here it is presented for a 1D periodic structure. It can be easily generalized to higher dimensions with more complex periodicities.

Optimizing spatial bandstop filter by means of Meta-PSO

In this context, Floquet Theorem is applied exclusively for planar periodic structures which are idealized as infinitely large. The analysis of these structures is then accomplished by analyzing one unit cell. The relative positions of the periodic points are specified by lattice vectors, as illustrated in Figure 2.13. These vectors describe the geometry of arrray but they are independent of the nature of array elements themselves. Different distribution of unit cells means different lattice vectors, therefore FSS structures will return diverse frequency responses.

Patch type in Figure 2.11(a) has capacitive response so it acts like low-pass filter. Instead, slot type in Figure 2.11(b) has inductive response so it acts like a high-pass filter. The idea is to combine both inductive and capacitive responses to retrieve a specific prohibited band.

In the restricted scope of this research, all the unit cells are square and they are placed uniformly as Figure 2.13(a). Regarding the angle of incidence, FSS structure is illuminated by plane waves with propagation direction normal to the planar surface and no phase delays are introduced between adjacent elements.

In [64], several loop types of FSS including one rectangular ring are studied to construct different radio frequency applications. Over the years, a variety of FSS elements were introduced for bandpass and bandstop applications. A complete list of these elements includes an array of the following: circular shapes; metallic plates such as rectangles and dipoles, cross-poles, tripoles, and Jerusalem cross; three- or four-legged dipoles; rings; square loops; and grid square loops, as shown in Figure 2.12.

In this study, a dual rectangular ring configuration is considered for WiFi bandstop filter, from 2.4 to 2.5 GHz. With the aim of increasing bandstop region over the requested one, one ring is added. As shown in Figure 2.14, the solution domain consists of 7 variables: a,a_1, b_1, t_1, t_2, a_2 ,b_2; which are properly modeled

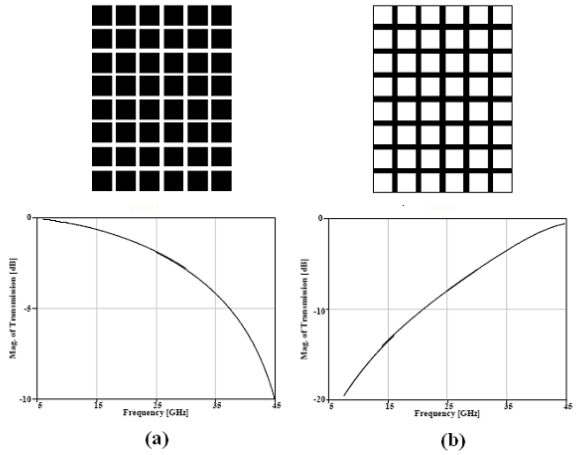

Figure 2.11: *(a) Patch type has capacitive response whereas (b) Slot type has inductive response*

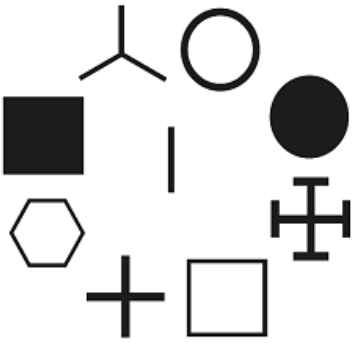

Figure 2.12: *A variety of FSS elements over the past decade*

to satisfy the feasibility of fabrication. For instance, two rings cannot overlap each other or the outer ring cannot exceed the dimension of the patch. The planar periodic stucture is printed on FR4 substrate with ε_r = 4.4 and 0.8 mm in height.

FSS structures are modeled by full-wave analysis and the objective of optimization is compressed into a representative cost function. The optimization scheme is the same as the scheme in Figure 2.1, but now FSS parameters need to be optimized. In this case, the main objective is to enlarge as much as possible the bandstop bandwidth over selected WiFi band (2.4-2.5 GHz). As illustrated in Figure 2.15, firstly, each set of geometrical parameters stands for one specific FSS

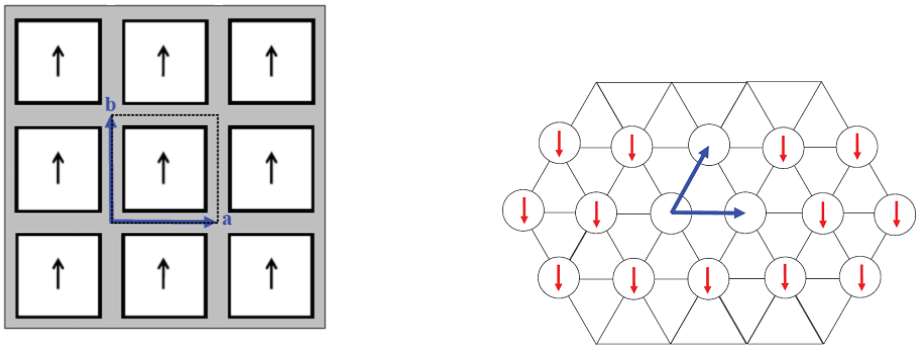

(a) 90 degree (b) 60 degree

Figure 2.13: *Organizing FSS as a planar periodic struture*

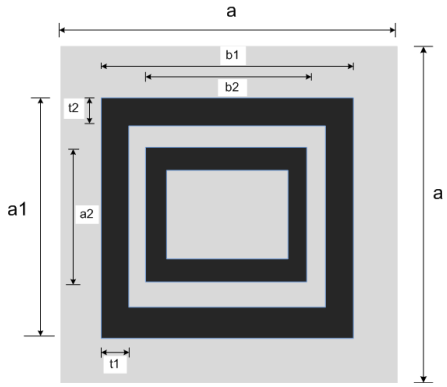

Figure 2.14: *Top view of dual rectangular ring unit cell*

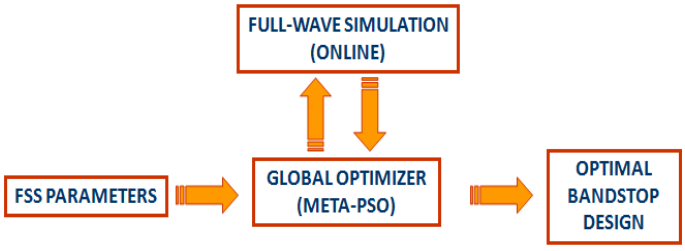

Figure 2.15: *The block diagram of optimization scheme.*

configuration. For each iteration of optimization loop, this set of data is varied by global optimizer and what full-wave simulation returns will be used to evaluate

the structure. After a certain number of loops, the optimal design is retrieved.

Numerical results

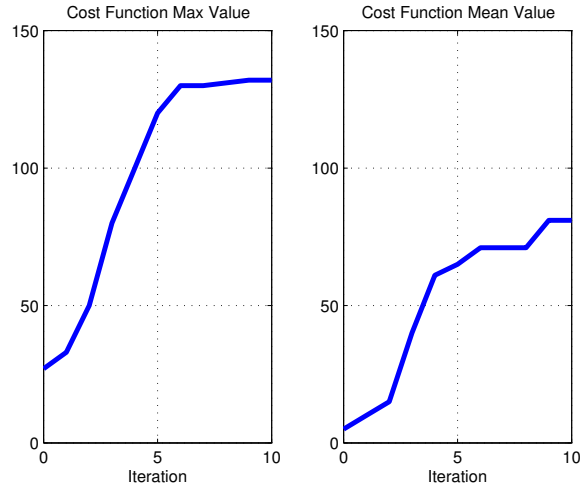

Figure 2.16: *The Max and Mean Value throughout 10 iterations*

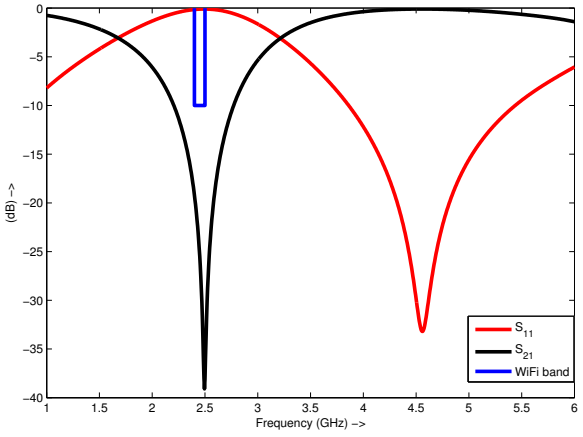

Figure 2.17: *Frequency response of best configuration ever found by optimizer*

Since the width and length of two rectangular rings and substrate patch play an important role on scattered field of FSS structure, they are modeled as variables in optimization scheme. Each set of parameters constructs an antenna configuration,

and then each antenna configuration stands for one agent in the swarm. In this context, total population consists of 90 particles, 9 agents in each 10 swarm.

Table 2.2: *Optimized geometrical parameters by Meta-PSO*

Parameter	a	a1	b1	t1	t2	a2	b2
Values	36.694	27.456	27.659	0.756	1.929	8.699	10.071

Considering FSS as a filter, S_{21} serves as transmission coefficient and S_{11} as reflection coefficient. When behaving bandstop characteristics, the requirements of $S_{21} < -10$ dB and $S_{11} > -1$ dB should be fulfilled. They are also fundamental conditions to determine cost value, which then they are evaluated by global optimizer. In order to enlarge the bandstop region, the extension of prohibited bandwidth (BW) is related to cost value according to the formulation:

$$\text{Cost Value} = 100 + BW/2 \tag{2.13}$$

In Figure 3.10, the change of max values and mean values of cost function shows the fundamental characteristic of heuristic approach: the swarm improves itself during optimization time. Frequency response of best configuration ever found by Meta-PSO is shown in Figure 2.17 and details of parameters are presented in Table 2.2.

911 simulations were evaluated by Meta-PSO optimizer in approximately 35 hours. Commercial full-wave analysis has been implemented on an Intel(R) core I-7 2600 CPU, 3.4 GHz, 8 GB Ram system.

Extension of the case: Bandpass spatial filter

As mentioned in Figure 2.12, FSS structures have been considered as periodic arrays of special elements. In general, FSS can be categorized into two major groups: *patch type* and *aperture type*. Once hit by plane wave, patch-type FSS behaves as a capacity surface which has the characteristics of a low-pass filter. This architecture transmits low-frequency content of the wave and reflects the higher pattern. Instead of that, aperture-type FSS, as a complementary structure, has an inductive response, and acts like a high pass filter.

Therefore, in order to manipulate both inductive and capacitive responses of patch-type and array-type, dual-rectangular ring configuration was utilized to produce bandstop filter. In this section, in order to create a **reverse behavior** of a bandpass filter, the idea is to make a **reverse structure**. Instead of printing two rectangular rings on a substrate, two rectangular slot rings are made on a printed

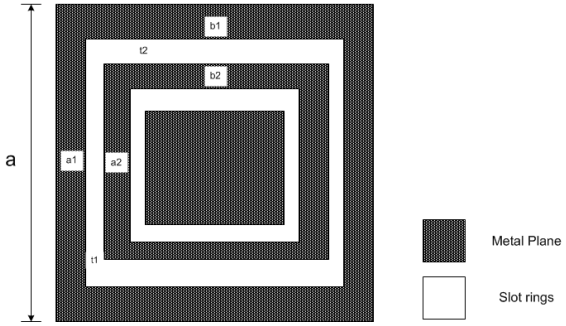

Figure 2.18: *Geometrical parameters of optimizing spatial bandpass filter*

metal plane. The mechanism of optimization from integration of full-wave analysis and global optimizer to modeling geometrical parameters follows exactly what explained in Figure 2.15. The details of seven geometrical parameters on a square unit cell are depicted in Figure 2.18.

Similar to bandstop design, all the unit cells are square and they are placed uniformly as Figure 2.13(a). Regarding the angle of incidence, FSS structure is illuminated by plane waves with propagation direction normal to the planar surface and no phase delays are introduced between adjacent elements. In this study, a dual rectangular ring configuration is considered for WiFi bandstop filter, from 2.4 to 2.5 GHz. With the aim of increasing bandstop region over the requested one, one ring is added. As shown in Figure 2.18, the solution domain consists of seven variables: a,a_1, b_1, t_1, t_2, a_2 ,b_2; which are properly modeled to satisfy the feasibility of fabrication.

FSS structures are modeled by full-wave analysis and the objective of optimization is compressed into a representative cost function. The optimization scheme is the same as the scheme in Figure 2.1, but now FSS parameters need to be optimized. In this case, the main objective is to enlarge as much as possible the **bandpass** bandwidth over selected WiFi band (2.4-2.5 GHz). As illustrated in Figure 2.18 , firstly, each set of geometrical parameters stands for one specific FSS configuration. For each iteration of optimization loop, this set of data is varied by global optimizer and what full-wave simulation returns will be used to evaluate the structure. After a certain number of loops, the optimal design is retrieved.

The width and length of two rectangular rings and substrate patch have been introduced again modeled as variables in the optimization scheme. Each set of parameters constructs an antenna configuration, and then each antenna configuration stands for one agent in the swarm. In this context, total population consists of 90 particles, 9 agents in each 10 swarms.

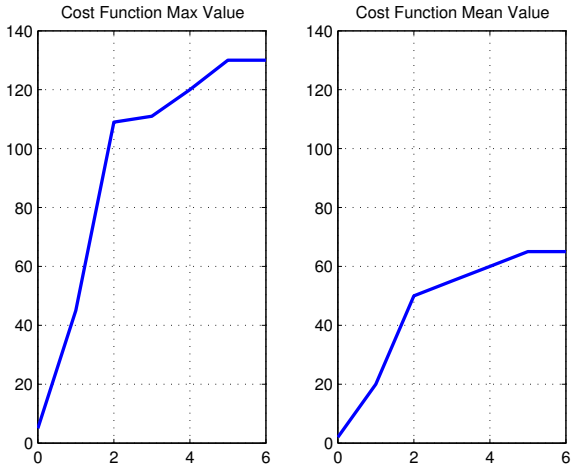

Figure 2.19: *The Max and Mean Value throughout 10 iterations*

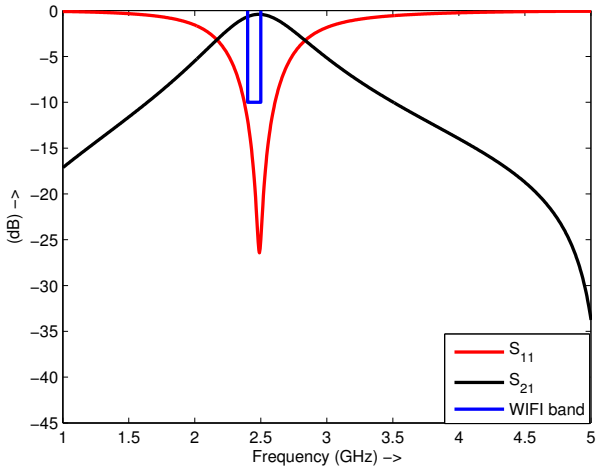

Figure 2.20: *Frequency response of best configuration ever found by optimizer*

Table 2.3: *Optimized geometrical parameters by Meta-PSO*

Parameter	a	a1	b1	t1	t2	a2	b2
Values	39.76	27.43	26.09	1.38	1.19	13.857	11.06

Considering FSS as a filter, S_{21} serves as transmission coefficient and S_{11} as reflection coefficient. When behaving bandpass filter, the requirements of

$S_{11} < -10$ dB and $S_{21} > -1$ dB should be fulfilled. They are also fundamental conditions to determine cost value, which then are evaluated by global optimizer. In order to enlarge the bandstop region, the extension of **permitted bandwidth** (PBW) is related to cost value according to the formulation:

$$\text{Cost Value} = 100 + PBW/2 \tag{2.14}$$

In Figure 2.19, the change of max values and mean values of cost function shows the fundamental characteristic of heuristic approach: the swarm improves itself during optimization time. Frequency response of best configuration ever found by Meta-PSO is shown in Figure 2.20 and details of parameters are presented in Table 2.3.

2.4 Meta-material inspired antennas

Theory of pure left-handed material

In the last few years, there has been an increased interest in the scientific community in the study of metamaterials. Metamaterials are a class of composite materials artificially constructed to exhibit exceptional properties not readily found in nature. In particular, there has been high level interest in studying materials which can be characterized by simultaneously negative permittivity (ϵ) and permeability (μ) over a certain frequency band. Such material can be called **left-handed** material or **anti-isorefractive** material. In this context, a brief but sufficient introduction on the EM properties of propagation, radiation and scattering of left-handed material has been provided. Throughout this thesis, all the medias are assumed to be homogeneous and isotropic. The characteristics of **anti-isorefractive** structure will be again discussed in Chapters 4, 5 and 6. It is useful to review the simple concept of wave propagation in a source-free unbounded medium. For such a medium, propagating waves obey the frequency domain Maxwell's curl equations, which are given by:

$$\nabla \times \bar{E}(\bar{r}) = i\omega\mu(\omega)\bar{H}(\bar{r}) \tag{2.15}$$

$$\nabla \times \bar{H}(\bar{r}) = -i\omega\epsilon(\omega)\bar{E}(\bar{r}) \tag{2.16}$$

where $\epsilon(\omega)$ and $\mu(\omega)$ are frequency dependent. For plane wave solutions of the form $e^{i\bar{k}.\bar{r}}$, Maxwell's equations become,

$$\bar{k} \times \bar{E}(\bar{r}) = \omega\mu(\omega)\bar{H}(\bar{r}) \tag{2.17}$$

$$\bar{k} \times \bar{H}(\bar{r}) = \omega\epsilon(\omega)\bar{E}(\bar{r}) \tag{2.18}$$

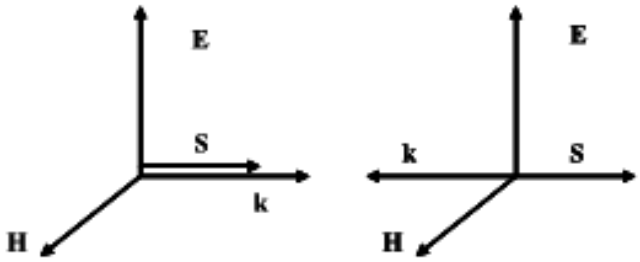

Figure 2.21: *Illustration with Transverse Electromagnetic Wave*

where $\bar{k}$ is the wave propagation vector and together with $\bar{E}$, $\bar{H}$, they form **left-handed system**. Considering an electric field that is polarized along the $\hat{\rho}$, the power flow can be calculated as follows, according to Poynting's Theorem:

$$\bar{E} = \hat{\rho} e^{i\bar{k}.\bar{r}} \tag{2.19}$$

$$\bar{H} = \frac{1}{\omega\mu}\left(\bar{k} \times \bar{\rho}\right) e^{i\bar{k}.\bar{r}} \tag{2.20}$$

$$\begin{aligned} \Longrightarrow \left\langle \bar{S} \right\rangle &= \Re\{\bar{E} \times \bar{H}\} = \frac{1}{\omega\mu}\hat{\rho} \times \left(\bar{k} \times \bar{\rho}\right) \\ &= (\hat{\rho}.\hat{\rho})\hat{k} - (\hat{\rho}.\hat{k})\hat{k} \\ &= \frac{\bar{k}}{\omega\mu} \end{aligned} \tag{2.21}$$

where $\Re$ is the real operator and $\hat{\rho}.\bar{k} = 0$ is due to Gauss's law. This result shows that the time-averaged Poynting vector will be in the opposite direction of the phase propagation vector where ϵ and μ are both negative, as illustrated in Figure 2.21.

Realization of Meta-Material inspired antennas

In recent years, as wireless communication technologies are growing exponentially, multi-band antennas for WLAN (Wireless Local Area Network) and WIMAX (World Wide Interoperability for Microwave Access) received a lot of interest [65]. In order to reduce the size of EM devices, Meta-Material (MTM)-inspired structures have been employed extensively by the relization of SRR or composite right-left handed (CRLH) transmission line [66–68]. However, these designs intrinsically suffer the drawbacks of narrow bandwidth and difficult fabrication. In this dissertation, two vialess microstrip antennas will be proposed by the combination of many techniques namely: SRR or CSRR, truncated ground plane and

Coplanar Waveguide (CPW)-fed. These configurations have been properly modeled by full-wave analysis, and then they have been optimized by the a global optimizer, Meta-PSO.

In the literature, Split ring resonator (SRR) and complementary split ring resonator (CSRR) have been widely used to reduce the antenna size. In order to exibit the robustness of global optimizers and new designs of Meta-Material inspired antenna, in this thesis, complete solutions for two vialess coplanar-fed antenna will be presented. Two multiple-band antennas are electrically small (20mm x 20mm x 1.6mm) and operate at Wifi band (2.45 GHz/5.2 GHz) as well as WIMAX at 3.5 GHz. Antenna structures are modeled by full-wave analysis and then compressed into a representative cost function. The optimization scheme used is fully described by Figure 2.1. In this context, the main objective is to enlarge as much as possible the resonating bandwidth over three selected bands: Wifi1 (2.4-2.5 GHz), Wifi2 (5.1-5.8 GHz) and WIMAX (3.4-3.7 GHz).

Meta-Material, as an artificial material, possesses many intriguing properties that can be exploited in miniturizing antennas since the operating frequencies are independent of electrical length. The idea is to create a multi-resonant structure with improved bandwidth response by imposing SRR (or CSRR) and CPW-fed. This multi-band design can be realized by the use of equivalent circuits, however L-C lumped elements are usually obtained through via-hole components [69], [70]. By adopting the ideas of vialess structure presented in [71], two striplines connected to the edge of substrate are created. These configurations, by a proper design, can perform equivalently with the via or multi-layer structures. Coplanar waveguide has been employed as feeding instead of conventional microstrip line thanks to the possibility of enhancing the bandwidth [72]. Since the antenna is the combination of many specific designs, the influence and coupling effects of one part on the others are remarkable. It is relevant to derive a solution by a stochastic approach based on the hypothesis of MTM-inspired structures. All the top view, side view and 3D layout of two proposed antennas are denoted in Figure 2.22 and Figure 2.23.

Regarding the substrate, all the elements are printed on FR4 proxy with thickness h = 1.6mm and dielectric constant of 4.4. All the geometrical parameters from the dimensions of CPW feed structure, split ring resonators, width and length of connected arms are varied. The truncated ground plane is placed on the bottom layer, paralel with the structures on the top plane. This patch can be placed symmetrically or asymmetrically to the center point of concentric split rings. The purpose of this design is to create the equivalences of lumped inductors and capacitors for multi-band structures. The second stage of feed line connecting external split ring to internal split ring is decreased in size. Since the aim is to minimize the size of antennas, the range or variation of all the parameters are

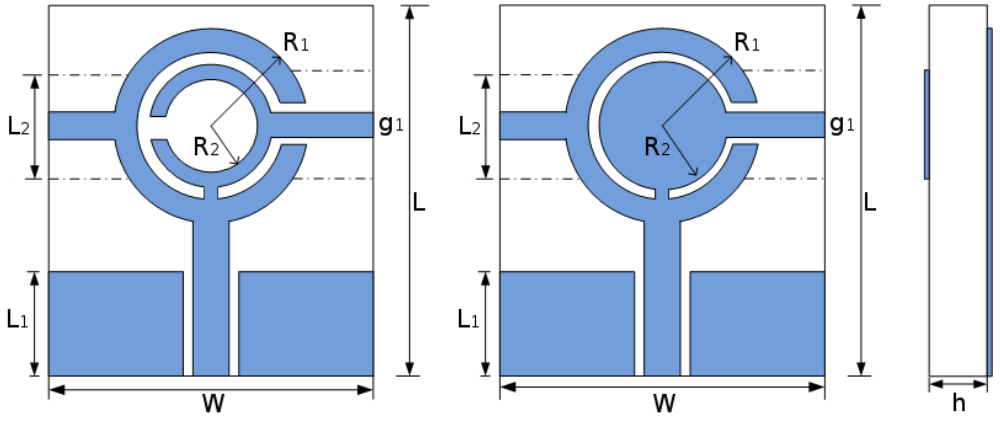

(a) Protoype 1 (b) Prototype 2

Figure 2.22: *Top view and side view of MTM-inspired antennas.*

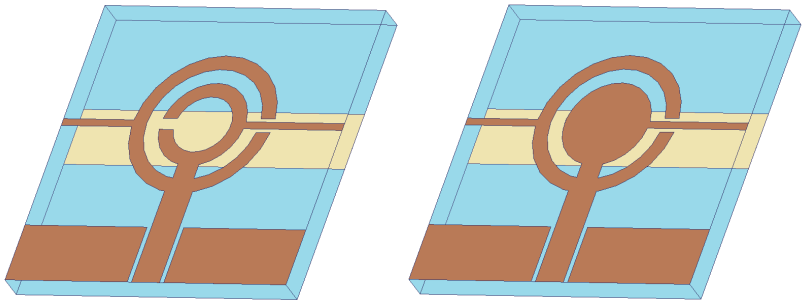

Figure 2.23: *The three-dimensional layout of Prototype 1 (left) and 2 (right).*

restricted into particular range of interest and fundamentally satisfy the feasibility of fabrication.

Numerical results

Table 2.4: *Comparison of optimal parameters between the two proposed antennas*

Proposed Antenna	W	L	R_1	R_2	L_2	g_1	L_1
Prototype 1	21.32	20.76	5.1	1.26	3.89	0.58	2.55
Prototype 2	19.67	16.94	4.92	0.81	6.58	0.22	2.09

Regarding optimization parameters, the initial population consists in 9 particles for each one of 10 swarms, in total 90 particles. After 10 iterations of Meta-PSO evaluation, the best results ever achieved are reported in Table 1. With

the aim of enlarging the bandwidth over the requirement, the extended bandwidth (BW) is related to cost value according to the formulation:

$$\text{Cost Value} = 100 + BW/2 \tag{2.22}$$

The maximum and mean value of cost function ever attained by Meta-PSO after each iteration are denoted in Figure 3.10. Considering two antenna configurations, the electrical length of substrate patch for Protype 2 is smaller than that of Prototype 1; 19.67mm x 16.94mm in comparison with 21.32mm x 20.76mm. The bandwidth comparison is depicted in Figure 2.24, showing good resonant behavior of two proposed antennas over the three requested bands.

Moreover, the gain and radiation pattern of two antennas are also observed in Figure 2.25, Figure 2.26, Figure 2.28 at 3 center frequencies of 2.4 GHz, 3.5 GHz and 5.4 GHz. Two antennas are both placed in x-y plane and the radiation characteristics are investigated in two main cuts y-z (E plane) and x-z (H-plane). As can be seen from the graph, the two antennas have dipole-like radiation pattern, showing good omni-directional behavior. Gain increases in higher frequency band, maximum value recorded is -0.3 dB. To sum up, the two proposed via-less antennas are built up on simple planar structure, showing huge prospect in modern wireless applications.

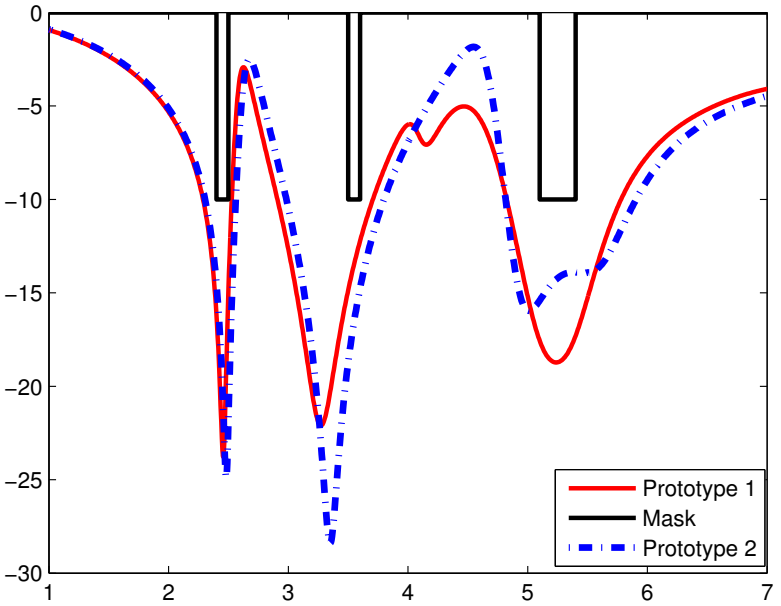

Figure 2.24: *The bandwidth comparison of two proposed antennas*

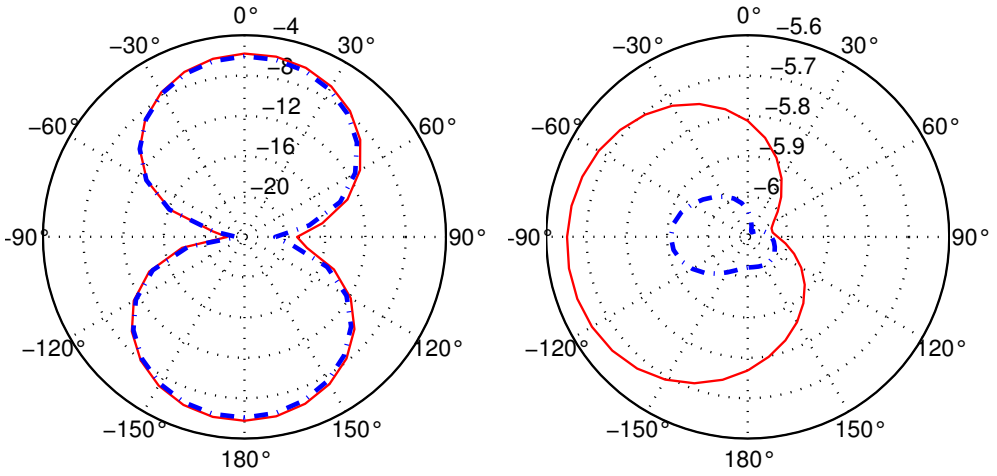

(a) E-plane (b) H-plane

Figure 2.25: *Radiation pattern of two proposed antennas at $f = 2.4$ GHz*

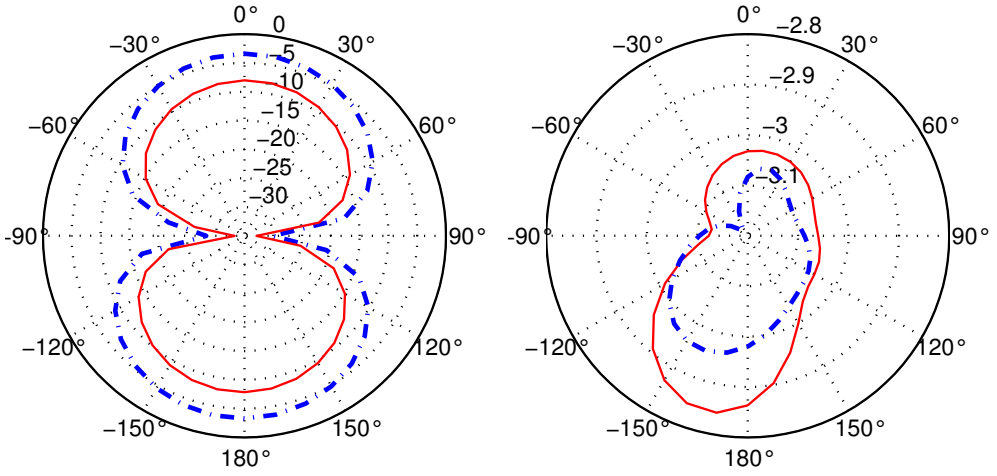

(a) E-plane (b) H-plane

Figure 2.26: *Radiation pattern of two proposed antenna at $f = 3.5$ GHz*

Conclusion

Two Meta-Material inspired antennas have been first constructed by the combination of many structures and then they have been optimized successfully by the use of a global optimizer. Altogether, two critical aspects of modern antenna design have been considered, namely antenna miniaturization and radiation pattern.

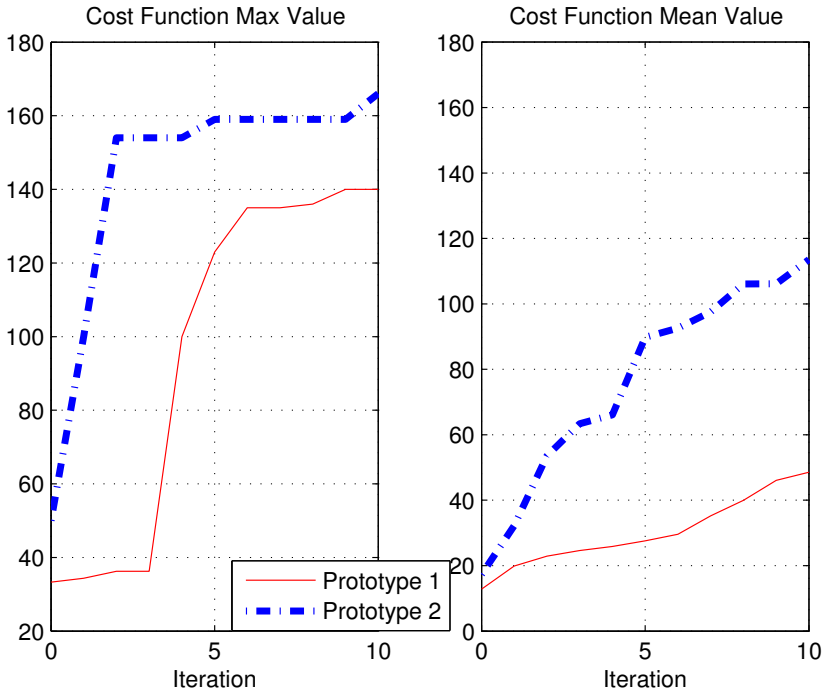

Figure 2.27: *The cost function Max value and Mean value through 10 iterations*

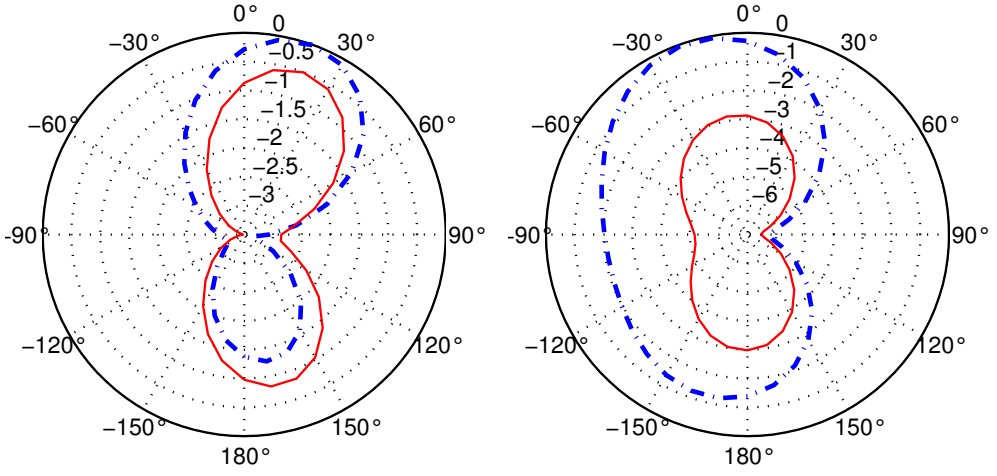

(a) E-plane (b) H-plane

Figure 2.28: *Radiation pattern of two proposed antennas at f = 5.4 GHz*

CHAPTER 3

Surrogate-driven optimization

The starting point of design procedure is the optimization of the antenna bandwidth by adopting a full wave FEM approach and the heuristic technique in Chapter 2. According to the scheme depicted in Figure 2.1, return loss is retrieved as a function of geometrical parameters, whereas the evaluation is based on the interaction between optimizer and EM modeling. However, this approach is computationally expensive since it requires a full wave analysis for each time of assessment. In addition, the storage of data produced by these simulations need a large amount of dynamic memory. With the aim of reducing these computational efforts and memory consumption, it is relevant to introduce a simplified equivalent model of the antenna, in order to be directly managed by the optimization tool.

One way of reducing the computation burden is to construct a surrogate model that can mimic the EM simulator as closely as possible. This approximation model is built up by a data-driven approach, where the inner mechanism of simulation code is not assumed to be known, which the input-output relationship is important. A model of this type is created from the "prior knowledge" from simulator to a limited number of chosen data points. This method is also known as behavioral modeling or black-box modeling, though the terminology is not always consistent. Thanks to the advantage of saving computational effort, the surrogate model can be used in many areas of science, where there are expensive

experiments or evaluations to be performed. The scientific challenge of surrogate modeling is the generation of a surrogate that is as accurate as possible, using as few simulation evaluations as possible. The process comprises three major steps which may be interleaved iteratively:

1. **Sample selection**: It is how we choose to extract "prior knowledge" from full-wave analysis. This is also the main topic of this chapter.

2. Construction of the surrogate model and optimizing the model parameters (Learning algorithms are mentioned in Chapter 1)

3. Appraisal of the accuracy of the surrogate. In this chapter, the validation of *Regular training* and *Irregular training* with full-wave model will be discussed.

The aim of *surrogate-driven optimization* is to develop a new class of optimization techniques where time consumption is reduced significantly. In this section, the configuration of dual rectangular ring proximity coupled feed antenna is used as a test object in order to compare efficiency with conventional scheme in Figure 2.1. Afterwards, in the second part of this chapter, a complete hybridization technique, **Irregular training**, is implemented to optimize a new antenna, dual annular ring proximity coupled feed.

3.1 Regular training

3.1.1 Interpretation of Methodology

Regarding the antenna configuration in Figure 2.4, the relation between inputs and output could be properly modeled by the Artificial Neural Network interpolator. Once being sufficiently trained, the ANN can be considered as a black box where the desired output can be forecasted for any arbitrary set of input data. In order to make ANN model work, suppose a training set (x, y), where x is an input vector and y is the desired output for x and d is the output of ANN for x. Both EBP and LM update the weights between layers based on the gradient of the error function:

$$E = \frac{1}{2}\|d(w, x) - y\|^2 \tag{3.1}$$

where $d(w, x)$ is the output for an input vector.

As shown in Figure 3.1 in order to derive the optimal antenna configuration, ANN is used as an effective interface between antenna designer and global optimization. Initially the full-wave simulator creates the validation data just for the training phase. The full procedure is guided by a global optimizer, by which the

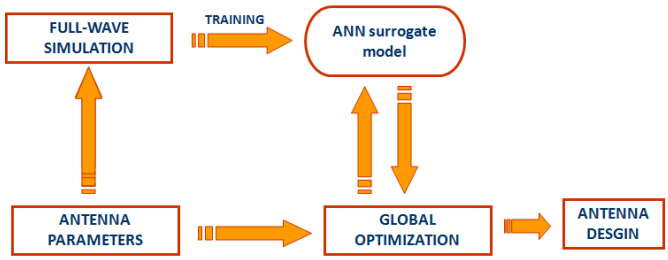

Figure 3.1: *The block diagram of the new approach with ANN surrogate model.*

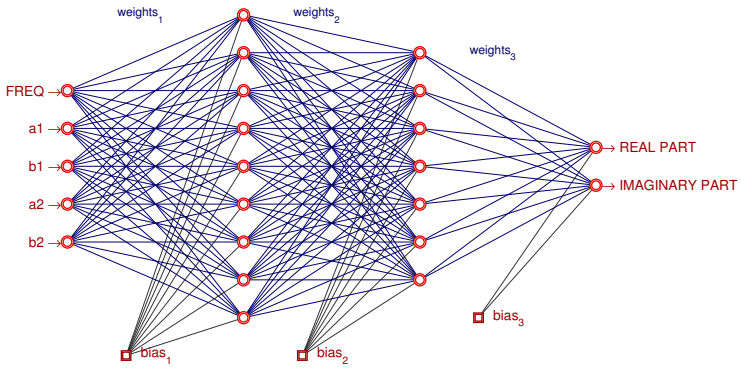

Figure 3.2: *The considered multilayered perceptron structure, with 5 inputs and 2 outputs together with 2 hidden layers of 9 and 7 neurons, respectively.*

inputs are tuned before entering the ANN which is able to produce a corresponding reflection coefficient with the full-wave simulator. Sampling target data and using neural networks are two discrete steps. Regarding this "Regular Sampling Method," the desired outputs are obtained by full-wave analysis from formally chosen geometrical inputs in the region of interest. Each parameter is selected by 5 values, and more variables to be optimized also means the needed training set grows exponentially, as denoted in Table 3.1

Knowledge extracted from the physical model is used as target data for training Artificial Neural Network. After being trained successfully, the satisfied ANN will be employed as an equivalent model to full-wave analysis. Since the ANN architecture only deals with binary and simple activation function, this surrogate model saves a critical amount of execution time. The best results ever found by ANN will be validated by full-wave analysis in order to check the accuracy of the simplified model. The proposed adaptive system consists of two hidden layers

Table 3.1: *Computational cost for different problems*

Assessments	3 inputs	4 inputs	5 inputs
Number of samples	25	125	625
Time consumption	40 mins	3.5 hour	18 hours

with 9 neurons in the first layer and 7 neurons in the second one. Bias is added to the input and hidden layer; a sigmoid function is deployed as an activation function, as sketched in Figure 3.2. For what concern the ANN architecture, the input consists of 5 patterns of which the first is the frequency band of interest, ranging from 1.5 GHz to 3.5 GHz. The remaining four inputs are the length and the width of two rectangular rings, where the reason for these selections is their obvious influence on the radiating behaviors of the top patch. The outputs are the real and imaginary parts of the reflection coefficient. It is also worth noting that antenna radiation is a lossy process and return loss is always a complex number. It is separated into two part: real and imaginary before being recombined to produce amplitude which is the main interest in terms of bandwidth optimization problem. Each different set of input geometrical parameters generates a diverse antenna configuration; all of them will be evaluated by ANN when it experience an adequate training. The capability of knowledge-based ANN in predicting the reflection coefficient is presented in the following section.

3.1.2 Numerical results

For each of four geometrical parameters, we take 5 samples; in total, we have 625 independent cases of reflection coefficient to form the training set data. In relation to the ANN model's numerical efficiency, we take into account the degree of complexity with respect to each different set of inputs. Firstly, we have to rebuild the reflection by full-wave analysis approach; then we make the comparisons with ANN surrogate model. After obtaining the two outputs, real and imaginary parts as the return loss, they are recombined to form the absolute value (Amplitude). All the figures show the behaviors of amplitude according to the change of different geometrical parameters and frequency. Regarding the three-dimensional plot, the axis of frequency remains unchanged since we need to investigate the structure in fixed frequency range from 1.5 GHz to 3.5 GHz with a resolution of 400 steps. The other interval is one of the geometrical parameters that has been discretized with 17 samples each. What results from the full-wave approach is considered as target value for the training of Neural Network. The color bar of top figures stands for the change of the amplitude from 0 to 1 while that of the bottom figures ranging from 0 to 0.2, indicates the error introduced by ANN ap-

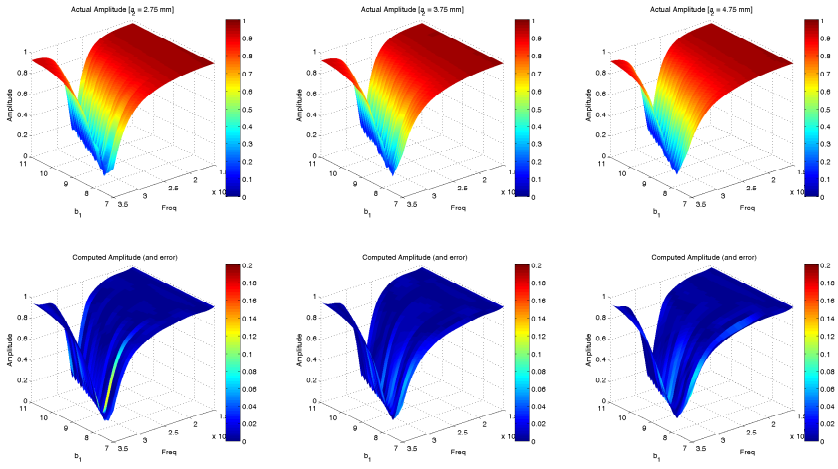

Figure 3.3: *Reflection coefficient amplitude versus b_1 of the proposed antenna configuration, computed with the full wave (top) and reconstructed with the ANN (bottom) in the certain frequency range.*

proximation. As can be seen in the plots of Figure 3.3, in certain cases, the largest error introduced by ANN model is approximately 0.1; this difference can be neglected since we exploit ANN as an effective tool to minimize the computation effort. At the end of the optimization process, the best configuration interpreted by ANN model will be validated again by full-wave approach. According to the reported analyses, the following considerations can be drawn up:

1. The behavior of the proposed antenna changes remarkably by the perturbation of dimensions of external radiators a_1, b_1. On the contrary, this value appears not to be influenced substantially by variables a_2 and b_2, the electrical length of internal ring radiators.

2. The errors gained from ANN surrogate model are relatively trivial. The difference between ANN simulation and physical assessment by full-wave approach can be neglected. Hence, the ANN approximation of reflection coefficient can be entrusted and qualified enough to be integrated into the global optimizer.

Figures 3.4, 3.5, 3.3, 3.6 illustrate the dependence of $|S_{11}|$ on geometrical parameters a_1, b_1, a_2 and b_2 respectively. As can be seen from the graphs, the perturbations of a_1 and b_1 have bigger influence on the structure than a_2 and b_2. In figure 3.6, by changing b_1 from 7 to 9mm in steps of 1 mm, the resonant frequencies shift significantly.

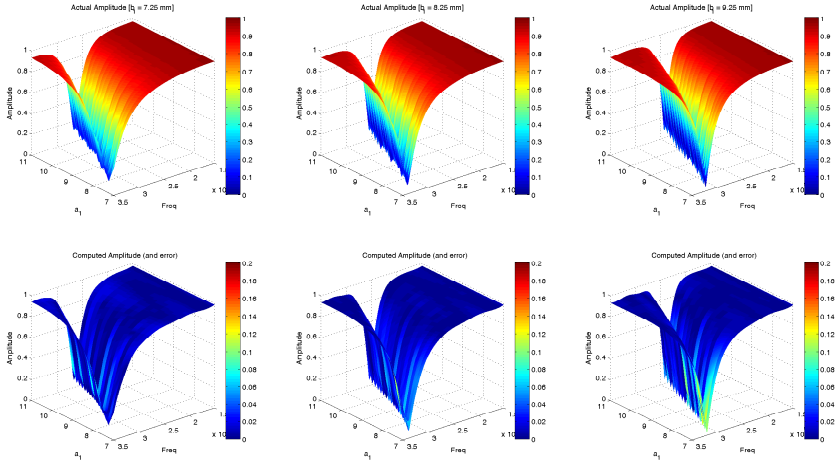

Figure 3.4: *Reflection coefficient amplitude versus a_1 of the proposed antenna configuration, computed with the full wave (top) and reconstructed with the ANN (bottom) in the certain frequency range.*

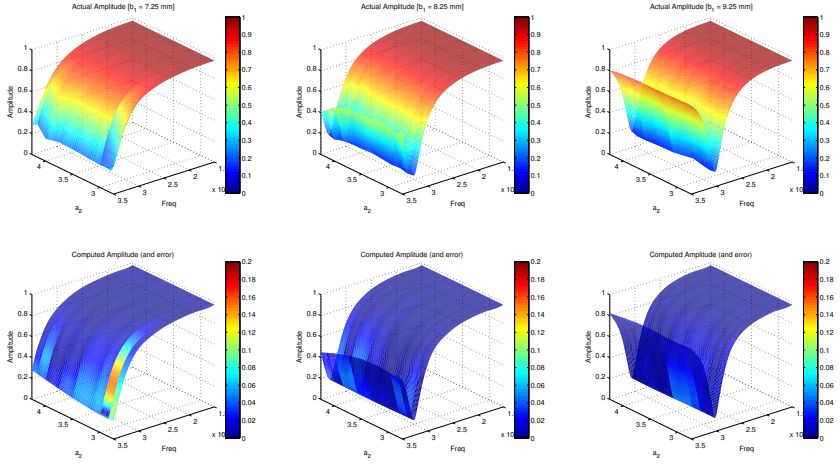

Figure 3.5: *Reflection coefficient amplitude versus a_2 of the proposed antenna configuration, computed with the full wave (top) and reconstructed with the ANN (bottom) in the certain frequency range.*

Instead, in Figure 3.3, while varying a_2 from 2.75mm to 4.75mm with the same step size of 1 mm, the center frequency remain almost the same. All the top plots of each figure represent target data for testing and training the ANN

model. All the comparisons are reported in the bottom parts showing a great accordance between the reconstructed data by ANN estimation and target by full-wave approach. Since training is the most crucial and expensive phase in the use of ANN, computational effort ought to be taken into account. Regarding the network size, the more complex the problem, the bigger the designed network may be required. Figure 3.7 shows the radiation pattern of the optimized antenna

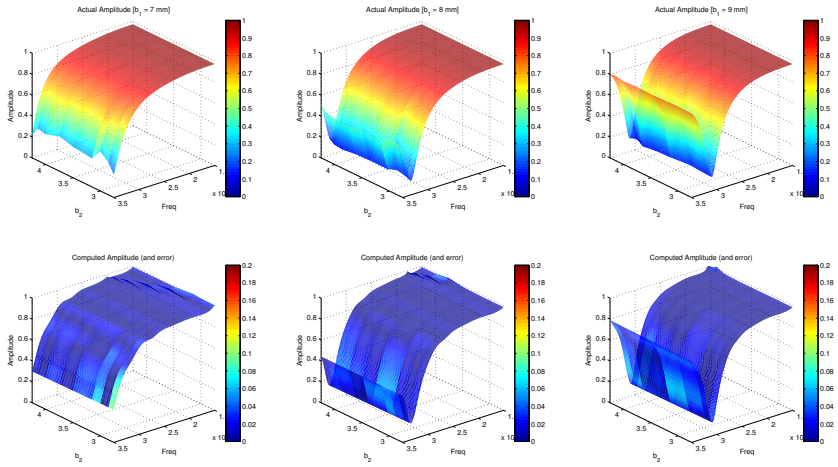

Figure 3.6: *Reflection coefficient amplitude versus b_2 of the proposed antenna configuration, computed with the full wave (top) and reconstructed with the ANN (bottom) in the certain frequency range.*

at the center resonant frequency band, 2.45 GHz. The maximum value of gain recorded is 4 dB, satisfying the constraint for indoor electrical appliances. It is worth noticing that the behaviors of ANN models are close to full-wave analysis, and it again confirms that the differences between the approximation and physical characterization are negligible. Figure 3.8 indicates the gain of the proposed antenna with respect to the change of frequency. As can be observed, radiation pattern peaks in the operating frequency range from 2.4 to 2.5 GHz. All the simulations were done by the use commercial full-wave analysis, on an Intel(R) Core I-7 2600 CPU, 3.4 GHz, 8 GB RAM system. The best configuration of proposed antenna: a = 40mm; b = 40mm; a1 = 19.76; b1 = 21; a2 = 13.14; b2 = 5.5; h = 4.8mm. Regarding the network size, the more complex the problem, the bigger the designed network may be required. In this context, a “split“ NN architecture is proposed to prevent the NN from under-training risk. The original NN is divided into two equal parts, each one is responsible for one output. The dimension of NN structure is also reduced by half, leading to the decrease in time

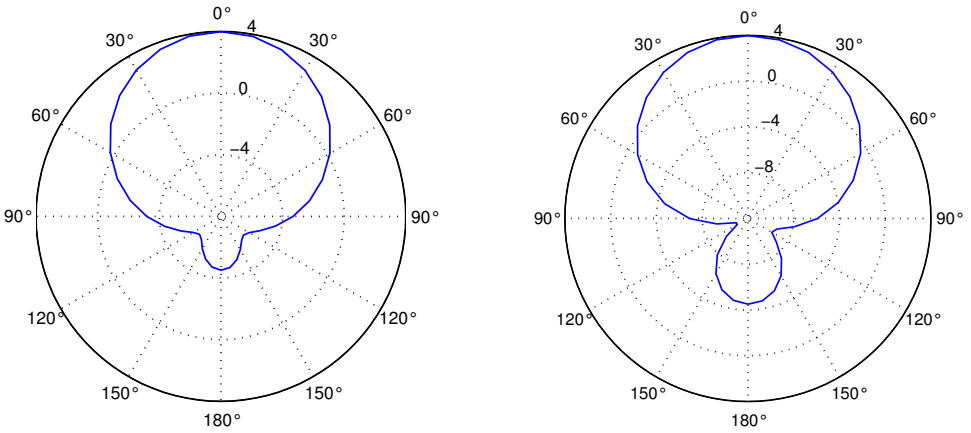

(a) xOz (b) yOz

Figure 3.7: *Radiation Pattern of the antenna when it is placed in xOy plane*

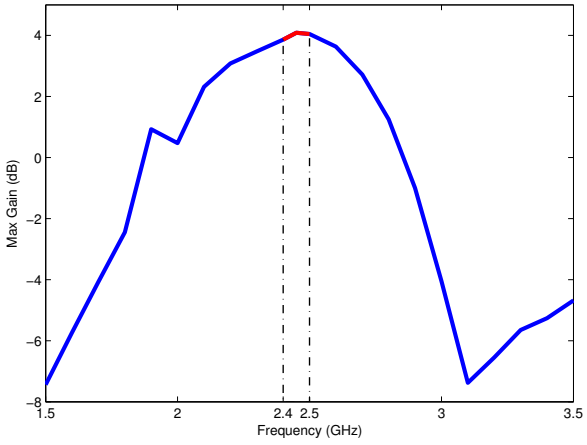

Figure 3.8: *Maximum total gain as a function of frequency in the region of interest*

convergence.

3.1.3 Multi ANN approach

However, when dealing with large-scale problem with huge amount of datasets, Error Backward Propagation (EBP) algorithm is not adequate to handle that kind of sophisticated problem. In order to tackle this issue, a second-order algorithm namely Levenberg-Marquandt (LM) is adopted. The optimal solution would be

using LM training for two separated Neural Networks and then unifying those two distinguished outputs to reform the amplitude of reflection coefficient. Table 3.2 reports the details of computational time for each kind of network. As can observed from Table 3.1 and Table 3.2, the total optimization time is reduced radically by the use of ANN. The driving reason is quite apparent: ANN only consists of simple processing units and it treats mainly binary objects. On the other hand, full-wave characterization always has to deal with a huge number of integral equations. Figure 3.9 illustrates the robustness of the proposed method: LM

Table 3.2: *Comparisons of computational time and numerical efficiency between the training algorithms.*

Assessment Categories	EBP full	EBP seperrated	LM full	LM separated
Training Time	20 hours	10 hours	1 hour	30 min
Error Committed	0.01	0.001	0.0005	0.0004
Optimization Time (when being integrated)	7 mins	5 mins	5 mins	4 mins

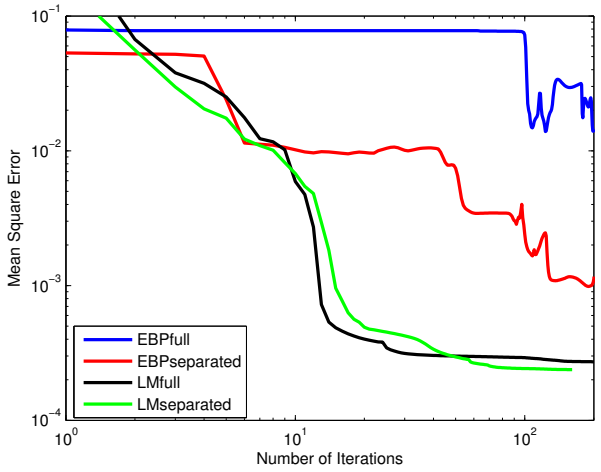

Figure 3.9: *Training error level as a function of number of iterations versus proposed methods.*

training for two separated networks. As regards the EBP algorithm, the division of original Neural Network into two separated ones declines significantly mean the square error to the minimum value of below 0.001. However, as reported in Figure 3.9, LM is proved to be more effective in minimizing the error grade. Both full network approach and separated one demonstrate the great improvement in solution accuracy. The best result is achieved by implementing LM-2 outputs. After the optimization run, the resulting geometrical configurations

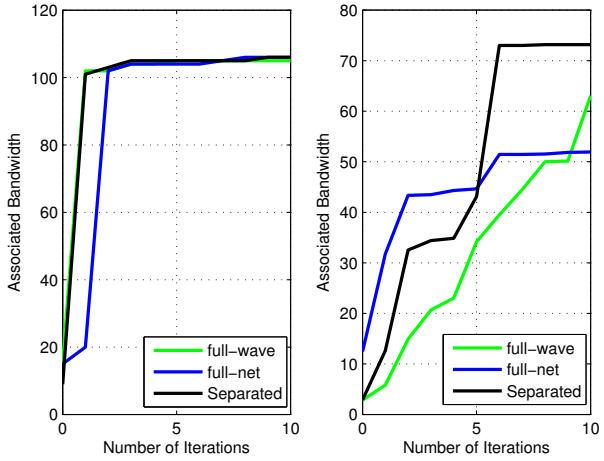

Figure 3.10: *Comparison of ANN model with full-wave analysis model when being integrated with global optimization tool.*

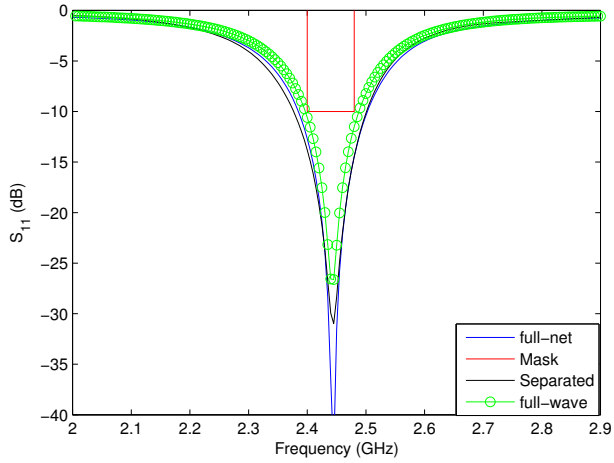

Figure 3.11: *ANN optimization and full-wave analysis validation.*

have been validated by full-wave analysis. Figure 3.11 shows the comparisons between the different uses of ANN (by LM training). It demonstrates that all proposed methods have a good match with target data. However, the two-output approach exhibits a better performance since the output data is closer to the validation by full wave analysis. The absolute difference between the target data and ANN outcome is just 0.0005. All the convergence curves of different approaches with Different Meta PSO optimization scheme are presented in Figure 3.10. For

the reported simulations, 8 swarms of 10 agents have been considered. In total, the whole population of 80 particles are tested for 10 iterations. With the aim of enlarging the bandwidth over the requirement, the extended bandwidth (BW) is related to cost value according to the formulation:

$$\text{Cost Value} = 100 + BW/2 \tag{3.2}$$

where BW is the measure of -10 dB bandwidth obtained from $|S_{11}|$ in Figure 3.11.

The presented results show the ability of Artificial Neural Network as an important vehicle in frequency EM-modeling. The achieved efficiency demonstrates the robustness of the surrogate model in terms of sensible reduction in computing resource. The accuracy of the solution makes Artificial Neural Network suitable to be implemented as a convenient interface between antenna designers and global optimization tools.

3.2 Irregular training

In the **Regular Training** method, sampling target data and using neural networks are two discrete steps. Regarding this "regular methodology," the desired outputs are obtained by full-wave analysis from formally chosen geometrical inputs in the region of interest. Each parameter is selected by five values, more variables to be optimized also means the needed training set grows exponentially, as denoted in Table 3.1

3.2.1 Interpretation of the method

When linking ANN with a global optimizer, it is obvious that there is information exchange between them. The main idea of this technique is to utilize the data from unsatisfying antenna configurations as prior knowledge for ANN training. ANN is a self-adaptive modeling tool that changes its structure on the basis of external or internal information flowing through the network. Therefore, the more information updated after each loop in Algorithm 3.1, the more accurate outputs ANN surrogate model can provide. The crucial difference between this hybridization technique and a conventional one, as presented above, is the way training set data retrieved.

In a population-based optimizer such as PSO, a particle, representing an antenna configuration, is characterized by a random vector **X** = [x_1,x_2,...,x_6]. Regarding this particular case, where is **X** defined in six-dimensional space, where exist six geometrical parameters to be optimized, with initial population of 50 agents. In order to enter the **While** loop, the primary error has been chosen as 10, larger than 0.3 of the constraint. Firstly, at step (1), all N_p particles are evaluated

Data: Assigned error: a_err
Number of population N_p ;
Prior knowledge: P; G ;
while *ANN model is not robust enough ($err > a_err$)* **do**
    Update the P and G;
    Do optimization by full-wave analysis (1);
    if *global best agent satisfies the bandwidth threshold* **then**
        Finish, Generate the best antenna configuration (2);
    else
        Remember P, G (3);
        Record unsatisfied antenna configurations for training data (4);
        Set up and train ANN model with existed data set (5);
        Check model accuracy by full-wave characterization by X_test (6);
        Update the value of err (7);
        Update the P and G (8);
    end
end
repeat
    Using ANN model to find the best solution X_best (9);
    Validate with full-wave analysis (10)
until *ANN best agent satisfies the bandwidth threshold*;

Algorithm 3.1: Pseudo-code for hybridazation technique

by PSO optimizer for one iteration. If the global-best satisfies has the bandwidth lager than WIFI band, then the loop is finished. Otherwise, all N_p unsatisfying configurations both inputs **X** and outputs to form training data for ANN, in steps (4) and (5). The positions of P and G are recorded at iteration (k) of the loop and they are updated at the iteration $(k+1)$ so that the computational effort is not lost. At the end of the **While** loop, surrogate model accuracy is validated with physical model by particle X_{test}. The representative parameter err is defined by the absolute difference between the Amplitude of Return Loss of two models. If ANN equivalent model can overcome this condition, it will be used to replace full-wave analysis. If not the **While** loop continues to gain more knowledge for machine learning ANN. After each time the loop cannot find proper ANN model, N_p antenna configurations are added into training data. It is also worth noting that ANN is a fault-tolerance model, thus it satisfies the case of X_test but for X_best the best antenna configuration ever found by ANN might have bandwidth condition mismatch when being checked with full-wave analysis. In order to tackle this issue, a **Repeat** loop is created. This loop ends when best particle by ANN satisfies both constraints of bandwidth and accuracy. The details of the proposed method is clearly explained in Diagram 3.12

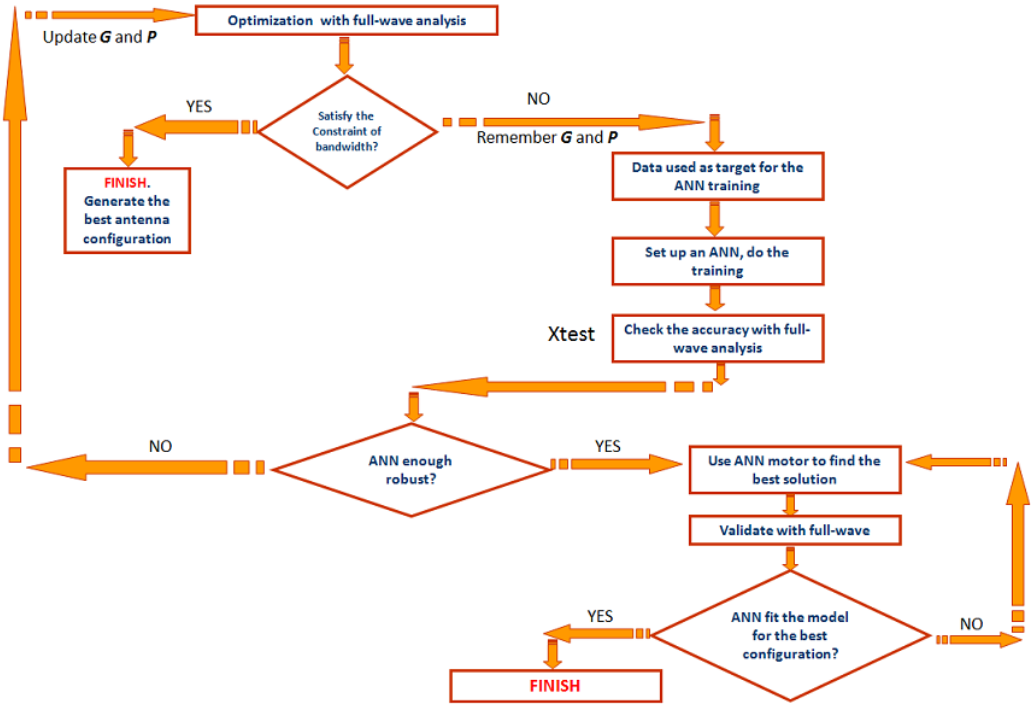

Figure 3.12: *Irregular Training in details*

3.2.2 Applying to the case of Dual Rectangular Ring Antennas

The bandwidth optimization for this antenna was first done in chapter 2, and by **Regular Training**. In this case, it is reused as a test object for **Irregular Training** scheme. The geometrical parameters are arbitrarily selected by optimizer to generate different antenna configurations. The creation of new particles must obey the feasibility of antenna fabrication such that the rings cannot overlap each other or exceed the substrate. The data from unsatisfied antenna structures will be used as the training set for surrogate model.

By applying the new scheme, after 90 times of sampling from random set of inputs, the ANN is robust enough to replace full-wave analysis. Considering the four-variable problem in this article, the new approach save more than 25 per cent of computational effort. Regarding the 3D plot in Figure 3.13, it denotes the change of the antenna return loss and the faults committed by each model. The axis of frequency remains unchanged since we need to investigate the structure in fixed frequency range from 1.5 GHz to 3.5 GHz with a resolution of 400 steps. The other interval is b_1 that has been discretized with 9 samples each. Therefore, amplitude of return loss is recognized as the function of b_1 and frequency, while a_2 and a_1 are fixed at the values of 2.5 mm and 7 mm respectively. The color bar

Table 3.3: *Computational cost for different approaches*

Methods	Conventional	Regular sampling	Irregular sampling
Number of assessments	300	125	90
Time consumption	10 hours	4.7 hours	3 hours

ranging from 0 to 0.2 represents the error introduced by two ANN approximations.

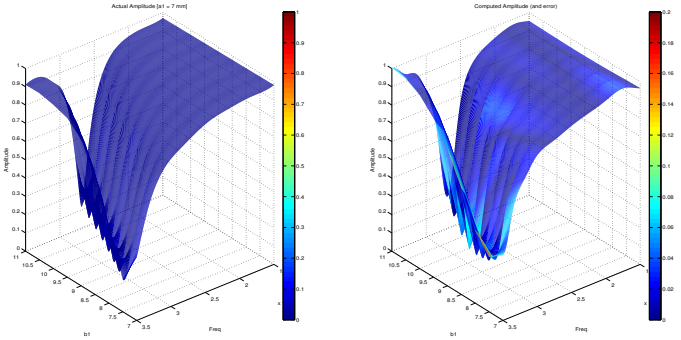

Figure 3.13: *Numerical comparison between the two optimization schemes*

As can be seen from the graph, a maximum value of error at some certain values of the interval is recorded at less than 0.08 in the interval of [0,1]. This fact again confirms that the differences between ANN approximations and physical characterization are negligible . Although the error is slightly higher in this new scheme with respect to the regular one, when data are processed by the optimizer it still can find the antenna configurations satisfying the design constraints. The best results ever found by ANN model again have been validated by full-wave analysis. It also worth noting in Table 3.3 that new scheme saves a large amount of computational time and, more importantly, ANN surrogate model and PSO combines smoothly to form a new and hybrid class of optimization.

3.2.3 Optimization of Dual Annular Ring Antenna by New Scheme

In this research, in order to examine the robustness of hybridization technique, a new proximity coupled feed type antenna has been chosen as a test object. From the viewpoint of complexity, dual annular ring antenna configuration is as sophisticated as a dual rectangular ring. These two antennas have the same type of feeding line but they have different degrees of freedom when being optimized. This multi-layer structure has two concentric annular rings situated on top plane,

feeding microstrip line in the middle layer and ground plane on the bottom layer. All these structures are printed on FR4 substrate with dielectric constant ε_r =

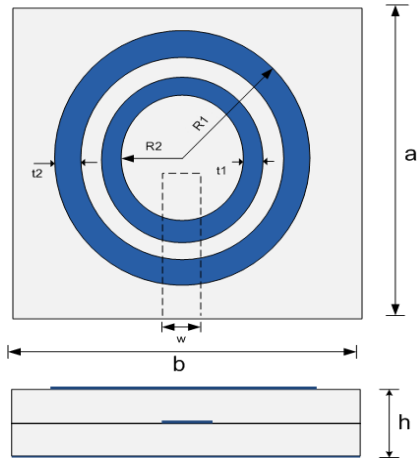

Figure 3.14: *Top view and side view of the test object antenna*

4.4 and 2.4 mm substrate height for each layer. The main object of optimization scheme is to enlarge as much as possible the bandwidth over requested WIFI band (2.4 GHz to 2.5 GHz). As illustrated in Figure 3.14, six geometrical parameters namely a, b, R_1, R_2, t_1, t_2 are properly modeled in a specific range of interest. Fabrication constraint and feasibility of this structure are satisfied, for example: two concentric rings cannot overlap each other, the outer ring cannot exceed the region of the patch. From the perspective of optimization, the complexity of Dual

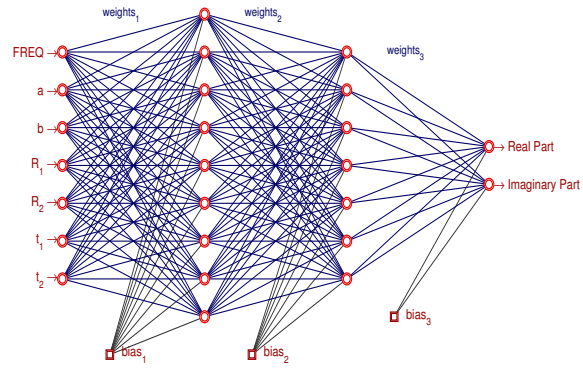

Figure 3.15: *Artificial Neural Network Architecture*

Annular Ring problem is similar to that of Dual Rectangular Ring. Therefore,

the proposed ANN structure comprises frequency, together with six geometrical parameters a, b, R_1, R_2, t_1, t_2 as inputs and two hidden layers of 9 neurons and 7 neurons respectively. This architecture ends up with two outputs: real part and imaginary part of return loss, as illustrated in Figure 3.15. At the end, the two outputs are recombined to form the amplitude of the return loss, which is the main concern of the global optimizer.

Numerical results

Comparisons of numerical efficiency are illustrated by a 3D plot in Figure 3.16. One axis is $Frequency$ since antenna structures are investigated in the band of interest (from 1.5 GHz to 3.5 GHz) with the resolution of 400 steps. Another interval is the geometrical parameter b that has been discretized by 7 samples. The rest of antenna parameters are fixed as: a = 30 mm; $R1$ = 12 mm; $R2$ = 5 mm; $t1$ = 1.5 mm; $t2$ = 1.5 mm. The color bar, ranging from 0 to 0.2, indicates the error introduced by ANN approximations in conventional scheme [73] and proposed hybrid method. As can be seen from the graph, the error committed by Irregular sampling method is slightly higher than Regular one. The maximum error value recorded is 0.1 and this difference can be neglected. The primary purpose is a better control by obtaining training data from arbitrary sets of inputs rather than formally chosen space so that the total time consumption is saved radically.

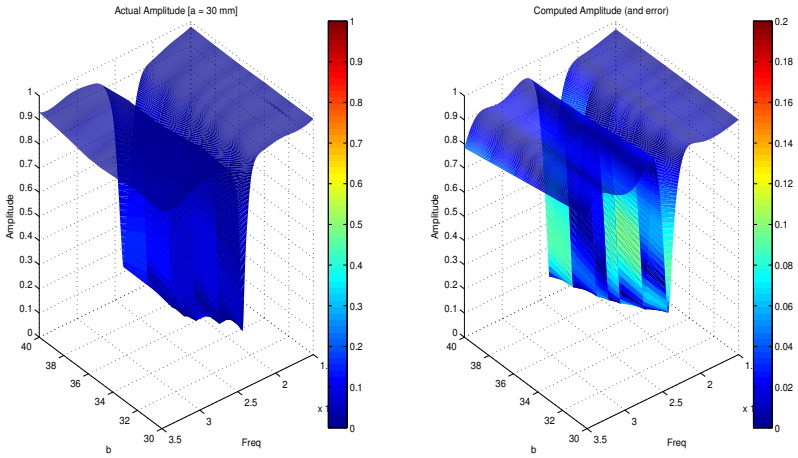

Figure 3.16: *Numerical efficiency comparison between conventional and hybridization technique according to the change of $frequency$ and b*

As shown in Table 3.4, according to **Regular scheme**, in order to create training set data, 15625 samples are needed. As a result, the proper ANN architecture

for this huge datasets might not be found. Provided that it exists, the amount of time for training is tremendous and it would lead the surrogate-based optimization by ANN to be impractical. By employing this hybridization technique, the case of over-training data is eliminated by a set of constraints and loops. Regarding this particular case, the total amount of time spent is 17 hours, much less than estimated 25 days in the conventional scheme.

Table 3.4: *Comparison of computational effort between conventional and hybridization technique*

Assessments	Regular sampling	Irregular sampling
Number of samples	$5^6 = 15625$	450
Estimated time consumption	25 days	17 hours.

Table 3.5: *Optmizied geometrical parameters by ANN model when being integrated with PSO optimizer*

Parameter	a	b	R1	R2	t1	t2
Values	40.13	39.92	12.7525	6.6776	3.9319	3.7056

The best particle **X** found by ANN model is validated by full-wave approach by **Repeat** loop in Algorithm 3.1. The details of final best antenna configuration are presented in Table 3.5. Figure 3.17 shows the good accordance between the outcomes of ANN model with full-wave model.

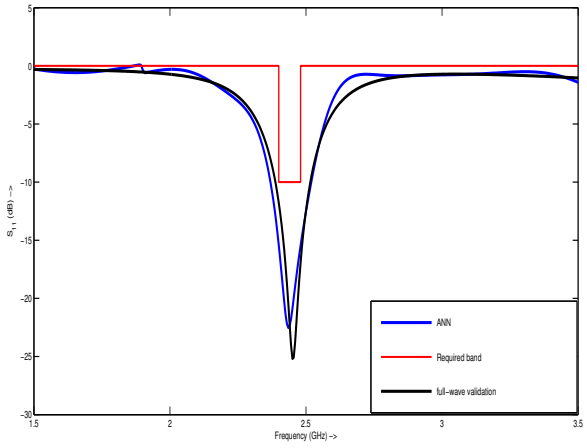

Figure 3.17: *The best configuration found by ANN model and validated by full-wave analysis*

At the end of the **While** loop, after being checked as a robust model, cost func-

tion **F** is now defined by ANN model. The convergence when integrating ANN with PSO optimizer is demonstrated in Figure 3.18. 500 particles are considered in 10 iterations. With the aim of enlarging the bandwidth over requested Wifi band, extended bandwidth is related to cost value by the formulation:

$$\text{Cost Value} = 100 + BW/2 \tag{3.3}$$

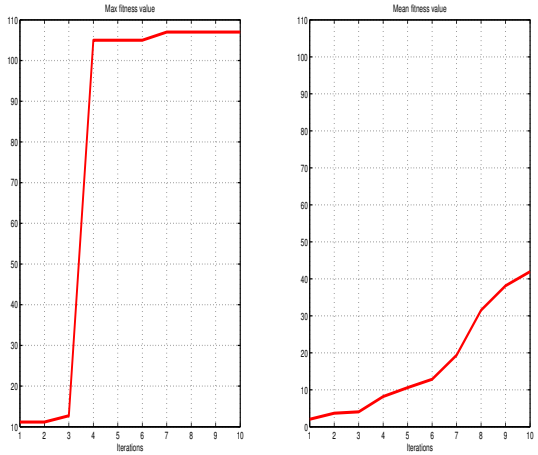

Figure 3.18: *The change of cost value throughtout 10 iterations with population of 500 particles*

CHAPTER 4

Electromagnetic Modeling by the use of Special Functions

4.1 Introduction

In previous chapters, computational intelligence from optimization algorithms to Artificial Neural Network (ANN) were discussed. From the viewpoint of computer engineering, once an arbitrary Electromagnetic (EM) problem is properly projected, the best solution corresponding to a specific objective function can be retrieved. Throughout chapter 1 and chapter 3, commercial full-wave analysis has been used as a convenient interface between designer and global optimizer, which is known as the tool to extract prior knowledge for ANN. However, when dealing with electromagnetic problem, a vast and sophisticated branch of physics, a simulator cannot appropriately model geometrical and electrical characteristics of the environment under investigation. In order to tackle this issue and take a deeper look into electromagnetic theory, some particular phenomenon should be manually defined by the use of mathematical formulas. In the scope of this thesis, a specific case of electromagnetic scattering is going to be considered.

The geometry of the problem can be described as a metallic prolate spheroid that is coated with confocal layers of penetrable material that is either isorefrac-

tive or anti-isorefractive to the surrounding space. There is a primary source which is an electric or magnetic dipole located outside the coating layer on the axis of symmetry of the structure and axially oriented. Such configuration is amenable to an exact solution by separation of variables, wherby the field components are expressed as infinite series of products of spheroidal special functions. In this particular coordinate, there are no restrictions on material properties or source types because the eigenfunctions must assume the same value on either side of the interface and do not depend on the propagation constants of the two media in contact. In this specific case, special wave functions, radial and angular spheroidal functions are used to characterize the fields of the coating layer, either Double PosSitive (DPS) or Double NeGative (DNG).

The development of novel electronic materials such as DNG metamaterial is still in its infancy, insofar as bandwidth and low losses are considered, but is proceeding rapidly, especially at optical and near-optical frequencies. The recent introduction of non-Foster active elements holds promise for future microwave applications, and especially for structures incorporating anti-isorefractive materials. In the literature, structures involving DNG materials with planar interfaces have been studied by Velasgo [74], Shelby et al. [75] and Engheta [76] among others, with circular cylindrical interfaces excited by a line source by Arslanagic et al. [77], and with spherical interfaces excited by an electric Hertzian dipole by Arslanagic et al. [78]

The model expansion coefficients in the infinite series can be determined analytically by imposing boundary conditions in spheroidal coordinates. This research on the boundary-value problem is conducted in the phasor domain with the time-dependence factor $exp(-i\omega t)$ ommitted throughout. Although prolate and oblate structures as penetrable materials of acoustic waves have been studied for many years, none of analytical results shown in this research is known beforehand. The details of numerical analysis will be discussed rigorously in the next sections.

4.1.1 Introduction to Prolate and Oblate coordinates

It has been said in the introduction that electromagnetic problems are often solved by applying boundary conditions. Such conditions are clearly strictly dependent on the geometry of the object itself and this is the reason why it can be often useful to adopt a special coordinate system describing the shape of the object in a simple way and allowing for a convenient mathematical representation of the constraints on the field. Theoretically, we could define an infinite number of *general or curvilinear coordinates systems* and use the more suitable ones for our case. An explanation about how to create a coordinate system can be found in Stratton [81]. In the case under consideration it is immediate to recur to the *spheroidal coordinate system*, which allows for the representation of the surface of the cavity by simply fixing the value of one coordinate (ξ). In fact, in such a system every point of the space is uniquely identified by the intersection of three orthogonal surfaces that are an ellipsoid, a hyperboloid and a half-plane. Thus, keeping constant the coordinate identifying the ellipsoid and letting vary the other two, we get exactly a spheroidal surface. The ellipsoids and hyperboloids defining the coordinates are generated by rotation of confocal ellipses and hyperbolas about the major or minor axis. In the first case the coordinate system is said to be *prolate*, while in the second one *oblate*. Typically, the z-axis is chosen to be the axis of revolution and we indicate the interfocal distance with the letter d.

Prolate system

As it can be found in Flammer [79], the prolate spheroidal coordinates are related to the rectangular coordinates by the transformation

$$
\begin{aligned}
x &= \frac{d}{2}\sqrt{(\xi^2-1)\,(1-\eta^2)}\cos\phi \\
y &= \frac{d}{2}\sqrt{(\xi^2-1)\,(1-\eta^2)}\sin\phi \\
z &= \frac{d}{2}\xi\eta
\end{aligned}
$$

with $-1 \leq \eta \leq 1,\ 1 \leq \xi < \infty,\ 0 \leq \varphi \leq 2\pi.$

For this case it is found that the length of the major axis of the prolate ellipsoid is related to ξ by the product $d\xi$ and the minor axis is given by $d\sqrt{\xi^2-1}$. The minimum value allowed for ξ is 1 and it corresponds to an an ellipsoid degenerated in a straight line between the two foci along the z-axis. The surface corresponding to $|\eta| = constant$ is a two-sheet hyperboloid of revolution for

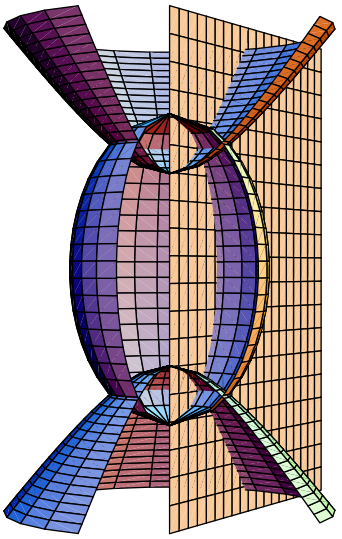

Figure 4.1: *Prolate spheroidal coordinate system section view.*

which the generating line of the asymptotic cone passes through the origin with inclination $\theta = \arccos\eta$. The degenerate surface obtained for $|\eta| = 1$ covers all the z-axis but the segment joining the two foci (the one identified by $\xi = 1$). In particular, the positive part of the z-axis is defined by $\eta = 1$ and the negative part is represented by $\eta = -1$. In this system $\eta = 0$ corresponds to the whole x,y-plane. The coordinate $\varphi = constant$ identifies a half-plane originating from the z-axis and forming the counterclockwise φ angle with the xz-plane.

Oblate system

For the oblate system the transformation to cartesian coordinates is given by

$$\begin{cases} x = \sqrt{\dfrac{d}{2}[(1-\eta^2)(\xi^2+1)]}\cos\varphi, \\ y = \sqrt{\dfrac{d}{2}[(1-\eta^2)(\xi^2+1)]}\sin\varphi, \\ z = \dfrac{d}{2}\eta\xi \end{cases} \tag{4.1}$$

with $-1 \leq \eta \leq 1,\ \ 0 \leq \xi < \infty,\ \ 0 \leq \varphi \leq 2\pi.$

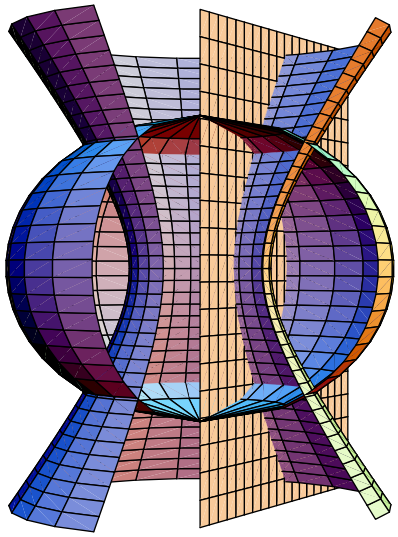

Figure 4.2: *Oblate spheroidal coordinate system section view.*

In the spheroidal coordinate system the minor axis is given by the product of the interfocal distance and the cavity surface coordinate $d\xi$ while the major axis is found to be $d\sqrt{\xi^2+1}$. The minimum value for ξ in this case is 0 and it corresponds to a circular disk of radius $a = d/2$ laying in the xy-plane and centered in the origin. Here $|\eta| = constant$ represents a one-sheet hyperboloid of revolution which asymptotic cone is the same as in the prolate case. For $|\eta| = 1$ we get a degenerate surface corresponding to the entire z-axis. As for the prolate system, the positive and negative part of the axis are identified respectively by $\eta = 1$ and $\eta = -1$. The surface $\eta = 0$ is the xy-plane except the disk $\xi = 0$. The coordinate φ represents also in the oblate system a half-plane forming the angle φ with the xz-plane.

Scalar Wave Equation and Spheroidal Functions

As it has been said in the previous section, the problem we are studying is characterized by an object illuminated by an electromagnetic wave. The use of a special coordinate system is necessary to easily represent mathematically the boundary conditions. It must be said though, that once we identify the more appropriate coordinate system, we have to solve the *wave equation* in the particular system we have defined and this is not always possible. Spheroidal coordinates are among

coordinate systems whereby the solution by using *the separation of variables method* can be applied. The scalar wave equation

$$(\nabla^2 + k^2)\psi = 0. \tag{4.2}$$

has a solution that is composed by three independent functions:
(i) the angular spheroidal function $S_{mn}(c, \eta)$,
(ii) the radial spheroidal function $R_{mn}(c, \xi)$,
(iii) the sine or cosine function, and it is in the form

$$\psi_{mn} = S_{mn}(c, \eta)R_{mn}(c, \xi)^{\cos}_{\sin} m\varphi. \tag{4.3}$$

The aforementioned spheroidal functions are for the prolate coordinate system. For the oblate case it is sufficient to replace c with $-ic$ and ξ with $i\xi$:

- $S_{mn}(-ic, \eta)$,
- $R_{mn}(-ic, i\xi)$,

which gives the solution of the wave equation in the form:

$$\psi_{mn} = S_{mn}(-ic, \eta)R_{mn}(-ic, i\xi)^{\cos}_{\sin} m\varphi.$$

Basically, the angular and radial spheroidal functions are a generalization of Legendre and spherical Bessel functions respectively.

Angular Functions

Writing the scalar wave function

$$(\nabla^2 + k^2)\psi = 0 \tag{4.4}$$

in prolate and oblate spheroidal coordinates

$$\left[\frac{\partial}{\partial\eta}(1-\eta^2)\frac{\partial}{\partial\eta} + \frac{\partial}{\partial\xi}(\xi^2-1)\frac{\partial}{\partial\xi} + \frac{\xi^2-\eta^2}{(\xi^2-1)(1-\eta^2)}\frac{\partial^2}{\partial\varphi^2}\right]\psi + c^2(\xi^2-\eta^2)\phi = 0 \tag{4.5a}$$

$$\left[\frac{\partial}{\partial\eta}(1-\eta^2)\frac{\partial}{\partial\eta} + \frac{\partial}{\partial\xi}(\xi^2+1)\frac{\partial}{\partial\xi} + \frac{\xi^2+\eta^2}{(\xi^2+1)(1-\eta^2)}\frac{\partial^2}{\partial\varphi^2}\right]\psi + c^2(\xi^2+\eta^2)\phi = 0, \tag{4.5b}$$

where

$$c = \frac{1}{2}kd, \tag{4.6}$$

and solving using the procedure of separation of variables, which implies a solution in the form of Lamé products

$$\psi_{mn} = S_{mn}(c,\eta)R_{mn}(c,\xi)^{\cos}_{\sin}\, m\varphi, \tag{4.7a}$$

$$\psi_{mn} = S_{mn}(-ic,\eta)R_{mn}(-ic,i\xi)^{\cos}_{\sin}\, m\varphi, \tag{4.7b}$$

we get that the angular spheroidal functions must satisfy the ordinary differential equations

$$\frac{d}{d\eta}\left[(1-\eta^2)\frac{d}{d\eta}S_{mn}(c,\eta)\right] + \left[\lambda_{mn} - c^2\eta^2 - \frac{m^2}{1-\eta^2}\right] S_{mn}(c,\eta) = 0, \tag{4.8a}$$

$$\frac{d}{d\eta}\left[(1-\eta^2)\frac{d}{d\eta}S_{mn}(-ic,\eta)\right] + \left[\lambda_{mn} - c^2\eta^2 - \frac{m^2}{1-\eta^2}\right] S_{mn}(-ic,\eta) = 0, \tag{4.8b}$$

for the prolate and oblate case respectively. In the above equations λ_{mn} and m are the separation constants. As explained in Flammer [79], we are interested only in those results for which the *wave function* (4.7) is single valued. In order to get physically significant solutions, this requires that m has to be an integer, which can be assumed positive or zero without loss of generality. To get the solution of the differential equation (4.5) it is required to find its eigenvalues and then the associated eigenfunctions $S_{mn}(c,\eta)$ or $S_{mn}(-ic,\eta)$ that are, respectively, the prolate and oblate spheroidal angular functions of the first kind, of order m and degree n, where $n \geq m$. The eigenvalues are found to be those values of $\lambda_{mn}(c)$, or $\lambda_{mn}(-ic)$ in the oblate case, for which the solutions of the wave equation are finite at $\eta = \pm 1$. From now on, only the prolate case is considered not to make the explanation too cumbersome since, as said before, the oblate case is easily obtained from the prolate by simply replacing c with $-ic$ and, in the radial functions, ξ with $i\xi$.

When c approaches zero, the functions satisfying 4.5 become Legendre functions of the first kind (as in the simpler spherical case). Since the spheroid can be seen as a deformed sphere, we can think to decompose the angular spheroidal functions, as the solution for such geometry, in an infinite sum of Legendre functions appropriately weighted, which reduces exactly to a single Legendre function ones we consider the spherical problem that imposes all the weight coefficients but one to zero:

$$S_{mn}(c,\eta) = \sum_{r=0,1}^{\infty\,\prime} d_r^{mn}(c) P_{m+r}^m(\eta) \tag{4.9}$$

The prime over the summation sign is used to indicate that the summation is only over even values of r for $n-m$ even and over odd values of r for $n-m$ odd.

At this point, the following step in determining the angular spheroidal function is to find the coefficients $d_r^{mn}(c)$. The procedure is not reported here but it can be found in Flammer [79]. Particular attention must be paid in the normalization criterion employed. In fact, several different criteria exist and it must be specified the one we use in order not to be mistaken. In this work the coefficients are normalized so that the angle function reduces to the associated Legendre function when c becomes zero. To do this, it may be imposed that the behavior of S_{mn} near a particular value of η approaches that of P_n^m. Following Chu and Stratton [80, 81], as reported on page 21 of Flammer [79], $\eta = 0$ is chosen to be the normalization point. The angular normalization coefficient we get is given by the relationship:

$$N_{mn} = 2 \sum_{r=0,1}^{\infty\prime} \frac{(r+2m)!(d_r^{mn})^2}{(2r+2m+1)r!} \,. \tag{4.10}$$

It should be noted the dependence of the angular function on the parameter c, namely on the wave number k and the interfocal distance d. The dependence on k is clear since the propagation constant contains information about the illuminating wave and the properties of the medium in which the wave is propagating, that are necessary in describing the total field. On the contrary, the dependence on d could be not so immediate to understand. The explanation is found in the fact that the spheroidal coordinate system is not unique. In fact, we can define an infinite number of such systems just choosing a different interfocal distance. So, the dependence on d is needed to take in account for the particular spheroidal coordinate system we are using.

Radial Functions

The radial spheroidal functions, $R_{mn}(c,\xi)$ and $R_{mn}(-ic,i\xi)$, as the angular ones, are obtained by solving the wave equation expressed in spheroidal coordinates. They are the eigenfunctions of the equations

$$\frac{d}{d\xi}\left[(1-\xi^2)\frac{d}{d\xi}R_{mn}(c,\xi)\right] + \left[\lambda_{mn} - c^2\eta^2 - \frac{m^2}{1-\xi^2}\right] R_{mn}(c,\xi) = 0, \tag{4.11a}$$

$$\frac{d}{d\xi}\left[(1-\xi^2)\frac{d}{d\xi}R_{mn}(-ic,\xi)\right] + \left[\lambda_{mn} - c^2\xi^2 - \frac{m^2}{1-\xi^2}\right] R_{mn}(-ic,\xi) = 0, \tag{4.11b}$$

for which the eigenvalues are the same as the ones found in computing the angle functions. We identify four kinds of radial functions. The first and second kinds, $R_{mn}^{(1)}$ and $R_{mn}^{(2)}$, are the basics and the third and forth kinds, $R_{mn}^{(3)}$ and $R_{mn}^{(4)}$, can be

obtained as sum and subtraction of the first two, respectively:

$$R_{mn}^{(3)} = R_{mn}^{(1)} + iR_{mn}^{(2)} \,, \tag{4.12}$$

$$R_{mn}^{(4)} = R_{mn}^{(1)} - iR_{mn}^{(2)} \,. \tag{4.13}$$

As the angular spheroidal functions are defined so that they coincide with the associate Legendre functions for c vanishing, the first, second, third and fourth kinds radial spheroidal functions reduce to the spherical Bessel, Neumann and Hankel functions of the first and second kinds, respectively, as c goes to zero. Therefore, also the radial spheroidal functions can be expressed as sum of simpler and well-known functions, as we have seen for the angle functions. An important feature is that the coefficients appearing in the radial functions are obtained from the ones of the angle functions d_r^{mn}. This characteristic gives a big help in terms of time when computing numerical results via computer.

Following are the relationships for the four kinds of radial spheroidal functions normalized by the coefficient:

$$\rho_{mn}(c) = i^{m-n}c^m \Big/ \left[\sum_{r=0,1}^{\infty\prime} d_r^{mn}(c) \frac{(2m+r)!}{r!} \right], \tag{4.14}$$

for the prolate case and $\rho_{mn}(-ic)$ for the oblate one. For detailed analysis of this problem, please refer to Flammer [79] and Li et al. [82] and in the book of Jin [83]

It is to be noticed that the convergence of the series is very slow for small values of $c\xi$. In fact, the expansion is an asymptotic series, being not absolutely convergent for any finite value of $c\xi$. For this reason other kinds of expansion have been implemented for the case of small $c\xi$. The details about these methods can be found in [79], [82] and [83]

The behavior of oblate spheroidal functions will be analyzed in detail. A little variation to the notation will be applied:

$$S_{mn} \rightarrow S_{m,n}$$
$$R_{mn}^{(1)} \rightarrow R_{m,n}^{(1)}$$
$$R_{mn}^{(3)} \rightarrow R_{m,n}^{(3)}$$

4.1.2 The case of one layer coating

This problem was previously considered by Dr. Askarpour and Prof. Uslenghi in [97–99] and analytical solutions have been such that strongly used as a reference to the case of dual layer coating about to be presented in this thesis. Basically, the geometry consists of a metallic prolate/oblate spheroid coated with

a confocal prolate/oblate spheroidal layer made of lossless penetrable material characterized by a real electric permittivity ε_1 amd a real magnetic permeability μ_1, or equivalently by a real propagation constant $k_1 = \sqrt{\varepsilon_1 \mu_1}$ and a real intrinsic impedance $Z_1 = \sqrt{\frac{\varepsilon_1}{\mu_1}}$. The structure is surrounded by an infinite medium (e.g., free space) with real propagation k_0 and real instrinsic impedance Z_0. The primary source is an electric or magnetic dipole located outside of coating layer on the axis of symmetry of the structure (in this case it is *z-axis*). The details of geometries of two problems are presented in Figure 4.3

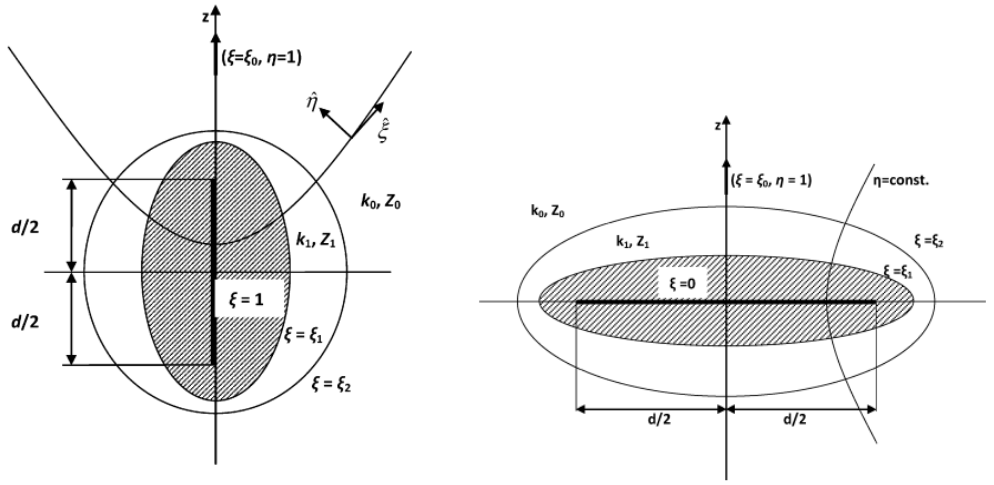

(a) Prolate case (b) Oblate case

Figure 4.3: *The two cases of one layer coating*

In this short section, several properties of elementary dipoles on spheroidal structures will be presented briefly and the details of fields have been fully demonstrated in papers [98, 99]. In Figure 4.4, the confocal distance *d* of prolate spheroids doubles the wavelength of incident wave, far-field radiation pattern is calculated and normalized to its maximum value. The parameters used for the case of Figure 4.4 are $\xi_0 = 2$, $\xi_1 = 1.2$, $\xi_2 = 1.5$.

As can be seen in the graph, the anti-isorefractive coating layer with different characteristic impedance to free space, characterized by parameter ζ, has strong influences on behavior of electric dipole. The radiation pattern is symmetrical as prolate structures are oriented symmetrically around the $z - axis$.

Regarding Figure 4.5, it shows the contour plot of electric field due to magnetic dipole. In this example, $\xi_0 = 2$, $\xi_1 = 0.5$, $\xi_2 = 0.75$ and the confocal

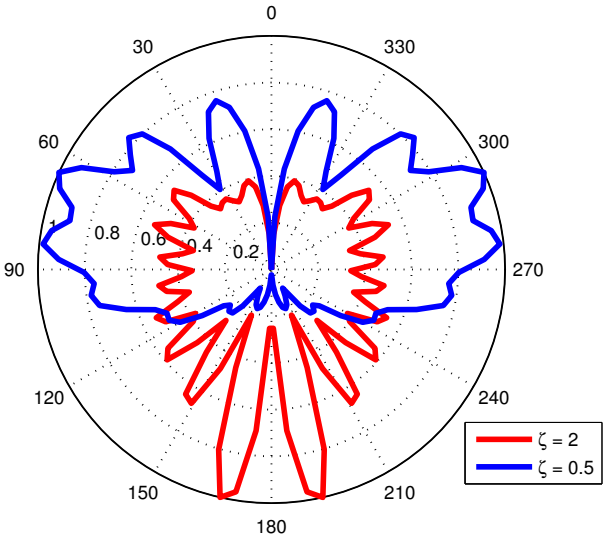

Figure 4.4: *Far field radiation pattern of Magnetic Field H_ϕ of Electric dipole on Prolate spheroids.*

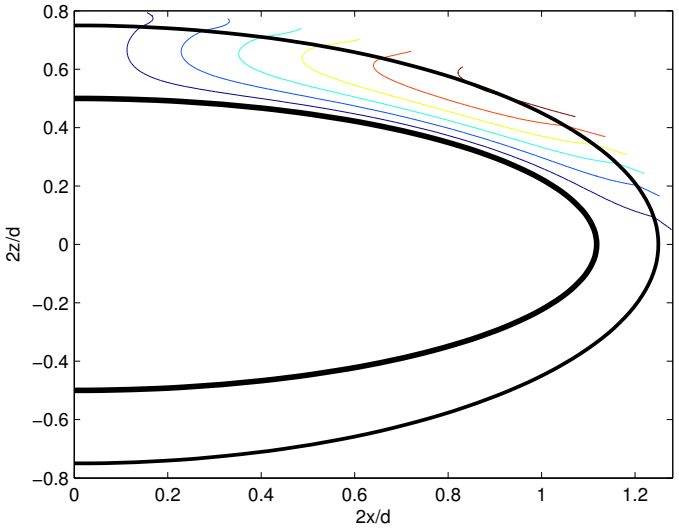

Figure 4.5: *Contour plot of near field E_ϕ of Magnetic dipole on Oblate spheroids.*

distance d of prolate spheroids triples the wavelength of incident wave $d = 3\lambda$. The generalization of this problem by means of a dual-layer coating will be presented rigorously in the next sections.

4.2 Dual-Layer Coating on Spheroidal Coordinates

The problem of radiation by antennas in the presence of spheroidal structures is amenable to an exact analytical solution only if the antenna is located on the symmetry axis of the structure and is axially oriented. Such solutions for electric and magnetic dipole antennas on prolate and oblate metallic spheroids are available in the published literature [100]. If the spheroid is coated with layers of materials penetrable to electromagnetic radiation, an exact solution is still obtainable under two additional conditions: the outer surface of each coating layer is a spheroidal surface confocal to the core spheroid, and the linear, homogeneous and isotropic material in each layer has a propagation constant that is either equal or of opposite sign to the propagation constant of the infinite medium surrounding the structure (the possibility of special anistropies in the coating layer is not considered in this work). A detailed discussion of these conditions is found in [79]. The case of single coating layer has been solved previously in [98] for a prolate spheroid and in [99] for an oblate spheroid.

The two new geometries, oblate and prolate, analyzed in this thesis consist of a metallic spheroid coated by two confocal spheroid layers made of lossless penetrable materials. The first layer characterized by a real electric permittivity ϵ_1 and real magnetic permeability μ_1 or equivalently by a real propagation constant $k_1 = \sqrt{\epsilon_1 \mu_1}$ and real intrinsic impedance $Z_1 = \sqrt{\frac{\mu_1}{\epsilon_1}}$. Those parameters of second layer are ϵ_2, μ_2, Z_2,k_2 respectively and either one of two layers can be DPS or DNG material. The case $k = k_0$ corresponds to an isorefractive coating layer, whereas $k = -k_0$ stands a double negative metamaterial layer. Therefore, in this prolate spheroid coordinate, we are going to consider the radiation Electric dipole and Magnetic dipole in two circumstances. The first case is when layer 1 is DPS, layer 2 is DNG. The second case is the reverse of the first when layer 1 is DNG and layer 2 is DPS. The analysis is conducted in phasor domain with the time-dependence factor $exp(-iwt)$ omitted throughout. As aforementioned, such coordinates like prolate and oblate systems in which wave equation is separable, the eigenfunctions on either side of each penetrable interface depend on propagation constants but not on the intrinsic impedances of the material on either side of interface. Therefore, the analytical determination of modal coefficients is possible and exact solution is obtainable by separation of variables. This is the case for a variety of bodies involving penetrable materials with the same refractive index

(isorefractive media) on both sides of each interface (see, e.g. [85–91]).When DNG layer is considered, an exact solution by separation of variables is possible only if the functions that depend on variables that vary along each interface remain unchanged when the refractive index changes sign. This is the case for elliptic cylinders [92], elliptical cylindrical cavities [93], [94], paraboloids of revolution under axial plane wave incidence [95], oblate spheroidal cavities excited by axially located and oriented dipoles [96, 97], and the spheroidal structures considered herein.

The goemetry of each case, prolate and oblate, is detailed in the next section, in which the boundary-value problem is presented and solved exactly for electric and magnetic sources.

CHAPTER 5

Dual-layer coating on Prolate Spheroids

The problem of radiation by antennas in the presence of spheroidal structures is amenable to an exact analytical solution only if the antenna is located on the symmetry axis of the structure and is axially oriented. Such solutions for electric and magnetic dipole antennas on prolate and oblate metallic spheroids are available in the published literature (see e.g [84]). If the spheroid is coated with layers of materials penetrable to electromagnetic radiation, an exact solution is still obtainable under two additional conditions: the outer surface of each coating layer is a spheroidal surface confocal to the core spheroid, and the linear, homogeneous and isotropic material in each layer has a propagation constant that is either equal or of opposite sign to the propagation constant of the infinite medium surrounding the structure (the possibility of special anistropies in the coating layer is not considered in this work). A detailed discussion of these conditions is found in [98, 99]. As detailed in the previous chapter, the case of single coating layer has been solved previously in [98] for a prolate spheroid and in [99, 100] for an oblate spheroid.

The purpose of this work is to analyze the effects that a double-layer coating, with one layer being isorefractive and the other layer anti-isorefractive to the surrounding space, has on the fields trapped inside the layers and on the far-field pattern. The analysis is performed in section II for prolate spheroidal structures

and in section III for oblate spheroidal structures, by expanding the field into infinite series of spheroidal wave functions and determining the modal expansion coefficients by imposing the boundary conditions at the various interfaces and the radiation condition at infinity. The explicit analytical determination of the expansion coefficients is possible because the angular spheroidal functions are even functions of the propagation constant, thus allowing for one-on-one mode matching even when anti-isorefractive layers are present. The notation for the spheroidal functions is that of Flammer [79, 84] and the analysis is performed in the phasor domain with a time-dependence factor $exp(i-\omega t)$ omitted throughout.

Numerical results based on the obtained exact analytical expressions for the fields inside the layers and the radiated field are shown and discussed in section IV, for several parameters involved: geometrical shape and dimensions of the spheroids and coating layers in terms of wavelength; location of the layers (inner layer isorefractive or anti-isorefractive); and intrinsic impedances of the two layers. Some conclusions are drawn on the influence of the parameters on the lobing structure of the far-field pattern and on the resonances set up inside the layers.

5.1 Geometry of the problem

A cross-section of the prolate spheroidal structure in a plane containing the axis z of symmetry is shown in Figure 5.1. The structure is centered at the origin of coordinates, with the $z = 0$ plane as the equatorial symmetry plane. The prolate spheroidal coordinates (η, ξ, ϕ) are related to the rectangular coordinate *(x, y, z)* by

$$x = \frac{d}{2}\sqrt{(\xi^2 - 1)(1 - \eta^2)}\cos\phi$$
$$y = \frac{d}{2}\sqrt{(\xi^2 - 1)(1 - \eta^2)}\sin\phi$$
$$z = \frac{d}{2}\xi\eta$$

where $-1 \leq \eta \leq 1, -1 \leq \xi \leq \infty$ and $0 \leq \phi \leq 2\pi$. The parameter d is the interfocal distance.

The dashed area in Figure 5.1 is the cross-section of a metallic prolate spheroid with surface $\xi = \xi_1$, that becomes a thin wire of length *d* in the limit $\xi_1 = 1$. It is coated by two confocal layers of outer surface, at $\xi = \xi_2$ inner layer made of an isotropic and uniform material characterized by a real propagation constant k_1 and a real intrinsic impedance $Z_1 = {Y_1}^{-1}$. At $\xi = \xi_3$ outer layer made of an isotropic and uniform material characterized by a real propagation constant k_2 and a real intrinsic impedance $Z_2 = {Y_2}^{-1}$. The structure is surrounded by

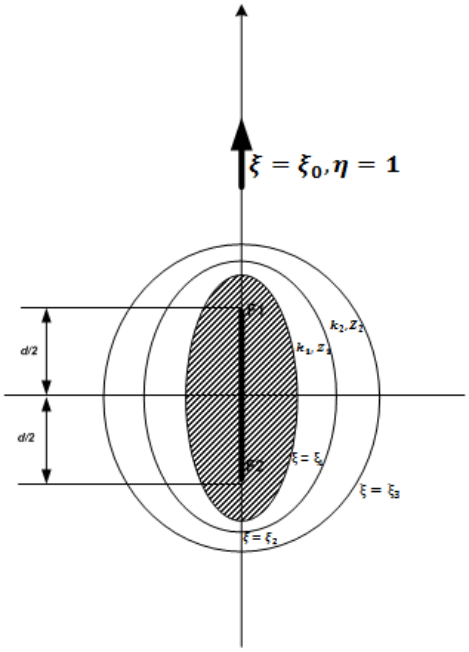

Figure 5.1: *Geometry of the problem*

a medium characterized by a real positive propagation constant k_0 and a real positive intrinsic impedance $Z_0 = {Y_0}^{-1}$.

The primary source is an electric or magnetic Hertzian dipole located on the axis z of symmetry at $(\xi = \xi_0, \eta = 1)$ and axially oriented. Even though the analysis can be performed for a dipole source inside the coating layer, i.e for $\xi_1 < \xi_0 < \xi_2$, for simplicity the following derivations are carried out only for the case $\xi_0 > \xi_2$ of a source outside the scattering structure.

5.2 Electric dipole source

5.2.1 Interpretation of the fields

If the electric dipole at $(\xi = \xi_0, \eta = 1)$ is characterized by the Hertz vector

$$\mathbf{\Pi_e}^{\mathbf{i}} = \hat{z}\frac{e^{jkr}}{kr} \tag{5.1}$$

where *R* is the distance from the dipole to the observation point, then the electric field $\underline{E}$ and the magnetic field $\underline{H}$ are everywhere of the type

$$\begin{aligned} \mathbf{E} &= E_\xi(\xi,\eta)\,\hat{\xi} + E_\eta(\xi,\eta)\,\hat{\eta}, \quad E_\phi = 0 \\ \mathbf{H} &= H_\phi(\xi,\eta)\,\hat{\phi}, \quad H_\xi = H_\eta = 0 \end{aligned} \tag{5.2}$$

In particular the incident field component ${H_\phi}^i$ corresponding to the source in (5.1) may be written as infinite series of prolate spheroidal wave functions [84]

$$H_\phi^i = \frac{2k^2 Y_0}{\sqrt{\xi_0^2-1}} \sum_{n=1}^{\infty} \frac{(-i)^{n-1}}{\rho_{1,n} N_{1,n}} R_{1,n}^{(1)}(c,\xi_<)\, R_{1,n}^{(3)}(c,\xi_>)\, S_{1,n}(c,\eta), \quad \xi_{\lessgtr} = \begin{matrix} min \\ max \end{matrix} (\xi,\xi_0) \tag{5.3}$$

where the dimensionless parameter

$$c = \frac{k_o d}{2} \tag{5.4}$$

and Flammer's notation has been used [79]. The coordinates $\xi_<$ ($\xi_>$) are the smaller (larger) between ξ and ξ_0. In order to impose the boundary condition across the interface $\xi = \xi_2$, it is necessary to consider also the component ${E_\eta}^i$, which is obtained from ${H_\phi}^i$ as

$$\begin{aligned} E_\eta^i &= \frac{iZ_0}{c}\sqrt{\frac{\xi^2-1}{\xi^2-\eta^2}}\left(\frac{\partial}{\partial\xi} + \frac{\xi}{\xi^2-1}\right) H_\phi^i \\ &= \frac{2ik^2}{c\sqrt{\xi_0^2-1}}\sqrt{\frac{\xi^2-1}{\xi^2-\eta^2}} \sum_{n=1}^{\infty} \frac{(-1)^{n-1}}{\rho_{1,n} N_{1,n}} S_{1,n}(c,\eta) \times \\ &\begin{cases} R_{1,n}^{(3)}(c,\xi_0)\, C_n^{(1)}(c,\xi), & \xi < \xi_0 \\ R_{1,n}^{(1)}(c,\xi_0)\, C_n^{(3)}(c,\xi), & \xi > \xi_0 \end{cases} \end{aligned} \tag{5.5}$$

where

$$C_{(\pm c,\xi)}^{(h)} = R_{1,n}^{(h)\prime}(\pm c,\xi) + \frac{\xi}{\xi^2-1} R_{1,n}^{(h)}(\pm c,\xi), \quad (h = 1,3)$$

where the prime means derivative with respect to ξ.

If the expressions akin to (5.3) and (5.5) are written for the field components inside two coating layers, they would contain the parameters:

$$c_{1,2} = \frac{k_{1,2} d}{2} \tag{5.6}$$

instead of c, in both the radial functions $R_{1,n}^{(1)}$, $R_{1,n}^{(3)}$ and the angular functions $S_{1,n}$. The explicit, analytical determination is possible only if the angular function $S_{1,n}$ is the same on both sides of the interface $\xi = \xi_2$; since $S_{1,n}$ is an even function of parameter c (this is not true for the radial function!). This occurs in two cases: either $c_{1,2} = c$ (i.e. $k_1 = k_0$), meaning that the coating layers and the surrounding medium have the same index of refraction (isorefractive layer); or $c_{1,2} = -c$ (i.e. $k_{1,2} = -k_0$), meaning that the coating layer is a DNG metamaterial whose index of refraction is the negative of the index of refraction of the surrounding medium (anti-isorefractive layer).

In all the following formulas, the upper sign applies to an isorefractive coating layer, and the lower sign to an anti-isorefractive coating layer. Since the electric dipole is located outside of two lossless dielectric layers, so $\xi_0 > \xi_3$ and $l = 1$ for inside layer ($\xi_1 \leq \xi \leq \xi_2$) and $l = 2$ for outside layer ($\xi_2 \leq \xi \leq \xi_3$): Magnetic and Electric fields inside two coating layers are respectively expressed by following formulas, respectively:

$$H_{l,\phi}^{(\pm)} = \frac{2k^2 Y_l}{\sqrt{\xi_0^2 - 1}} \sum_{n=1}^{\infty} \frac{(-i)^{n-1}}{\rho_{1,n} N_{1,n}} R_{1,n}^{(3)}(c, \xi_0)\, S_{1,n}(c, \eta) \times \\ \times \left[a_{l,n}^{\pm} R_{1,n}^{(1)}(\pm c, \xi) + b_{l,n}^{\pm} \times R_{1,n}^{(3)}(\pm c, \xi) \right], \tag{5.7}$$

And Electric field:

$$E_{l,\eta}^{(\pm)} = \frac{\pm 2ik^2}{c\sqrt{\xi_0^2 - 1}} \sqrt{\frac{\xi^2 - 1}{\xi^2 - \eta^2}} \sum_{n=1}^{\infty} \frac{(-i)^{n-1}}{\rho_{1,n} N_{1,n}} R_{1,n}^{(3)}(c, \xi_0)\, S_{1,n}(c, \eta) \times \\ \times \left\{ a_{l,n}^{\pm} C_n^{(1)}(\pm c, \xi) + b_{l,n}^{\pm} C_n^{(3)}(\pm c, \xi) \right\}. \tag{5.8}$$

The scattered fields outside the structure ($\xi_3 \leq \xi$) are expressed as:
$m = 1$ for the first case (outside layer is anti-isorefractive);
$m = 2$ for the second case (outside layer is isorefractive)

Scattered Magnetic Field:

$$H_{\phi}^{s,m} = \frac{2k^2 Y}{\sqrt{\xi_0^2 - 1}} \sum_{n=1}^{\infty} \frac{(-i)^{n-1}}{\rho_{1,n} N_{1,n}} {c_n}^m R_{1,n}^{(3)}(c, \xi_0)\, R_{1,n}^{(3)}(c, \xi)\, S_{1,n}(c, \eta), \tag{5.9}$$

Scattered Electric Field:

$$E_{\phi}^{s,m} = \frac{2ik^2}{c\sqrt{\xi_0^2 - 1}} \sqrt{\frac{\xi^2 - 1}{\xi^2 - \eta^2}} \sum_{n=1}^{\infty} \frac{(-i)^{n-1}}{\rho_{1,n} N_{1,n}} {c_n}^m R_{1,n}^{(3)}(c, \xi_0)\, S_{1,n}(c, \eta)\, C_{1,n}^{(3)}(c, \xi). \tag{5.10}$$

With the reference to spherical cooridnates (r, θ, ϕ) with the origin at the center of the structure, the scatterd far field is:

$$H_{\phi}^{s} \mid_{c\xi \to \infty} \approx \frac{e^{jkr}}{kr} \frac{2k^2 Y_0}{\sqrt{\xi_0^2 - 1}} \sum_{n=1}^{\infty} \frac{(-i)^{(n-1)}}{\rho_{1,n} N_{1,n}} {c_n}^m R_{1,n}^{(3)}(c, \xi_0) \, S_{1,n}(c, cos\theta) \,. \quad (5.11)$$

Properties of Angular Functions and Radial Functions

Angular function $S_{1,n}$ is an even function of c :
$S_{1,n}(c, \xi) = S_{1,n}(-c, \xi)$.
We assume the notations explicitly for the case Prolate:

$$C_{(\pm c,\xi)}^{(k)} = R_{1,n}^{(k)\prime}(\pm c, \xi) + \frac{\xi}{\xi^2 - 1} R_{1,n}^{(k)}(\pm c, \xi) \,. \quad (5.12)$$

According to Flammer's notes [79], properties of radial functions can be written as:

$$R_{m,n}^{(3,4)}(c, \xi) = {R_{m,n}}^{(1)}(c, \xi) \pm i {R_{m,n}}^{(2)}(c, \xi)$$
$$\Delta \left\langle {R_{m,n}}^{(1)}(c, \xi) \, {R_{m,n}}^{(2)}(c, \xi) \right\rangle =$$
$$ {R_{m,n}}^{(1)}(c, \xi) \frac{d\left({R_{m,n}}^{(2)}(c, \xi)\right)}{d\xi} - {R_{m,n}}^{(2)}(c, \xi) \frac{d\left({R_{m,n}}^{(1)}(c, \xi)\right)}{d\xi} = \frac{1}{c(\xi^2 - 1)}. \quad (5.13)$$

Therefore:

$$C_{(c,\xi)}^{(1)} R_{(c,\xi)}^{(3)} - C_{(c,\xi)}^{(3)} R_{(c,\xi)}^{(1)} = \frac{-i}{c(\xi^2 - 1)}$$
$$C_{(-c,\xi)}^{(1)} R_{(-c,\xi)}^{(3)} - C_{(-c,\xi)}^{(3)} R_{(-c,\xi)}^{(1)} = \frac{i}{c(\xi^2 - 1)} \quad (5.14)$$

5.2.2 Applying Boundary Conditions

Case 1

Description: Outer layer is anti-isorefractive; inner layer is isorefractive
Applying boundary conditions for the tangential components of Electric field and Magnetic field at $\xi = \xi_1$, $\xi = \xi_2$ and $\xi = \xi_3$, we have five linear equations as follows:
$E_{1\eta}^{(+)} \mid_{\xi=\xi_1} = 0$

$E_{1\eta}^{(+)}\mid_{\xi=\xi_2} = E_{2\eta}^{(-)}\mid_{\xi=\xi_2}$; $H_{1\phi}^{(+)}\mid_{\xi=\xi_2} = H_{2\phi}^{(-)}\mid_{\xi=\xi_2}$;

$E_{2\eta}^{(-)}\mid_{\xi=\xi_3} = \left(E_{\eta}^{s,1} + E_{\eta}^{i}\right)\mid_{\xi=\xi_3}$;
$H_{2\phi}^{(-)}\mid_{\xi=\xi_3} = \left(H_{\phi}^{s,1} + H_{\phi}^{i}\right)\mid_{\xi=\xi_3}$.

Expansion coefficients: c_n^1; $a_{2,n}^{(-)}$; $b_{2,n}^{(-)}$; $a_{1,n}^{(+)}$ and $b_{1,n}^{(+)}$ will be determined by solving this system of linear equations.

Case 2

Description: Outer layer is isorefractive; inner layer is Anti-isorefractive
Applying boundary conditions for the tangential components of Electric field and Magnetic field at $\xi = \xi_1$, $\xi = \xi_2$ and $\xi = \xi_3$, we have five linear equations as follows:
$E_{1\eta}^{(-)}\mid_{\xi=\xi_1} = 0$

$E_{1\eta}^{(-)}\mid_{\xi=\xi_2} = E_{2\eta}^{(+)}\mid_{\xi=\xi_2}$; $H_{1\phi}^{(-)}\mid_{\xi=\xi_2} = H_{2\phi}^{(+)}\mid_{\xi=\xi_2}$;

$E_{2\eta}^{(+)}\mid_{\xi=\xi_3} = \left(E_{\eta}^{s,2} + E_{\eta}^{i}\right)\mid_{\xi=\xi_3}$;
$H_{2\phi}^{(+)}\mid_{\xi=\xi_3} = \left(H_{\phi}^{s,2} + H_{\phi}^{i}\right)\mid_{\xi=\xi_3}$.

Expansion coefficients: c_n^2; $a_{2,n}^{(+)}$; $b_{2,n}^{(+)}$; $a_{1,n}^{(-)}$ and $b_{1,n}^{(-)}$ will be determined by solving this system of linear equations.

5.2.3 Exact solutions

Case 1

By applying Cramer's rule, exact solutions for expansion coefficients a_1; b_1; a_2; b_2; and$c$ can be retrieved as follows:

$$a_1^{(+)} = \frac{-C_{(c,\xi_1)}^{(3)}\zeta_2}{c^2\left(\xi_3^2-1\right)\left(\xi_2^2-1\right)\Delta} \tag{5.15}$$

$$b_1^{(+)} = \frac{C_{(c,\xi_1)}^{(1)}\zeta_2}{c^2\left(\xi_3^2-1\right)\left(\xi_2^2-1\right)\Delta} \tag{5.16}$$

$$a_2^{(-)} = \frac{i}{c^2\left(\xi_3^2-1\right)\Delta} \times \left\langle \zeta_2 R_{(-c,\xi_2)}^{(3)}\left[C_{(c,\xi_1)}^{(1)}C_{(c,\xi_2)}^{(3)} - C_{(c,\xi_2)}^{(1)}C_{(c,\xi_1)}^{(3)}\right] + \zeta_1 C_{(-c,\xi_2)}^{(3)}\left[C_{(c,\xi_1)}^{(1)}R_{(c,\xi_2)}^{(3)} - C_{(c,\xi_1)}^{(3)}R_{(c,\xi_2)}^{(1)}\right]\right\rangle, \tag{5.17}$$

$$b_2^{(-)} = \frac{-i}{c^2\left(\xi_3^2-1\right)\Delta} \times \left\langle \zeta_2 R_{(-c,\xi_2)}^{(1)} \left[C_{(c,\xi_1)}^{(1)} C_{(c,\xi_2)}^{(3)} - C_{(c,\xi_2)}^{(1)} C_{(c,\xi_1)}^{(3)} \right] + \zeta_1 C_{(-c,\xi_2)}^{(1)} \left[C_{(c,\xi_1)}^{(1)} R_{(c,\xi_2)}^{(3)} - C_{(c,\xi_1)}^{(3)} R_{(c,\xi_2)}^{(1)} \right] \right\rangle. \tag{5.18}$$

We assume the notations:

$$\Delta_1 = \zeta_2 \left(C_{(c,\xi_1)}^{(1)} C_{(c,\xi_2)}^{(3)} - C_{(c,\xi_2)}^{(1)} C_{(c,\xi_1)}^{(3)} \right) \left(C_{(-c,\xi_3)}^{(1)} R_{(-c,\xi_2)}^{(3)} - C_{(-c,\xi_3)}^{(3)} R_{(-c,\xi_2)}^{(1)} \right) - \zeta_1 \left(C_{(c,\xi_1)}^{(1)} R_{(c,\xi_2)}^{(3)} - C_{(c,\xi_1)}^{(3)} R_{(c,\xi_2)}^{(1)} \right) \left(C_{(-c,\xi_2)}^{(1)} C_{(-c,\xi_3)}^{(3)} - C_{(-c,\xi_3)}^{(1)} C_{(-c,\xi_2)}^{(3)} \right)$$

$$\Delta_2 = \zeta_2 \left(C_{(c,\xi_1)}^{(1)} C_{(c,\xi_2)}^{(3)} - C_{(c,\xi_2)}^{(1)} C_{(c,\xi_1)}^{(3)} \right) \left(R_{(-c,\xi_3)}^{(1)} R_{(-c,\xi_2)}^{(3)} - R_{(-c,\xi_2)}^{(1)} R_{(-c,\xi_3)}^{(3)} \right) - \zeta_1 \left(C_{(-c,\xi_2)}^{(1)} R_{(-c,\xi_3)}^{(3)} - C_{(-c,\xi_2)}^{(3)} R_{(-c,\xi_3)}^{(1)} \right) \left(C_{(c,\xi_1)}^{(1)} R_{(c,\xi_2)}^{(3)} - C_{(c,\xi_1)}^{(3)} R_{(c,\xi_2)}^{(1)} \right)$$

in which $\Delta = R_{(c,\xi_3)}^{(3)} \Delta_1 + C_{(c,\xi_3)}^{(3)} \zeta_2 \Delta_2$ and coefficient c is retrieved as:

$$c^1 = \frac{-\left[R_{(c,\xi_3)}^{(1)} \Delta_1 + C_{(c,\xi_3)}^{(1)} \zeta_2 \Delta_2 \right]}{\Delta}. \tag{5.19}$$

Case 2

By applying Cramer's rule, exact solutions for expansion coefficients a_1; b_1; a_2; b_2; and$c$ can be retrieved as follows:

$$a_{1,n}^{(-)} = \frac{-C_{(-c,\xi_1)}^{(3)} \zeta_2}{c^2\left(\xi_3^2-1\right)\left(\xi_2^2-1\right)\Delta} \tag{5.20}$$

$$b_{1,n}^{(-)} = \frac{C_{(-c,\xi_1)}^{(1)} \zeta_2}{c^2\left(\xi_3^2-1\right)\left(\xi_2^2-1\right)\Delta} \tag{5.21}$$

$$a_{2,n}^{(+)} = \frac{i}{c^2\left(\xi_3^2-1\right)\Delta} \times \left\langle \zeta_2 R_{(c,\xi_2)}^{(3)} \left[C_{(-c,\xi_1)}^{(1)} C_{(-c,\xi_2)}^{(3)} - C_{(-c,\xi_2)}^{(1)} C_{(-c,\xi_1)}^{(3)} \right] + \zeta_1 C_{(c,\xi_2)}^{(3)} \left[C_{(-c,\xi_1)}^{(1)} R_{(-c,\xi_2)}^{(3)} - C_{(-c,\xi_1)}^{(3)} R_{(-c,\xi_2)}^{(1)} \right] \right\rangle \tag{5.22}$$

$$b_{2,n}^{(+)} = \frac{-i}{c^2\left(\xi_3^2-1\right)\Delta} \times \left\langle \zeta_2 R_{(c,\xi_2)}^{(1)} \left[C_{(c,\xi_1)}^{(1)} C_{(-c,\xi_2)}^{(3)} - C_{(-c,\xi_2)}^{(1)} C_{(-c,\xi_1)}^{(3)} \right] + \zeta_1 C_{(c,\xi_2)}^{(1)} \left[C_{(-c,\xi_1)}^{(1)} R_{(-c,\xi_2)}^{(3)} - C_{(-c,\xi_1)}^{(3)} R_{(-c,\xi_2)}^{(1)} \right] \right\rangle. \tag{5.23}$$

We assume the notations:

$$\Delta_1 = \zeta_1 \left(C_{(c,\xi_2)}^{(1)} C_{(c,\xi_3)}^{(3)} - C_{(c,\xi_3)}^{(1)} C_{(c,\xi_2)}^{(3)} \right) \left(C_{(-c,\xi_1)}^{(1)} R_{(-c,\xi_2)}^{(3)} - C_{(-c,\xi_1)}^{(3)} R_{(-c,\xi_2)}^{(1)} \right)$$

$$- \zeta_2 \left(C^{(1)}_{(c,\xi_3)} R^{(3)}_{(c,\xi_2)} - C^{(3)}_{(c,\xi_3)} R^{(1)}_{(c,\xi_2)} \right) \left(C^{(1)}_{(-c,\xi_1)} C^{(3)}_{(-c,\xi_2)} - C^{(1)}_{(-c,\xi_2)} C^{(3)}_{(-c,\xi_1)} \right)$$

$$\Delta_2 = \zeta_2 \left(C^{(1)}_{(-c,\xi_1)} C^{(3)}_{(-c,\xi_2)} - C^{(1)}_{(-c,\xi_2)} C^{(3)}_{(-c,\xi_1)} \right) \left(R^{(1)}_{(c,\xi_3)} R^{(3)}_{(c,\xi_2)} - R^{(1)}_{(c,\xi_2)} R^{(3)}_{(c,\xi_3)} \right)$$

$$- \zeta_1 \left(C^{(1)}_{(c,\xi_2)} R^{(3)}_{(c,\xi_3)} - C^{(3)}_{(c,\xi_2)} R^{(1)}_{(c,\xi_3)} \right) \left(C^{(1)}_{(-c,\xi_1)} R^{(3)}_{(-c,\xi_2)} - C^{(3)}_{(-c,\xi_1)} R^{(1)}_{(-c,\xi_2)} \right)$$

in which $\Delta = R^{(3)}_{(c,\xi_3)} \Delta_1 + C^{(3)}_{(c,\xi_3)} \zeta_2 \Delta_2$. Coefficient c can be retrieved as:

$$c^2 = \frac{- \left[R^{(1)}_{(c,\xi_3)} \Delta_1 + C^{(1)}_{(c,\xi_3)} \zeta_2 \Delta_2 \right]}{\Delta}. \tag{5.24}$$

5.2.4 Numerical results

Since all the field components can be computed using E_ϕ and H_ϕ, we only consider these two quantities in this section. In order to lower the computational cost of the problem and increase the accuracy of computations, incident fields are evaluated using closed form expressions for dipole radiation. We considered up to thirty terms in summations needed for computing the fields to achieve a convergence error of less than one percent in our calculations.

All the simulations are done with the parameters of: $d = 2$; $\lambda = 1$; $\xi_0 = 4.1$; $\xi_1 = 2$; $\xi_2 = 2.8$ and $\xi_3 = 3$.

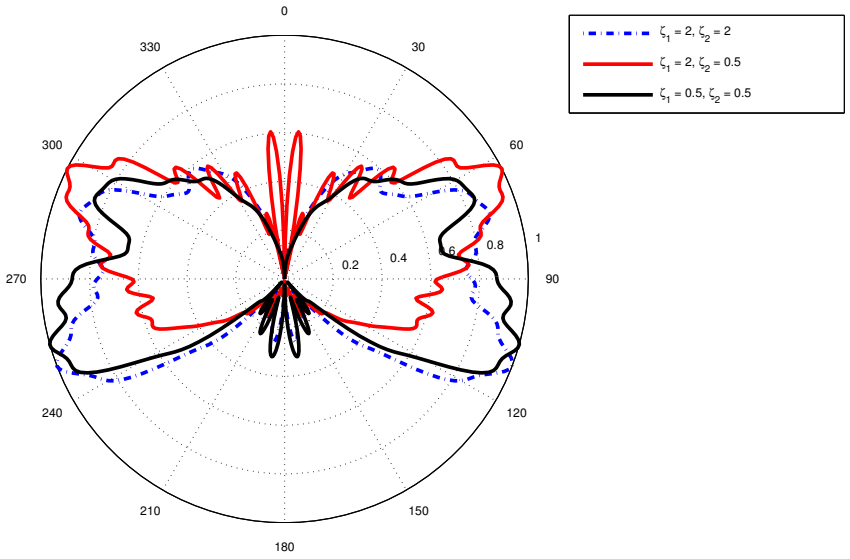

Figure 5.2: *The Scattered Magnetic Far Field of an electric Dipole when Layer 1 is Isorefractive and Layer 2 is Anti-Isorefractive with different* ζ_1, ζ_2

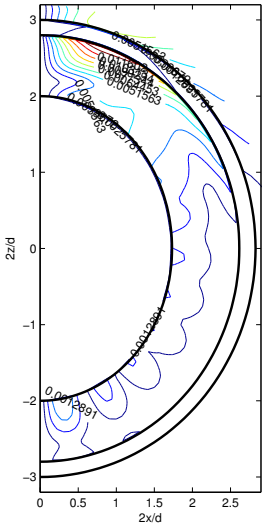

Figure 5.3: *Contour Plot of Magnetic Field of an electric Dipole in the case layer 1 is Isorefractive and layer 2 is Anti-Isorefractive with* $\zeta_1 = 2$, $\zeta_2 = 2$

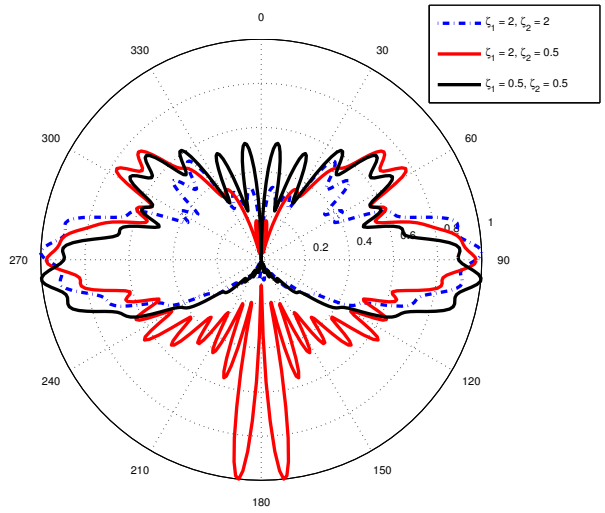

Figure 5.4: *The Scattered Magnetic Far Field of an electric Dipole when layer 1 is Anti-Isorefractive and layer 2 is Isorefractive with different* ζ_1, ζ_2

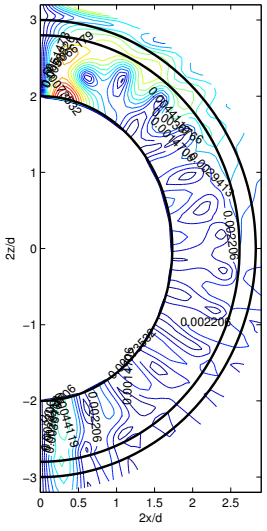

Figure 5.5: *Contour Plot of Magnetic Field of an electric Dipole in the case layer 1 is Anti-Isorefractive and layer 2 is Isorefractive with* $\zeta_1 = 2$, $\zeta_2 = 0.5$

5.3 Magnetic dipole source

5.3.1 Interpretation of the fields

If the magnetic dipole at $(\xi = \xi_0, \eta = 1)$ is characterized by the Hertz vector

$$\mathbf{\Pi_m}^{\mathbf{i}} = \hat{z}\frac{e^{jkr}}{kr} \tag{5.25}$$

generates electric and magnetic fields that are everywhere of the type

$$\begin{aligned} \mathbf{E} &= E_\phi(\xi,\eta)\,\hat{\phi}, \quad E_\xi = E_\eta = 0 \\ \mathbf{H} &= H_\xi(\xi,\eta)\,\hat{\xi} + H_\eta(\xi,\eta)\,\hat{\eta}, \quad H_\phi = 0 \end{aligned} \tag{5.26}$$

It should be noted that the fields cannot be simply obtained by duality from electric dipole case, because duality would require that the core spheroid be a perfect magnetic conductor. The incident field components ${E_\phi}^i$ and ${H_\eta}^i$ may be written as the infinite series

$$E_\phi^i = \frac{-2k^2 Z_0}{\sqrt{\xi_0^2-1}}\sum_{n=1}^{\infty}\frac{(-i)^{n-1}}{\rho_{1,n}N_{1,n}}R_{1,n}^{(1)}(c,\xi_<)\,R_{1,n}^{(3)}(c,\xi_>)\,S_{1,n}(c,\eta),$$

$$\xi_{\lessgtr} = \begin{matrix} min \\ max \end{matrix}(\xi,\xi_0), \tag{5.27}$$

$$H_\eta^i = \frac{2ik_0^2}{c\sqrt{\xi_0^2-1}}\sqrt{\frac{\xi^2-1}{\xi^2-\eta^2}}\sum_{n=1}^{\infty}\frac{(-i)^{n-1}}{\rho_{1,n}N_{1,n}}S_{1,n}(c,\eta)\times \begin{cases} R_{1,n}^{(3)}(c,\xi_0)\,C_n^{(1)}(c,\xi), & \xi<\xi_0 \\ R_{1,n}^{(1)}(c,\xi_0)\,C_n^{(3)}(c,\xi), & \xi>\xi_0 \end{cases} \tag{5.28}$$

In all the following formulas, the upper sign applies to an isorefractive coating layer, and the lower sign to an anti-isorefractive coating layer. Since the electric dipole is located outside of two lossless dielectric layers, so $\xi_0 > \xi_3$ and $l = 1$ for inside layer $(\xi_1 \le \xi \le \xi_2)$ and $l = 2$ for outside layer $(\xi_2 \le \xi \le \xi_3)$. Magnetic and Electric fields inside two coating layers are respectively expressed by following formulas Regarding Electric Field:

$$E_{l,\phi}^{(\pm)} = \frac{-2k^2 Z_l}{\sqrt{\xi_0^2-1}}\sum_{n=1}^{\infty}\frac{(-i)^{n-1}}{\rho_{1,n}N_{1,n}}R_{1,n}^{(3)}(c,\xi_0)\,S_{1,n}(c,\eta)\times \times\left[a_{l,n}^{\pm}R_{1,n}^{(1)}(\pm c,\xi)+b_{l,n}^{\pm}\times R_{1,n}^{(3)}(\pm c,\xi)\right], \tag{5.29}$$

And Magnetic field:

$$H_{l,\eta}^{(\pm)} = \frac{\pm 2ik^2}{c\sqrt{\xi_0^2-1}}\sqrt{\frac{\xi^2-1}{\xi^2-\eta^2}}\sum_{n=1}^{\infty}\frac{(-i)^{n-1}}{\rho_{1,n}N_{1,n}}R_{1,n}^{(3)}(c,\xi_0)\,S_{1,n}(c,\eta)\times \\ \times\left\{a_{l,n}^{\pm}C_n^{(1)}(\pm c,\xi)+b_{l,n}^{\pm}C_n^{(3)}(\pm c,\xi)\right\}. \tag{5.30}$$

The scattered fields outside the structure ($\xi_3 \leq \xi$) are expressed as:
$m = 1$ for the first case (outside layer is anti-isorefractive);
$m = 2$ for the second case (outside layer is isorefractive)
Scattered Magnetic Field:

$$H_{\eta}^{s,m} = \frac{2ik^2}{c\sqrt{\xi_0^2-1}}\sqrt{\frac{\xi^2-1}{\xi^2-\eta^2}}\sum_{n=1}^{\infty}\frac{(-i)^{n-1}}{\rho_{1,n}N_{1,n}}{c_n}^m R_{1,n}^{(3)}(c,\xi_0)\,S_{1,n}(c,\eta)\,C_n^{(3)}(c,\xi), \tag{5.31}$$

Scattered electric Field:

$$E_{\phi}^{s,m} = \frac{2k^2Y_0}{\sqrt{\xi_0^2-1}}\sum_{n=1}^{\infty}\frac{(-i)^{n-1}}{\rho_{1,n}N_{1,n}}{c_n}^m R_{1,n}^{(3)}(c,\xi_0)\,R_{1,n}^{(3)}(c,\xi)\,S_{1,n}(c,\eta), \tag{5.32}$$

And Scattered magnetic field:

$$H_{\phi}^{s,m} = \frac{2ik^2}{c\sqrt{\xi_0^2-1}}\sqrt{\frac{\xi^2-1}{\xi^2-\eta^2}}\sum_{n=1}^{\infty}\frac{(-i)^{n-1}}{\rho_{1,n}N_{1,n}}{c_n}^m R_{1,n}^{(3)}(c,\xi_0)\,S_{1,n}(c,\eta)\,C_{1,n}^{(3)}(c,\xi). \tag{5.33}$$

With reference to spherical cooridnates (r,θ,ϕ) with the origin at the center of the structure, the scattered far field is:

$$E_{\phi}^{s}\mid_{c\xi\to\infty} \approx \frac{e^{jkr}}{kr}\frac{2k^2Z_0}{\sqrt{\xi_0^2-1}}\sum_{n=1}^{\infty}\frac{(-i)^{n-1}}{\rho_{1,n}N_{1,n}}{\gamma_n}^m R_{1,n}^{(3)}(c,\xi_0)\,S_{1,n}(c,cos\theta), \tag{5.34}$$

5.3.2 Applying Boundary Conditions

Case 1

Description: Outer layer is anti-isorefractive; inner layer is isorefractive
Applying boundary conditions for the tangential components of Electric field and Magnetic field at $\xi = \xi_1$; $\xi = \xi_2$ and $\xi = \xi_3$, we have five linear equations as follows

$E_{1\phi}^{(+)} \mid_{\xi=\xi_1} = 0$

$E_{1\phi}^{(+)} \mid_{\xi=\xi_2} = E_{2\phi}^{(-)} \mid_{\xi=\xi_2}; H_{1\eta}^{(+)} \mid_{\xi=\xi_2} = H_{2\eta}^{(-)} \mid_{\xi=\xi_2};$

$E_{2\phi}^{(-)} \mid_{\xi=\xi_3} = \left(E_{\phi}^{s,1} + E_{\phi}^{i}\right) \mid_{\xi=\xi_3};$
$H_{2\eta}^{(-)} \mid_{\xi=\xi_3} = \left(H_{\eta}^{s,1} + H_{\eta}^{i}\right) \mid_{\xi=\xi_3}.$

Expansion coefficients: c_n^1; $a_{2,n}^{(-)}$; $b_{2,n}^{(-)}$; $a_{1,n}^{(+)}$ and $b_{1,n}^{(+)}$ will be determined by solving this system of linear equations.

Case 2

Description: Outer layer is Isorefractive; inner layer is Anti-isorefractive
Applying boundary conditions for the tangential components of Electric field and Magnetic field at $\xi = \xi_1$; $\xi = \xi_2$ and $\xi = \xi_3$, we have 5 linear equations as follows
$E_{1\phi}^{(-)} \mid_{\xi=\xi_1} = 0$

$E_{1\phi}^{(-)} \mid_{\xi=\xi_2} = E_{2\phi}^{(+)} \mid_{\xi=\xi_2}; H_{1\eta}^{(-)} \mid_{\xi=\xi_2} = H_{2\eta}^{(+)} \mid_{\xi=\xi_2};$

$E_{2\phi}^{(+)} \mid_{\xi=\xi_3} = \left(E_{\phi}^{s,2} + E_{\phi}^{i}\right) \mid_{\xi=\xi_3};$
$H_{2\eta}^{(+)} \mid_{\xi=\xi_3} = \left(H_{\eta}^{s,2} + H_{\eta}^{i}\right) \mid_{\xi=\xi_3}.$

Expansion coefficients: c_n^2; $a_{2,n}^{(+)}$; $b_{2,n}^{(+)}$; $a_{1,n}^{(-)}$ and $b_{1,n}^{(-)}$ will be determined by solving this system of linear equations.

5.3.3 Exact solutions

Case 1

By applying Cramer's rule, exact solutions for expansion coefficients c_n^1; $a_{2,n}^{(-)}$; $b_{2,n}^{(-)}$; $a_{1,n}^{(+)}$ and $b_{1,n}^{(+)}$ can be retrieved as follows

$$a_{1,n}^{(+)} = \frac{R_{(c,\xi_1)}^{(3)} \zeta_1 \zeta_2}{c^2 \left(\xi_3^2 - 1\right) \left(\xi_2^2 - 1\right) \Delta}, \tag{5.35}$$

$$b_{1,n}^{(+)} = \frac{-R_{(c,\xi_1)}^{(1)} \zeta_1 \zeta_2}{c^2 \left(\xi_3^2 - 1\right) \left(\xi_2^2 - 1\right) \Delta}, \tag{5.36}$$

$$a_{2,n}^{(-)} = \frac{i\zeta_2}{c\left(\xi_3^2-1\right)\Delta} \times \Big\langle \zeta_1 R_{(-c,\xi_2)}^{(3)} \left[C_{(c,\xi_2)}^{(1)} R_{(\xi_1)}^{(3)} - C_{(c,\xi_2)}^{(3)} R_{(\xi_1)}^{(1)} \right] + \zeta_2 C_{(-c,\xi_2)}^{(3)} \left[R_{(c,\xi_2)}^{(1)} R_{(c,\xi_1)}^{(3)} - R_{(c,\xi_2)}^{(3)} R_{(c,\xi_1)}^{(1)} \right] \Big\rangle, \tag{5.37}$$

$$b_{2,n}^{(-)} = \frac{-i\zeta_2}{c\left(\xi_3^2-1\right)\Delta} \times \Big\langle \zeta_1 R_{(-c,\xi_2)}^{(1)} \left[C_{(c,\xi_2)}^{(1)} R_{(c,\xi_1)}^{(3)} - C_{(c,\xi_2)}^{(3)} R_{(c,\xi_1)}^{(1)} \right] + + \zeta_2 C_{(-c,\xi_2)}^{(1)} \left[R_{(c,\xi_2)}^{(1)} R_{(c,\xi_1)}^{(3)} - R_{(c,\xi_2)}^{(3)} R_{(c,\xi_1)}^{(1)} \right] \Big\rangle. \tag{5.38}$$

We assume the notations:

$$\Delta_1 = \zeta_1 \left(C_{(c,\xi_2)}^{(1)} R_{(c,\xi_1)}^{(3)} - C_{(c,\xi_2)}^{(3)} R_{(c,\xi_1)}^{(1)} \right) \left(R_{(-c,\xi_3)}^{(1)} R_{(-c,\xi_2)}^{(3)} - R_{(-c,\xi_3)}^{(3)} R_{(-c,\xi_2)}^{(1)} \right) + \zeta_2 \left(C_{(c,\xi_2)}^{(1)} R_{(-c,\xi_3)}^{(3)} - C_{(-c,\xi_2)}^{(3)} R_{(-c,\xi_3)}^{(1)} \right) \left(R_{(c,\xi_1)}^{(1)} R_{(c,\xi_2)}^{(3)} - R_{(c,\xi_2)}^{(1)} R_{(c,\xi_1)}^{(3)} \right)$$

$$\Delta_2 = \zeta_1 \left(C_{(c,\xi_2)}^{(1)} R_{(c,\xi_1)}^{(3)} - C_{(c,\xi_2)}^{(3)} R_{(c,\xi_1)}^{(1)} \right) \left(C_{(-c,\xi_3)}^{(1)} R_{(-c,\xi_2)}^{(3)} - C_{(-c,\xi_3)}^{(3)} R_{(-c,\xi_2)}^{(1)} \right) + \zeta_2 \left(C_{(-c,\xi_2)}^{(1)} C_{(-c,\xi_3)}^{(3)} - C_{(-c,\xi_2)}^{(3)} C_{(-c,\xi_3)}^{(1)} \right) \left(R_{(c,\xi_1)}^{(1)} R_{(c,\xi_2)}^{(3)} - R_{(c,\xi_2)}^{(1)} R_{(c,\xi_1)}^{(3)} \right)$$

In which $\Delta = C_{(c,\xi_3)}^{(3)} \Delta_1 + R_{(c,\xi_3)}^{(3)} \zeta_2 \Delta_2$. The coefficient c_n^1 can be retrieved as:

$$c_n^1 = \frac{-\left[C_{(c,\xi_3)}^{(1)} \Delta_1 + R_{(c,\xi_3)}^{(1)} \zeta_2 \Delta_2 \right]}{\Delta}. \tag{5.39}$$

Case 2

By applying Cramer's rule, exact solutions for expansion coefficients c_n^2; $a_{2,n}^{(+)}$; $b_{2,n}^{(+)}$; $a_{1,n}^{(-)}$ and $b_{1,n}^{(-)}$ can be retrieved as follows

$$a_{1,n}^{(-)} = \frac{-R_{(-c,\xi_1)}^{(3)} \zeta_1 \zeta_2}{c^2\left(\xi_3^2-1\right)\left(\xi_2^2-1\right)\Delta}, \tag{5.40}$$

$$b_{1,n}^{(-)} = \frac{R_{(-c,\xi_1)}^{(1)} \zeta_1 \zeta_2}{c^2\left(\xi_3^2-1\right)\left(\xi_2^2-1\right)\Delta}. \tag{5.41}$$

$$a_{2,n}^{(+)} = \frac{-i\zeta_2}{c\left(\xi_3^2-1\right)\Delta} \times \Big\langle \zeta_2 C_{(c,\xi_2)}^{(3)} \left[R_{(-c,\xi_2)}^{(3)} R_{(-c,\xi_1)}^{(1)} - R_{(-c,\xi_2)}^{(1)} R_{(-c,\xi_1)}^{(3)} \right] - \zeta_1 R_{(c,\xi_2)}^{(3)} \left[C_{(-c,\xi_2)}^{(1)} R_{(-c,\xi_1)}^{(3)} - C_{(-c,\xi_2)}^{(3)} R_{(-c,\xi_1)}^{(1)} \right] \Big\rangle, \tag{5.42}$$

$$b_{2,n}^{(+)} = \frac{i\zeta_2}{c\left(\xi_3^2-1\right)\Delta} \times \Big\langle \zeta_2 C_{(c,\xi_2)}^{(1)} \left[R_{(-c,\xi_2)}^{(3)} R_{(-c,\xi_1)}^{(1)} - R_{(-c,\xi_2)}^{(1)} R_{(-c,\xi_1)}^{(3)}\right] \\ -\zeta_1 R_{(c,\xi_2)}^{(1)} \left[C_{(-c,\xi_2)}^{(1)} R_{(-c,\xi_1)}^{(3)} - C_{(-c,\xi_2)}^{(3)} R_{(-c,\xi_1)}^{(1)}\right] \Big\rangle . \tag{5.43}$$

We assume the notations:

$$\Delta_1 = \zeta_2 \left(C_{(c,\xi_2)}^{(1)} R_{(c,\xi_3)}^{(3)} - R_{(c,\xi_3)}^{(1)} C_{(c,\xi_2)}^{(3)}\right) \left(R_{(-c,\xi_1)}^{(1)} R_{(-c,\xi_2)}^{(3)} - R_{(-c,\xi_1)}^{(3)} R_{(-c,\xi_2)}^{(1)}\right) \\ + \zeta_1 \left(C_{(-c,\xi_2)}^{(1)} R_{(-c,\xi_1)}^{(3)} - C_{(-c,\xi_2)}^{(3)} R_{(-c,\xi_1)}^{(1)}\right) \left(R_{(c,\xi_3)}^{(1)} R_{(c,\xi_2)}^{(3)} - R_{(c,\xi_3)}^{(3)} R_{(c,\xi_2)}^{(1)}\right)$$

$$\Delta_2 = \zeta_2 \left(C_{(c,\xi_2)}^{(1)} C_{(c,\xi_3)}^{(3)} - C_{(c,\xi_3)}^{(1)} C_{(c,\xi_2)}^{(3)}\right) \left(R_{(-c,\xi_1)}^{(1)} R_{(-c,\xi_2)}^{(3)} - R_{(-c,\xi_2)}^{(1)} R_{(-c,\xi_1)}^{(3)}\right) \\ + \zeta_1 \left(C_{(c,\xi_3)}^{(1)} R_{(c,\xi_2)}^{(3)} - C_{(c,\xi_3)}^{(3)} R_{(c,\xi_2)}^{(1)}\right) \left(C_{(-c,\xi_2)}^{(1)} R_{(-c,\xi_1)}^{(3)} - C_{(-c,\xi_2)}^{(3)} R_{(-c,\xi_1)}^{(1)}\right)$$

In which $\Delta = C_{(c,\xi_3)}^{(3)} \Delta_1 - R_{(c,\xi_3)}^{(3)} \zeta_2 \Delta_2$. Coefficient c_n^2 can be retrieved as:

$$c_n^2 = \frac{-\left[C_{(c,\xi_3)}^{(1)} \Delta_1 + R_{(c,\xi_3)}^{(1)} \zeta_2 \Delta_2\right]}{\Delta}. \tag{5.44}$$

5.3.4 Numerical results

All the simulations are done with the parameters of: $d = 2$; $\lambda = 1$; $\xi_0 = 4.1$; $\xi_1 = 2$; $\xi_2 = 2.8$ and $\xi_3 = 3$.

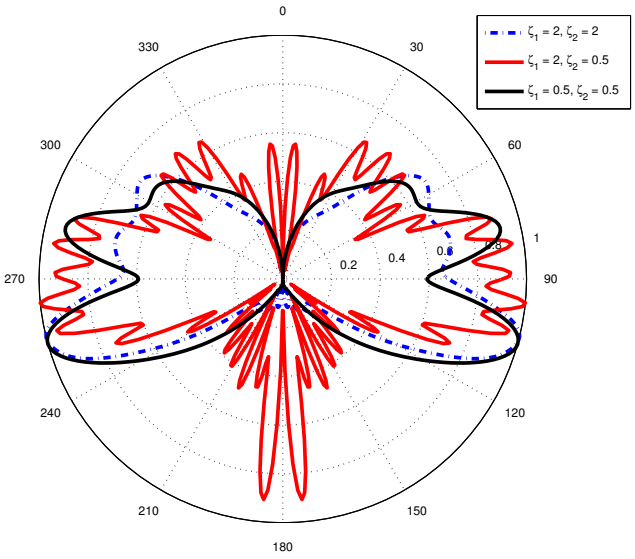

Figure 5.6: *The Scattered Electric Far Field of a magnetic Dipole when Layer 1 is Isorefractive and Layer 2 is Anti-Isorefractive with different* ζ_1, ζ_2

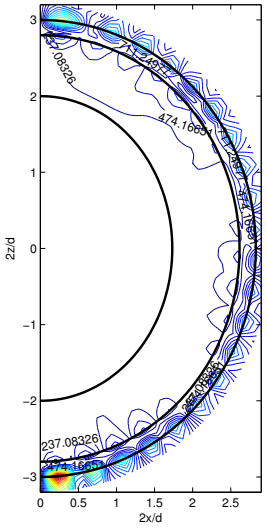

Figure 5.7: *Contour Plot of Electric Field of a magnetic Dipole in the case layer 1 is Isorefractive and layer 2 is Anti-Isorefractive with* $\zeta_1 = 2$, $\zeta_2 = 0.5$

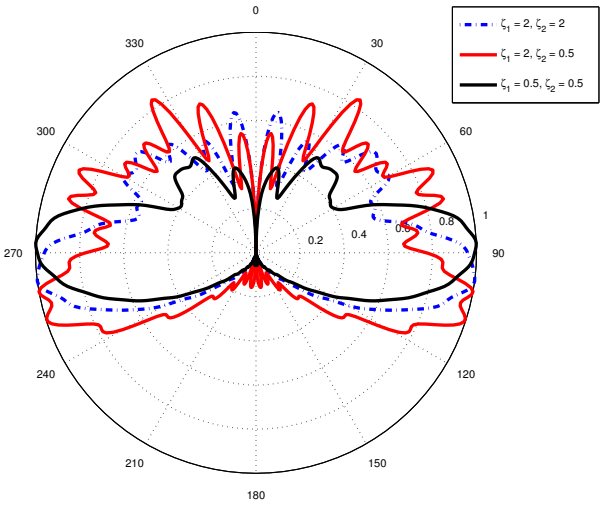

Figure 5.8: *The Scattered Electric Far Field of a magnetic Dipole when layer 1 is Anti-Isorefractive and layer 2 is Isorefractive with different* ζ_1, ζ_2

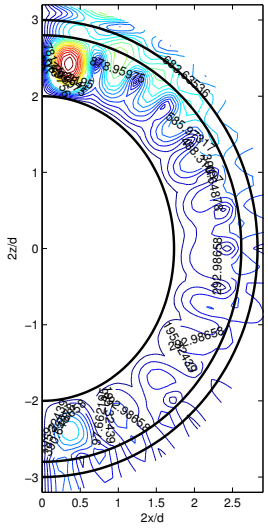

Figure 5.9: *Contour Plot of Electric Field of a magnetic Dipole in the case layer 1 is Anti-Isorefractive and layer 2 is Isorefractive with* $\zeta_1 = 0.5$, $\zeta_2 = 2$

5.4 Stochastic Optimization of the Far field

In this section, we come back to the conventional optimization scheme with all the implementing algorithms were presented in **chapter 1**. In **chapter 2**, a number of Electromagnetic drives are optimized by successfully establishing the link between global optimizer and full-wave analysis. Afterwards, **chapter 3** discusses how to save more optimizing time by introducing an equivalent model by the use of Artificial Neural Network. However, the key limitation of these techniques is the feasibility of model fully depends on full-wave analysis. The problems can only be solved if they can be modeled in commercial solvers. There are a large number of scattering problems that cannot be fully described by a simulator, like the issues presented in this chapter.

In this chapter, the issues on scattering of a magnetic dipole on Prolate Spheroids is totally covered, the exact solutions are already retrieved. It is obvious that we can construct a cost function representing this scattering problem with a specific constraint. The interesting point is radiated far field of a magnetic dipole with Prolate spheroids is very different from the case without those structures. In this context, in order to optimize the radiated far field of multiple dipoles, those interesting reflection of behaviors are utilized. The optimization scheme, as depicted in Figure 5.10, is the same as the scheme in Figure 2.1, however the representative cost function is built upon analytical model in this chapter.The details of numerical results are shown in the following.

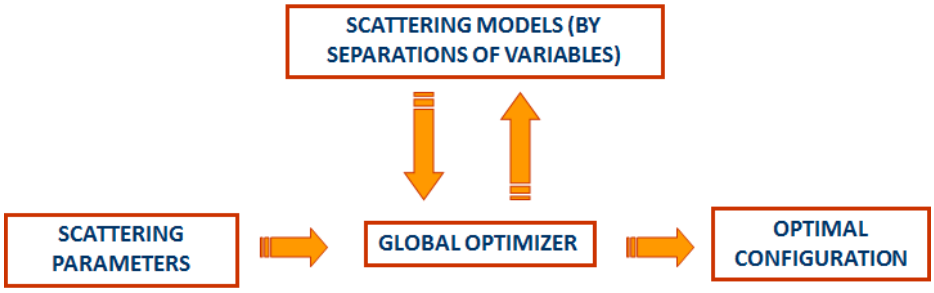

Figure 5.10: *Stochastic optimization scheme for scattering problem*

5.4.1 Problem description and analysis

A metallic prolate spheroid is coated by two confocal layers of penetrable medias, in this case, layer 1 is isorefractive or **DPS** and layer 2 is anti-isorefractive or **DNG**. An exact solution was already obtained by infinite series of prolate spheroidal wave functions when the primary source is a magnetic dipole.

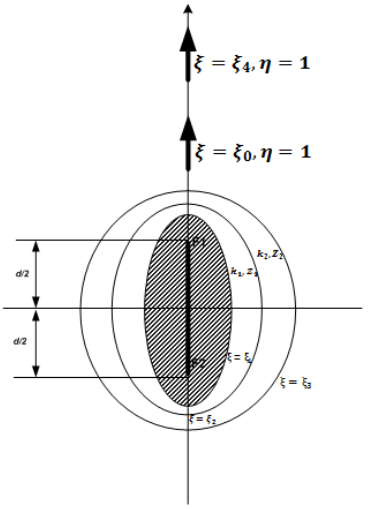

Figure 5.11: *The geometry of multi-dipole on Prolate spheroids when second located at* $\xi = \xi_4,\ \eta = 1$

As depicted in Figure 5.11, assuming Dipole 2 is located at $\xi = \xi_4, \eta = 1$, similarly to the equation 5.34, the Electric Scattered Far field can be retrieved as:

$$E_{\phi}^{s} \mid_{c\xi\to\infty} \approx \frac{e^{jk_o r}}{k_0 r} \frac{2k_0^2 Z_0}{\sqrt{\xi_4^2 - 1}} \sum_{n=1}^{\infty} \frac{(-i)^{n-1}}{\rho_{1,n} N_{1,n}} \gamma_n R_{1,n}^{(3)}(c, \xi_0)\, S_{1,n}(c, cos\theta)) \tag{5.45}$$

when $S_{1,n}(c, cos\theta)$ is the approximation of Angular Spheroidal Wave Functions for $S_{1,n}(c, \eta)$ in the far field region. In order to increase the degree of freedom in the solution domain, dipole 2 not only locates in the $+z$ plane but also in the $-z$ plane, as illustrated in Figure 5.12. As such, the term $S(c, \eta)$ in each serie will turn out to $S(c, -\eta)$ and the scattered Electric far field can be written as:

$$E_{\phi}^{s} \mid_{c\xi\to\infty} \approx \frac{e^{jk_o r}}{k_0 r} \frac{2k_0^2 Z_0}{\sqrt{\xi_4^2 - 1}} \sum_{n=1}^{\infty} \frac{(-i)^{n-1}}{\rho_{1,n} N_{1,n}} \gamma_n R_{1,n}^{(3)}(c, \xi_0)\, S_{1,n}(c, -cos\theta) \tag{5.46}$$

Calculation of the fields

According to Flammer [79] for Spheroidal Wave Functions , the Angular Spheroidal Wave Function can be calculated as:

$$S_{mn}(c, \eta) = (1 - \eta^2)^{\frac{m}{2}} \sum_{k=0}^{\infty} c_{2k}^{mn} (1 - \eta^2)^k \quad (n - m)\ even \tag{5.47}$$

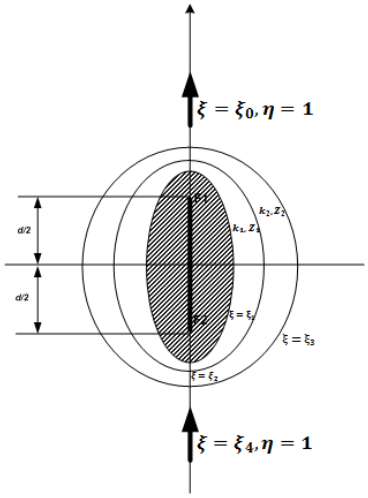

Figure 5.12: *The geometry of multi-dipole on Prolate spheroids when second dipole located at* $\xi = \xi_4,\ \eta = -1$

$$S_{mn}(c,\eta) = \eta(1-\eta^2)^{\frac{m}{2}} \sum_{k=0}^{\infty} c_{2k}^{mn}(1-\eta^2)^k \quad (n-m)\ odd \tag{5.48}$$

where c_{2k}^{mn} is defined in the [79]. According to two equations 5.47 and 5.48, $S_{mn}(c,-\eta)$ is only different from $S_{mn}(c,\eta)$ when $(n-m)$ is an odd number. A solution can be derived as:

$$S_{1,n}(c,-\eta) = (-1)^n \sum_{n=0}^{N} S_{1,n}(c,\eta) \tag{5.49}$$

where N is the number of terms in summations needed to compute the fields. Similarly

$$S_{1,n}(c,-cos(\theta)) = (-1)^{n-1} \sum_{n=1}^{N} S_{1,n}(c,cos(\theta) \tag{5.50}$$

In order to exhibit the accuracy equation 5.49, Figure 5.13 denotes the Electric field of two dipole with the same ξ but one with $\eta = 1$, the other with $\eta = -1$

5.4.2 Stochastic optimization and numerical results

Since a magnetic dipole produces only an Electric field E_ϕ so the total scattered far field of multiple dipoles put axially on $z - axis$ is the superposition of all the

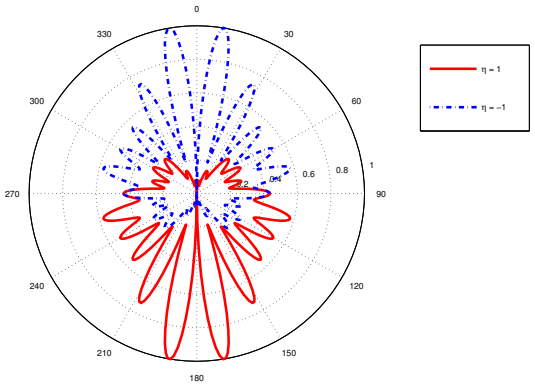

Figure 5.13: *Comparison of two dipoles with same ξ but different η*

components E_ϕ of each dipole, where M is the number of dipoles

$$E_{total,s} = \sum_{i=1}^{M} E_{i,s\phi}. \tag{5.51}$$

Given an angle α that the engineer want the beam of scattered far field to concentrate on, the merit of a representative cost function is the absolute value of scattered Electric field at given angle α.

$$cost\ value = \frac{\mid E_{s,total,\alpha} \mid}{\mid E_{max,total,\alpha} \mid}. \tag{5.52}$$

Nine parameters ($\xi_1,\ \xi_2,\ \xi_3,\ [\xi_0,\ \xi_4],\ dice,\ \zeta_1,\ \zeta_2,\ d$) of geometry are represented by a variable $X = [X_1,\ X_2,\ X_3,\ X_4,\ X_5,\ X_6,\ X_7,\ X_8,\ X_9,\ X_{10}]$ and they are compressed into a cost function with the aim of maximizing *cost value*. The variable $dice$ is a boolean, defining the position of dipole 2 either on $+z$ plane or $-z$ plane.

The purpose of optimization in this scheme is to maximize the scattered far field of two dipoles at the angle $\alpha = 60^o$. Global optimizer used in this research is Genetic Swarm Optimization (GSO), a hybridization technique of PSO and GA already presented in **Chapter 1**. With a population of 100 particles and after 5 iterations the best radiation pattern ever found is presented in Figure 5.14.

The details of geometry are shown in the Table 5.1, when both two dipoles stay in $+z$ plane ($\eta = 1$)

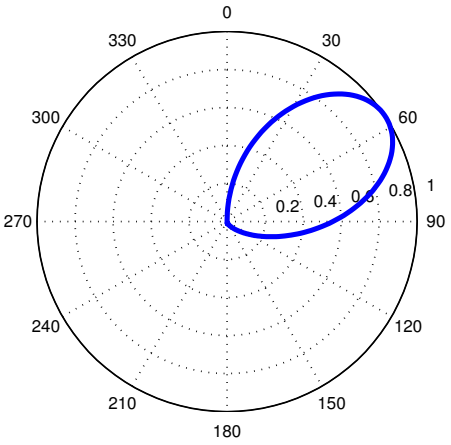

Figure 5.14: *Far field radiation pattern of best configuration in the half plane of θ*

Table 5.1: *Best configuration for the problem of 2 dipoles*

ξ_1	ξ_2	ξ_3	ξ_0	ξ_4	ζ_1	ζ_2	d
2.246	3.729	6.12234	7.253	8.463	0.906	0.99	1.04

CHAPTER 6

Dual-layer coating on Oblate Spheroids

In this chapter, the electromagnetic scattering problem of elementary source is carried out on oblate spheroidal system. Similar to the case of prolate, two coating layers are either DPS or DNG.

6.1 Geometry of the problem

A cross-section of the oblate spheroidal structure in a plane containing the axis z of symmetry is shown in Figure 6.1. The structure is centered at the origin of coordinates, with the $z = 0$ plane as the equatorial symmetry plane. The oblate spheroidal coordinates (η, ξ, ϕ) are related to the rectangular coordinate *(x, y, z)* by

$$\begin{cases} x &= \frac{d}{2}\sqrt{(\xi^2+1)\,(1-\eta^2)}\cos\phi \\ y &= \frac{d}{2}\sqrt{(\xi^2+1)\,(1-\eta^2)}\sin\phi \\ z &= \frac{d}{2}\xi\eta \end{cases} \tag{6.1}$$

where $-1 \leq \eta \leq 1, 1 \leq \xi \leq \infty$ and $0 \leq \phi \leq 2\pi$. The parameter d is the interfocal distance.
The dashed area in Figure 6.1 is the cross-section of a metallic oblate spheroid

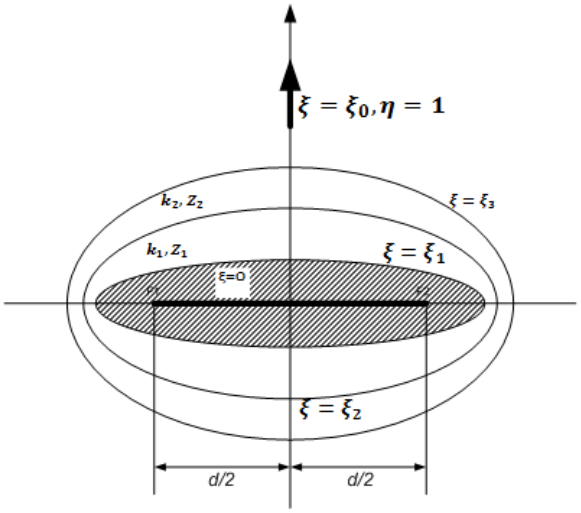

Figure 6.1: *Geometry of the problems*

with surface $\xi = \xi_1$, that becomes a thin wire of length d in the limit $\xi_1 = 1$. It is coated by two confocal layers of outer surface, at $\xi = \xi_2$ inner layer made of an isotropic and uniform material characterized by a real propagation constant k_1 and a real intrinsic impedance $Z_1 = {Y_1}^{-1}$. At $\xi = \xi_3$ outer layer made of an isotropic and uniform material characterized by a real propagation constant k_2 and a real intrinsic impedance $Z_2 = {Y_2}^{-1}$. The structure is surrounded by a medium characterized by a real positive propagation constant k_0 and a real positive intrinsic impedance $Z_0 = {Y_0}^{-1}$.

The primary source is an electric or magnetic Hertzian dipole located on the axis z of symmetry at $(\xi = \xi_0, \eta = 1)$ and axially oriented. Even though the analysis can be performed for a dipole source inside the coating layer, i.e for $\xi_1 < \xi_0 < \xi_2$, for simplicity the following derivations are carried out only for the case $\xi_0 > \xi_3$ of a source outside the scattering structure.

6.2 Electric dipole source

6.2.1 Interpretation of the fields

If the electric dipole at $(\xi = \xi_0, \eta = 1)$ is characterized by the Hertz vector

$$\mathbf{\Pi_e}^{\mathbf{i}} = \hat{z}\frac{e^{jkr}}{kr} \tag{6.2}$$

where R is the distance from the dipole to the observation point, then the electric field $\underline{E}$ and the magnetic field $\underline{H}$ are everywhere of the type

$$\begin{aligned}\mathbf{E} &= E_\xi(\xi,\eta)\,\hat{\xi} + E_\eta(\xi,\eta)\,\hat{\eta}, \quad E_\phi = 0\\ \mathbf{H} &= H_\phi(\xi,\eta)\,\hat{\phi}, \quad H_\xi = H_\eta = 0\end{aligned} \tag{6.3}$$

In particular the incident field component ${H_\phi}^i$ corresponding to the source in (6.2) may be written as infinite series of oblate spheroidal wave functions [84]

$$H_\phi^i = \frac{2k^2 Y_0}{\sqrt{\xi_0^2+1}} \sum_{n=1}^{\infty} \frac{(-i)^n}{\widetilde{\rho}_{1,n}\widetilde{N}_{1,n}} R_{1,n}^{(1)}(-ic, i\xi_<)\, R_{1,n}^{(3)}(-ic, i\xi_>)\, S_{1,n}(-ic,\eta),$$
$$\xi_{\lessgtr} = \begin{matrix} min \\ max \end{matrix} (\xi, \xi_0) \tag{6.4}$$

where the dimensionless parameter

$$c = \frac{kd}{2} \tag{6.5}$$

and Flammer's notation has been used [79]. The coordinates $\xi_<$ ($\xi_>$) are the smaller (larger) between ξ and ξ_0; Notations $\rho_{1,n}$ and $\widetilde{N}_{1,n}$ are the normalization constants for the radial and angular functions, respectively. In order to impose the boundary condition across the interface $\xi = \xi_2$, it is necessary to consider also the component ${E_\eta}^i$, which is obtained from ${H_\phi}^i$ as

$$\begin{aligned} E_\eta^i &= \frac{iZ_0}{c}\sqrt{\frac{\xi^2+1}{\xi^2+\eta^2}}\left(\frac{\partial}{\partial\xi} + \frac{\xi}{\xi^2+1}\right)\left(H_\phi^i\right)\\ &= \frac{2ik^2}{c\sqrt{\xi_0^2+1}}\sqrt{\frac{\xi^2+1}{\xi^2+\eta^2}}\sum_{n=1}^{\infty}\frac{(-1)^n}{\widetilde{\rho}_{1,n}\widetilde{N}_{1,n}} S_{1,n}(-ic,\eta)\times\\ &\begin{cases} R_{1,n}^{(3)}(-ic, i\xi_0)\, A_n^{(1)}(-ic, i\xi), & \xi < \xi_0\\ R_{1,n}^{(1)}(-ic, i\xi_0)\, A_n^{(3)}(-ic, i\xi), & \xi > \xi_0 \end{cases}\end{aligned} \tag{6.6}$$

where

$$A^{(h)}(\mp ic,\xi) = R_{1,n}^{(h)\prime}(\mp ic, i\xi) + \frac{\xi}{\xi^2-1} R_{1,n}^{(h)}(\mp ic, i\xi), \quad (h = 1,3)$$

The prime means derivative with respect to ξ.

If the expressions akin to (6.4) and (6.6) are written for the field components inside two coating layers, they would contain the parameters:

$$c_{1,2} = \frac{k_{1,2}d}{2} \tag{6.7}$$

instead of c, in both the radial functions $R_{1,n}^{(1)}$, $R_{1,n}^{(3)}$ and the angular functions $S_{1,n}$. The explicit, analytical determination is possible only if the angular function $S_{1,n}$ is the same on both sides of the interface $\xi = \xi_2$; since $S_{1,n}$ is an even function of parameter c (this is not true for the radial function!). This occurs in two cases: either $c_{1,2} = c$ (i.e. $k_1 = k_0$), meaning that the coating layers and the surrounding medium have the same index of refraction (isorefractive layer); or $c_{1,2} = -c$ (i.e. $k_{1,2} = -k_0$), meaning that the coating layer is a DNG metamaterial whose index of refraction is the negative of the index of refraction of the surrounding medium (anti-isorefractive layer).

In all the following formulas, the upper sign applies to an isorefractive coating layer, and the lower sign to an anti-isorefractive coating layer. Since the electric dipole is located outside of two lossless dielectric layers, so $\xi_0 > \xi_3$ and $l = 1$ for inside layer ($\xi_1 \leq \xi \leq \xi_2$) and $l = 2$ for outside layer ($\xi_2 \leq \xi \leq \xi_3$): Magnetic and Electric fields inside two coating layers are expressed by following formulas, respectively:

$$H_{l,\phi}^{\pm} = \frac{2k^2 Y_l}{\sqrt{\xi_0^2+1}} \sum_{n=1}^{\infty} \frac{(-i)^n}{\widetilde{\rho}_{1,n}\widetilde{N}_{1,n}} R_{1,n}^{(3)}(-ic, i\xi_0)\, S_{1,n}(-ic, \eta) \times \\ \times \left[a_{l,n}^{\pm} R_{1,n}^{(1)}(\mp ic, i\xi) + b_{l,n}^{\pm} R_{1,n}^{(3)}(\mp ic, i\xi) \right] \tag{6.8}$$

And Electric field:

$$E_{l,\eta}^{\pm} = \frac{\pm 2ik^2}{c\sqrt{\xi_0^2+1}} \sqrt{\frac{\xi^2+1}{\xi^2+\eta^2}} \sum_{n=1}^{\infty} \frac{(-i)^n}{\widetilde{\rho}_{1,n}\widetilde{N}_{1,n}} R_{1,n}^{(3)}(-ic, i\xi_0)\, S_{1,n}(-ic, \eta) \times \\ \times \left[a_{l,n}^{\pm} A_n^{(1)}(\mp ic, i\xi) + b_{l,n}^{\pm} A_n^{(3)}(\mp ic, i\xi) \right] . \tag{6.9}$$

The scattered fields outside the structure ($\xi_3 \leq \xi$) are expressed as:
$m = 1$ for the first case (outside layer is anti-isorefractive);
$m = 2$ for the second case (outside layer is isorefractive)

Scattered Magnetic Field:

$$H_{\phi}^{s,m} = \frac{2k^2 Y}{\sqrt{\xi_0^2+1}} \sum_{n=1}^{\infty} \frac{(-i)^n}{\widetilde{\rho}_{1,n}\widetilde{N}_{1,n}} {c_n}^m R_{1,n}^{(3)}(-ic, i\xi_0)\, R_{1,n}^{(3)}(-ic, \xi)\, S_{1,n}(c, \eta) , \tag{6.10}$$

And scattered Electric Field:

$$E_{\phi}^{s,m} = \frac{2ik^2}{c\sqrt{\xi_0^2+1}}\sqrt{\frac{\xi^2+1}{\xi^2+\eta^2}}\sum_{n=1}^{\infty}\frac{(-i)^n}{\widetilde{\rho}_{1,n}\widetilde{N}_{1,n}}{c_n}^m R_{1,n}^{(3)}\left(-ic, i\xi_0\right)\times \\ \times S_{1,n}\left(-ic,\eta\right)\times A_n^{(3)}\left(-ic, i\xi\right). \quad (6.11)$$

With the reference to spherical cooridnates (r,θ,ϕ) with the origin at the center of the structure, the scatterd far field is:

$$H_{\phi}^{s}\mid_{c\xi\to\infty} \sim \frac{e^{jkr}}{kr}\frac{2k^2Y_0}{\sqrt{\xi_0^2+1}}\sum_{n=1}^{\infty}\frac{(-i)^n}{\widetilde{\rho}_{1,n}\widetilde{N}_{1,n}}{c_n}^m R_{1,n}^{(3)}\left(-ic, i\xi_0\right)S_{1,n}\left(-ic, cos\theta\right). \quad (6.12)$$

Properties of Oblate Spheroidal functions

Angular function $S_{1,n}$ is an even function of c :
$S_{1,n}\left(-ic,\eta\right) = S_{1,n}\left(+ic,\eta\right)$.
According to Flammer's notes [79], properties of radial functions can be written as:

$$R_{m,n}^{(3,4)}\left(-ic, i\xi\right) = {R_{m,n}}^{(1)}\left(-ic, i\xi\right) \pm i{R_{m,n}}^{(2)}\left(-ic, i\xi\right)$$
$$R_{1,n}^{(1)}\left(-ic, i\xi\right)R_{1,n}^{(3)\prime}\left(-ic, i\xi\right) - R_{1,n}^{(1)\prime}\left(-ic, i\xi\right)R_{1,n}^{(3)}\left(-ic, i\xi\right) = \frac{1}{c\left(\xi^2+1\right)}.$$

Therefore:

$$A_{(-ic,i\xi)}^{(1)}R_{(-ic,i\xi)}^{(3)} - A_{(-ic,i\xi)}^{(3)}R_{(-ic,i\xi)}^{(1)} = \frac{-i}{c\left(\xi^2+1\right)}$$
$$A_{(+ic,i\xi)}^{(1)}R_{(+ic,i\xi)}^{(3)} - A_{(+ic,i\xi)}^{(3)}R_{(+ic,i\xi)}^{(1)} = \frac{i}{c\left(\xi^2+1\right)}.$$

6.2.2 Applying Boundary Conditions

Case 1

Description: Outer layer is anti-isorefractive; inner layer is isorefractive.
Applying boundary conditions for the tangential components of Electric field and Magnetic field at $\xi = \xi_1$, $\xi = \xi_2$ and $\xi = \xi_3$, we have five linear equations as follows:
$E_{1\eta}^{(+)}\mid_{\xi=\xi_1} = 0$

$E_{1\eta}^{(+)}\mid_{\xi=\xi_2} = E_{2\eta}^{(-)}\mid_{\xi=\xi_2}; H_{1\phi}^{(+)}\mid_{\xi=\xi_2} = H_{2\phi}^{(-)}\mid_{\xi=\xi_2};$

$E_{2\eta}^{(-)}\mid_{\xi=\xi_3} = \left(E_{\eta}^{s,1} + E_{\eta}^{i}\right)\mid_{\xi=\xi_3};$
$H_{2\phi}^{(-)}\mid_{\xi=\xi_3} = \left(H_{\phi}^{s,1} + H_{\phi}^{i}\right)\mid_{\xi=\xi_3}.$

Expansion coefficients: γ_n^1; $\alpha_{2,n}^{(-)}$; $\beta_{2,n}^{(-)}$; $\alpha_{1,n}^{(+)}$ and $\beta_{1,n}^{(+)}$ will be determined by solving this system of linear equations.

Case 2

Description: Outer layer is isorefractive; inner layer is anti-isorefractive
Applying boundary conditions for the tangential components of Electric field and Magnetic field at $\xi = \xi_1$, $\xi = \xi_2$ and $\xi = \xi_3$, we have five linear equations as follows:
$E_{1\eta}^{(-)}\mid_{\xi=\xi_1} = 0$

$E_{1\eta}^{(-)}\mid_{\xi=\xi_2} = E_{2\eta}^{(+)}\mid_{\xi=\xi_2}; H_{1\phi}^{(-)}\mid_{\xi=\xi_2} = H_{2\phi}^{(+)}\mid_{\xi=\xi_2};$

$E_{2\eta}^{(+)}\mid_{\xi=\xi_3} = \left(E_{\eta}^{s,2} + E_{\eta}^{i}\right)\mid_{\xi=\xi_3};$
$H_{2\phi}^{(+)}\mid_{\xi=\xi_3} = \left(H_{\phi}^{s,2} + H_{\phi}^{i}\right)\mid_{\xi=\xi_3}.$

Expansion coefficients: γ_n^2; $\alpha_{2,n}^{(+)}$; $\beta_{2,n}^{(+)}$; $\alpha_{1,n}^{(-)}$ and $\beta_{1,n}^{(-)}$ will be determined by solving this system of linear equations.

6.2.3 Exact solutions

Case 1

By applying Cramer's rule, exact solutions for expansion coefficients α_1; β_1; α_2; β_2 and γ_n^1 can be retrieved as follows:

$$\alpha_1^{(+)} = \frac{-A_{(-ic,i\xi_1)}^{(3)}\zeta_2}{c^2\left(\xi_3^2+1\right)\left(\xi_2^2+1\right)\Delta}, \tag{6.13}$$

$$\beta_1^{(+)} = \frac{A_{(-ic,i\xi_1)}^{(1)}\zeta_2}{c^2\left(\xi_3^2+1\right)\left(\xi_2^2+1\right)\Delta}, \tag{6.14}$$

$$\begin{aligned}\alpha_2^{(-)} = \frac{i}{c\left(\xi_3^2+1\right)\Delta} \times \Big\langle & \zeta_2 R_{(+ic,i\xi_2)}^{(3)}\left[A_{(-ic,i\xi_1)}^{(1)}A_{(-ic,i\xi_2)}^{(3)} - A_{(-ic,i\xi_2)}^{(1)}A_{(-ic,i\xi_1)}^{(3)}\right] \\ & +\zeta_1 A_{(+ic,i\xi_2)}^{(3)}\left[A_{(-ic,i\xi_1)}^{(1)}R_{(-ic,i\xi_2)}^{(3)} - A_{(-ic,i\xi_1)}^{(3)}R_{(-ic,i\xi_2)}^{(1)}\right]\Big\rangle,\end{aligned} \tag{6.15}$$

$$\beta_2^{(-)} = \frac{-i}{c\left(\xi_3^2+1\right)\Delta} \times \left\langle \zeta_2 R^{(1)}_{(+ic,i\xi_2)} \left[A^{(1)}_{(-ic,i\xi_1)} A^{(3)}_{(-ic,i\xi_2)} - A^{(1)}_{(-ic,i\xi_2)} A^{(3)}_{(-ic,i\xi_1)} \right] + \zeta_1 A^{(1)}_{(+ic,i\xi_2)} \left[A^{(1)}_{(-ic,i\xi_1)} R^{(3)}_{(-ic,i\xi_2)} - A^{(3)}_{(-ic,i\xi_1)} R^{(1)}_{(-ic,i\xi_2)} \right] \right\rangle. \tag{6.16}$$

We assume the notations:

$$\Delta_1 = \zeta_2 \left(A^{(1)}_{(-ic,i\xi_1)} A^{(3)}_{(-ic,i\xi_2)} - A^{(1)}_{(-ic,i\xi_2)} A^{(3)}_{(-ic,i\xi_1)} \right) \left(A^{(1)}_{(+ic,i\xi_3)} R^{(3)}_{(+ic,i\xi_2)} - A^{(3)}_{(+ic,i\xi_3)} R^{(1)}_{(+ic,i\xi_2)} \right) - \zeta_1 \left(A^{(1)}_{(-ic,i\xi_1)} R^{(3)}_{(-ic,i\xi_2)} - A^{(3)}_{(-ic,i\xi_1)} R^{(1)}_{(-ic,i\xi_2)} \right) \left(A^{(1)}_{(+ic,i\xi_2)} A^{(3)}_{(+ic,i\xi_3)} - A^{(1)}_{(+ic,i\xi_3)} A^{(3)}_{(+ic,i\xi_2)} \right)$$

$$\Delta_2 = \zeta_2 \left(A^{(1)}_{(-ic,i\xi_1)} A^{(3)}_{(-ic,i\xi_2)} - A^{(1)}_{(-ic,i\xi_2)} A^{(3)}_{(-ic,i\xi_1)} \right) \left(R^{(1)}_{(+ic,i\xi_3)} R^{(3)}_{(+ic,i\xi_2)} - R^{(1)}_{(+ic,i\xi_2)} R^{(3)}_{(+ic,i\xi_3)} \right) - \zeta_1 \left(A^{(1)}_{(+ic,i\xi_2)} R^{(3)}_{(+ic,i\xi_3)} - A^{(3)}_{(+ic,i\xi_2)} R^{(1)}_{(+ic,i\xi_3)} \right) \left(A^{(1)}_{(-ic,i\xi_1)} R^{(3)}_{(-ic,i\xi_2)} - A^{(3)}_{(-ic,i\xi_1)} R^{(1)}_{(-ic,i\xi_2)} \right)$$

in which $\Delta = R^{(3)}_{(-ic,i\xi_3)} \Delta_1 + A^{(3)}_{(-ic,i\xi_3)} \zeta_2 \Delta_2$. Coefficient γ^1 can be retrieved as:

$$\gamma^1 = \frac{-\left[R^{(1)}_{(-ic,i\xi_3)} \Delta_1 + A^{(1)}_{(-ic,i\xi_3)} \zeta_2 \Delta_2 \right]}{\Delta}. \tag{6.17}$$

Case 2

By applying Cramer's rule, exact solutions for expansion coefficients α_1; β_1; α_2; β_2, γ^2 can be retrieved as follows:

$$\alpha_1^{(-)} = \frac{-A^{(3)}_{(+ic,i\xi_1)} \zeta_2}{c^2\left(\xi_3^2+1\right)\left(\xi_2^2+1\right)\Delta}, \tag{6.18}$$

$$\beta_1^{(-)} = \frac{A^{(1)}_{(+ic,i\xi_1)} \zeta_2}{c^2\left(\xi_3^2+1\right)\left(\xi_2^2+1\right)\Delta}, \tag{6.19}$$

$$\alpha_2^{(+)} = \frac{i}{c\left(\xi_3^2+1\right)\Delta} \times \left\langle \zeta_2 R^{(3)}_{(-ic,i\xi_2)} \left[A^{(1)}_{(+ic,i\xi_1)} A^{(3)}_{(+ic,i\xi_2)} - A^{(1)}_{(+ic,i\xi_2)} A^{(3)}_{(+ic,i\xi_1)} \right] + \zeta_1 A^{(3)}_{(-ic,i\xi_2)} \left[A^{(1)}_{(+ic,i\xi_1)} R^{(3)}_{(+ic,i\xi_2)} - A^{(3)}_{(+ic,i\xi_1)} R^{(1)}_{(+ic,i\xi_2)} \right] \right\rangle, \tag{6.20}$$

$$\beta_2^{(+)} = \frac{i}{c\left(\xi_3^2+1\right)\Delta} \times \left\langle \zeta_2 R^{(1)}_{(-ic,i\xi_2)} \left[A^{(1)}_{(+ic,i\xi_1)} A^{(3)}_{(+ic,i\xi_2)} - A^{(1)}_{(+ic,i\xi_2)} A^{(3)}_{(+ic,i\xi_1)} \right] + \zeta_1 A^{(1)}_{(-ic,i\xi_2)} \left[A^{(1)}_{(+ic,i\xi_1)} R^{(3)}_{(+ic,i\xi_2)} - A^{(3)}_{(+ic,i\xi_1)} R^{(1)}_{(+ic,i\xi_2)} \right] \right\rangle. \tag{6.21}$$

We assume the notations:

$$\Delta_1 = \zeta_1 \left(A^{(1)}_{(-ic,i\xi_2)} A^{(3)}_{(-ic,i\xi_3)} - A^{(1)}_{(-ic,i\xi_3)} A^{(3)}_{(-ic,i\xi_2)} \right) \left(A^{(1)}_{(+ic,i\xi_1)} R^{(3)}_{(+ic,i\xi_2)} - A^{(3)}_{(+ic,i\xi_1)} R^{(1)}_{(+ic,i\xi_2)} \right) - \zeta_2 \left(A^{(1)}_{(-ic,i\xi_3)} R^{(3)}_{(-ic,i\xi_2)} - A^{(3)}_{(-ic,i\xi_3)} R^{(1)}_{(-ic,i\xi_2)} \right) \left(A^{(1)}_{(+ic,i\xi_1)} A^{(3)}_{(+ic,i\xi_2)} - A^{(1)}_{(+ic,i\xi_2)} A^{(3)}_{(+ic,i\xi_1)} \right)$$

$\Delta_2 = \zeta_2 \left(A^{(1)}_{(+ic,i\xi_1)} A^{(3)}_{(+ic,i\xi_2)} - A^{(1)}_{(+ic,i\xi_2)} A^{(3)}_{(+ic,i\xi_1)} \right) \left(R^{(1)}_{(-ic,i\xi_3)} R^{(3)}_{(-ic,i\xi_2)} - R^{(1)}_{(-ic,i\xi_2)} R^{(3)}_{(-ic,i\xi_3)} \right)$
$- \zeta_1 \left(A^{(1)}_{(-ic,i\xi_2)} R^{(3)}_{(-ic,i\xi_3)} - A^{(3)}_{(-ic,i\xi_2)} R^{(1)}_{(-ic,i\xi_3)} \right) \left(A^{(1)}_{(+ic,i\xi_1)} R^{(3)}_{(+ic,i\xi_2)} - A^{(3)}_{(+ic,i\xi_1)} R^{(1)}_{(+ic,i\xi_2)} \right)$
in which $\Delta = R^{(3)}_{(-ic,i\xi_3)} \Delta_1 + A^{(3)}_{(-ic,i\xi_3)} \zeta_2 \Delta_2$. Coefficient γ^2 can be retrieved as:

$$\gamma^2 = \frac{- \left[R^{(1)}_{(-ic,i\xi_3)} \Delta_1 + A^{(1)}_{(-ic,i\xi_3)} \zeta_2 \Delta_2 \right]}{\Delta} \tag{6.22}$$

6.2.4 Numerical results

All the simulations are done with the parameters of: $d = 2$; $\lambda = 1$; $\xi_0 = 1.5$; $\xi_1 = 0.25$; $\xi_2 = 0.5$ and $\xi_3 = 0.6$.

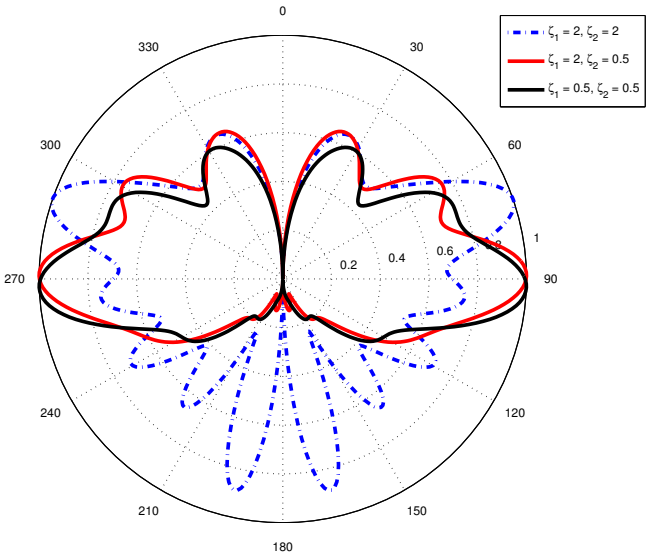

Figure 6.2: *The Scattered Magnetic Far Field of an Electric Dipole when Layer 1 is Isorefractive and Layer 2 is Anti-Isorefractive with different* ζ_1, ζ_2

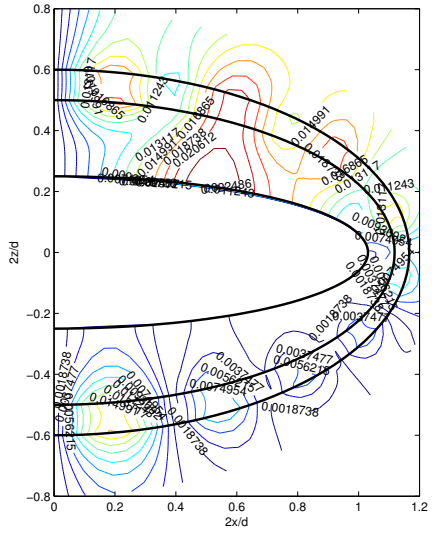

Figure 6.3: *Contour Plot of Magnetic Field of an Electric Dipole in the case layer 1 is Isorefractive and layer 2 is Anti-Isorefractive with* $\zeta_1 = 2$, $\zeta_2 = 0.5$

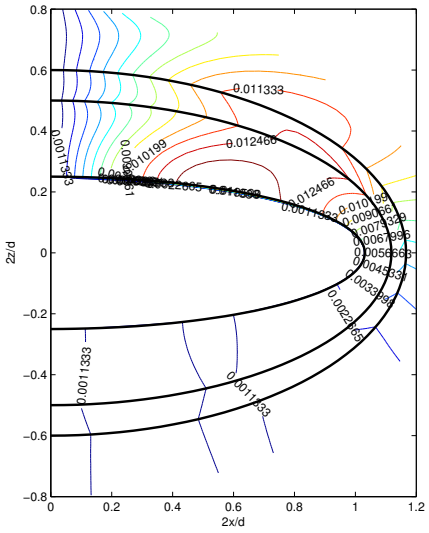

Figure 6.4: *Contour Plot of Magnetic Field of an Electric Dipole in the case layer 1 is Isorefractive and layer 2 is Anti-Isorefractive with* $\zeta_1 = 2$, $\zeta_2 = 2$

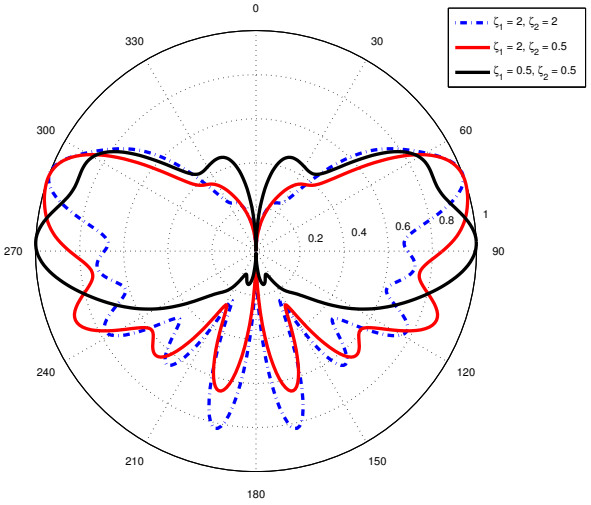

Figure 6.5: *The Scattered Magnetic Far Field of an Electric Dipole when layer 1 is Anti-Isorefractive and layer 2 is Isorefractive with different* ζ_1, ζ_2

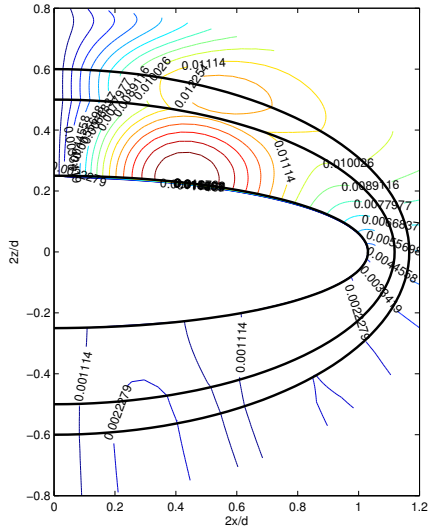

Figure 6.6: *Contour Plot of Magnetic Field of an Electric Dipole in the case layer 1 is Anti-Isorefractive and layer 2 is Isorefractive with* $\zeta_1 = 2$, $\zeta_2 = 0.5$

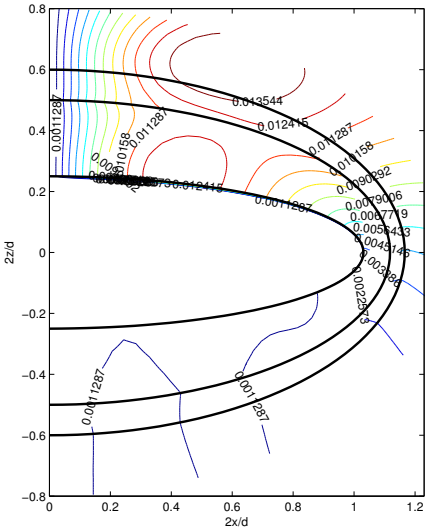

Figure 6.7: *Contour Plot of Magnetic Field of an Electric Dipole in the case layer 1 is Anti-Isorefractive and layer 2 is Isorefractive with* $\zeta_1 = 2$, $\zeta_2 = 2$

6.3 Magnetic dipole source

6.3.1 Interpretation of the fields

If the magnetic dipole at $(\xi = \xi_0, \eta = 1)$ is characterized by the Hertz vector

$$\mathbf{\Pi_m}^{\mathbf{i}} = \hat{z}\frac{e^{jkr}}{kr} \tag{6.23}$$

generates electric and magnetic fields that are everywhere of the type

$$\begin{aligned} \mathbf{E} &= E_\phi(\xi,\eta)\,\hat{\phi}, & E_\xi = E_\eta = 0 \\ \mathbf{H} &= H_\xi(\xi,\eta)\,\hat{\xi} + H_\eta(\xi,\eta)\,\hat{\eta}, & H_\phi = 0 \end{aligned} \tag{6.24}$$

It should be noted that the fields cannot be simply obtained by duality from electric dipole case, because duality would require that the core spheroid be a perfect magnetic conductor. The incident field components ${E_\phi}^i$ and ${H_\eta}^i$ may be written as the infinite series:

$$E_\phi^i = \frac{-2k^2 Z_0}{\sqrt{\xi_0^2+1}}\sum_{n=1}^{\infty}\frac{(-i)^n}{\widetilde{\rho}_{1,n}\widetilde{N}_{1,n}} R_{1,n}^{(1)}(-ic, i\xi_<)\, R_{1,n}^{(3)}(-ic, i\xi_>)\, S_{1,n}(-ic,\eta)$$
$$\xi_{\lessgtr} = \begin{matrix} min \\ max \end{matrix}(\xi, \xi_0) \tag{6.25}$$

$$H_\eta^i = \frac{2ik^2}{c\sqrt{\xi_0^2+1}}\sqrt{\frac{\xi^2+1}{\xi^2+\eta^2}}\sum_{n=1}^{\infty}\frac{(-i)^n}{\widetilde{\rho}_{1,n}\widetilde{N}_{1,n}} S_{1,n}(-ic,\eta)\times$$
$$\begin{cases} R_{1,n}^{(3)}(-ic, i\xi_0)\, A_n^{(1)}(-ic, i\xi), & \xi < \xi_0 \\ R_{1,n}^{(1)}(-ic, i\xi_0)\, A_n^{(3)}(-ic, i\xi), & \xi > \xi_0 \end{cases}, \tag{6.26}$$

In all the following formulas, the upper sign applies to an isorefractive coating layer, and the lower sign to an anti-isorefractive coating layer. Since the electric dipole is located outside of two lossless dielectric layers, so $\xi_0 > \xi_3$ and $l = 1$ for inside layer $(\xi_1 \le \xi \le \xi_2)$ and $l = 2$ for outside layer $(\xi_2 \le \xi \le \xi_3)$: Magnetic and Electric fields inside two coating layers are expressed by following formulas. As for Electric Field:

$$E_{l,\phi}^{\pm} = \frac{-2k^2 Z_l}{\sqrt{\xi_0^2+1}}\sum_{n=1}^{\infty}\frac{(-i)^n}{\widetilde{\rho}_{1,n}\widetilde{N}_{1,n}} R_{1,n}^{(3)}(-ic, i\xi_0)\, S_{1,n}(-ic,\eta)\times$$
$$\times\left[a_{l,n}^{\pm} R_{1,n}^{(1)}(\mp ic, i\xi) + b_{l,n}^{\pm} R_{1,n}^{(3)}(\mp ic, i\xi)\right], \tag{6.27}$$

And Magnetic field:

$$H_{l,\eta}^{\pm} = \frac{\pm 2ik_0^2}{c\sqrt{\xi_0^2+1}}\sqrt{\frac{\xi^2+1}{\xi^2+\eta^2}}\sum_{n=1}^{\infty}\frac{(-i)^n}{\widetilde{\rho}_{1,n}\widetilde{N}_{1,n}}R_{1,n}^{(3)}\left(-ic,i\xi_0\right)S_{1,n}\left(-ic,\eta\right)\times \\ \left[a_{l,n}^{\pm}A_n^{(1)}\left(\mp ic,i\xi\right)+b_{l,n}^{\pm}A_n^{(3)}\left(\mp ic,i\xi\right)\right]\ . \quad (6.28)$$

The scattered fields outside the structure $(\xi_3 \leq \xi)$ are expressed as:
$m = 1$ for the first case (outside layer is anti-isorefractive);
$m = 2$ for the second case (outside layer is Isorefractive)
As for Scattered Electric Field:

$$E_{\phi}^{s,m} = \frac{-2k^2Z_0}{\sqrt{\xi_0^2+1}}\sum_{n=1}^{\infty}\frac{(-i)^n}{\widetilde{\rho}_{1,n}\widetilde{N}_{1,n}}{c_n}^m R_{1,n}^{(3)}\left(-ic,i\xi_0\right)R_{1,n}^{(3)}\left(-ic,i\xi\right)S_{1,n}\left(-ic,\eta\right), \quad (6.29)$$

And Scattered Magnetic field:

$$H_{\eta}^{s,m} = \frac{2ik^2}{c\sqrt{\xi_0^2+1}}\sqrt{\frac{\xi^2+1}{\xi^2+\eta^2}}\sum_{n=1}^{\infty}\frac{(-i)^n}{\widetilde{\rho}_{1,n}\widetilde{N}_{1,n}}{c_n}^m R_{1,n}^{(3)}\left(-ic,i\xi_0\right)\times \\ \times S_{1,n}\left(-ic,\eta\right)A_n^{(3)}\left(-ic,i\xi\right). \quad (6.30)$$

With the reference to spherical cooridnates (r,θ,ϕ) with the origin at the center of the structure, the scatterd far field is:

$$E_{\phi}^{s}\mid_{c\xi\to\infty} \mid \frac{e^{jkr}}{kr}\frac{2k^2Z_0}{\sqrt{\xi_0^2+1}}\sum_{n=1}^{\infty}\frac{(-i)^n}{\widetilde{\rho}_{1,n}\widetilde{N}_{1,n}}{\gamma_n}^m R_{1,n}^{(3)}\left(-ic,i\xi_0\right)S_{1,n}\left(-ic,cos\theta\right). \quad (6.31)$$

6.3.2 Applying Boundary Conditions

Case 1

Description: Outer layer is anti-isorefractive; inner layer is Isorefractive
Applying boundary conditions for the tangential components of Electric field and Magnetic field at $\xi = \xi_1$; $\xi = \xi_2$ and $\xi = \xi_3$, we have five linear equations as follows:

$E_{1\phi}^{(+)}\mid_{\xi=\xi_1} = 0$

$E_{1\phi}^{(+)}\mid_{\xi=\xi_2} = E_{2\phi}^{(-)}\mid_{\xi=\xi_2}$; $H_{1\eta}^{(+)}\mid_{\xi=\xi_2} = H_{2\eta}^{(-)}\mid_{\xi=\xi_2}$;

$E_{2\phi}^{(-)}\mid_{\xi=\xi_3} = \left(E_{\phi}^{s,1}+E_{\phi}^{i}\right)\mid_{\xi=\xi_3}$;

$H_{2\eta}^{(-)} \mid_{\xi=\xi_3} = \left(H_\eta^{s,1} + H_\eta^i\right) \mid_{\xi=\xi_3}$;

Expansion coefficients: γ_n^1; $\alpha_{2,n}^{(-)}$; $\beta_{2,n}^{(-)}$; $\alpha_{1,n}^{(+)}$ and $\beta_{1,n}^{(+)}$ will be determined by solving this system of linear equations.

Case 2

Description: Outer layer is Isorefractive; inner layer is Anti-isorefractive
Applying boundary conditions for the tangential components of Electric field and Magnetic field at $\xi = \xi_1$; $\xi = \xi_2$ and $\xi = \xi_3$, we have five linear equations as follows:
$E_{1\phi}^{(-)} \mid_{\xi=\xi_1} = 0$

$E_{1\phi}^{(-)} \mid_{\xi=\xi_2} = E_{2\phi}^{(+)} \mid_{\xi=\xi_2}$; $H_{1\eta}^{(-)} \mid_{\xi=\xi_2} = H_{2\eta}^{(+)} \mid_{\xi=\xi_2}$;

$E_{2\phi}^{(+)} \mid_{\xi=\xi_3} = \left(E_\phi^{s,2} + E_\phi^i\right) \mid_{\xi=\xi_3}$;
$H_{2\eta}^{(+)} \mid_{\xi=\xi_3} = \left(H_\eta^{s,2} + H_\eta^i\right) \mid_{\xi=\xi_3}$;

Expansion coefficients:γ_n^2; $\alpha_{2,n}^{(+)}$; $\beta_{2,n}^{(+)}$; $\alpha_{1,n}^{(-)}$ and $\beta_{1,n}^{(-)}$ will be determined by solving this system of linear equations.

6.3.3 Exact solutions

Case 1

By Applying Crammer's rule, exact solutions for expansion coefficients $\alpha_{1,n}^{(+)}$; $\beta_{1,n}^{(+)}$; $\alpha_{2,n}^{(-)}$; $\beta_{2,n}^{(-)}$, γ^1 can be retrieved as follows:

$$\alpha_{1,n}^{(+)} = \frac{R_{(-ic,i\xi_1)}^{(3)} \zeta_1 \zeta_2}{c^2 \left(\xi_3^2 + 1\right)\left(\xi_2^2 + 1\right)\Delta}, \tag{6.32}$$

$$\beta_{1,n}^{(+)} = \frac{-R_{(-ic,i\xi_1)}^{(1)} \zeta_1 \zeta_2}{c^2 \left(\xi_3^2 + 1\right)\left(\xi_2^2 + 1\right)\Delta}, \tag{6.33}$$

$$\begin{aligned}\alpha_{2,n}^{(-)} = \frac{i\zeta_2}{c\left(\xi_3^2 + 1\right)\Delta} \times \Big[\zeta_1 R_{(+ic,i\xi_2)}^{(3)} \left[A_{(-ic,i\xi_2)}^{(1)} R_{(-ic,i\xi_1)}^{(3)} - A_{(-ic,i\xi_2)}^{(3)} R_{(-ic,i\xi_1)}^{(1)}\right] \\ + \zeta_2 A_{(+ic,i\xi_2)}^{(3)} \left[R_{(-ic,i\xi_2)}^{(1)} R_{(-ic,i\xi_1)}^{(3)} - R_{(-ic,i\xi_2)}^{(3)} R_{(-ic,i\xi_1)}^{(1)}\right]\Big],\end{aligned} \tag{6.34}$$

$$\beta_{2,n}^{(-)} = \frac{i\zeta_2}{c\left(\xi_3^2+1\right)\Delta} \times \left\langle \zeta_1 R_{(+ic,i\xi_2)}^{(1)} \left[A_{(-ic,i\xi_2)}^{(1)} R_{(-ic,i\xi_1)}^{(3)} - A_{(-ic,i\xi_2)}^{(3)} R_{(-ic,i\xi_1)}^{(1)} \right] \right.$$
$$\left. + \zeta_2 A_{(+ic,i\xi_2)}^{(1)} \left[R_{(-ic,i\xi_2)}^{(1)} R_{(-ic,i\xi_1)}^{(3)} - R_{(-ic,i\xi_2)}^{(3)} R_{(-ic,i\xi_1)}^{(1)} \right] \right\rangle. \tag{6.35}$$

We assume the notations:

$\Delta_1 = \zeta_1 \left(A_{(-ic,i\xi_2)}^{(1)} R_{(-ic,i\xi_1)}^{(3)} - A_{(-ic,i\xi_2)}^{(3)} R_{(-ic,i\xi_1)}^{(1)} \right) \left(R_{(+ic,i\xi_3)}^{(1)} R_{(+ic,i\xi_2)}^{(3)} - R_{(+ic,i\xi_3)}^{(3)} R_{(+ic,i\xi_2)}^{(1)} \right) +$
$\zeta_2 \left(A_{(+ic,i\xi_2)}^{(1)} R_{(+ic,i\xi_3)}^{(3)} - A_{(+ic,i\xi_2)}^{(3)} R_{(+ic,\xi_3)}^{(1)} \right) \left(R_{(-ic,i\xi_1)}^{(1)} R_{(-ic,i\xi_2)}^{(3)} - R_{(-ic,i\xi_2)}^{(1)} R_{(-ic,i\xi_1)}^{(3)} \right)$

$\Delta_2 = \zeta_1 \left(A_{(-ic,i\xi_2)}^{(1)} R_{(-ic,i\xi_1)}^{(3)} - A_{(-ic,i\xi_2)}^{(3)} R_{(-ic,i\xi_1)}^{(1)} \right) \left(A_{(+ic,i\xi_3)}^{(1)} R_{(+ic,i\xi_2)}^{(3)} - A_{(+ic,i\xi_3)}^{(3)} R_{(+ic,i\xi_2)}^{(1)} \right)$
$+ \zeta_2 \left(A_{(+ic,i\xi_2)}^{(1)} A_{(+ic,i\xi_3)}^{(3)} - A_{(+ic,i\xi_2)}^{(3)} A_{(+ic,i\xi_3)}^{(1)} \right) \left(R_{(-ic,i\xi_1)}^{(1)} R_{(-ic,i\xi_2)}^{(3)} - R_{(-ic,i\xi_2)}^{(1)} R_{(-ic,i\xi_1)}^{(3)} \right)$

In which: $\Delta = A_{(-ic,i\xi_3)}^{(3)} \Delta_1 + R_{(-ic,i\xi_3)}^{(3)} \zeta_2 \Delta_2$. Coefficient γ can be retrieved as:

$$\gamma^1 = \frac{-\left[A_{(-ic,i\xi_3)}^{(1)} \Delta_1 + R_{(-ic,i\xi_3)}^{(1)} \zeta_2 \Delta_2 \right]}{\Delta} \tag{6.36}$$

Case 2

by applying Cramer's rule, exact solutions for expansion coefficients α_1; β_1; α_2; β_2, γ can be retrieved as follows:

$$\alpha_{1,n}^{(-)} = \frac{-R_{(+ic,i\xi_1)}^{(3)} \zeta_1 \zeta_2}{c^2\left(\xi_3^2+1\right)\left(\xi_2^2+1\right)\Delta}, \tag{6.37}$$

$$\beta_{1,n}^{(-)} = \frac{R_{(+ic,i\xi_1)}^{(1)} \zeta_1 \zeta_2}{c^2\left(\xi_3^2+1\right)\left(\xi_2^2+1\right)\Delta}, \tag{6.38}$$

$$\alpha_{2,n}^{(+)} = \frac{-i\zeta_2}{c\left(\xi_3^2+1\right)\Delta} \times \left\langle \zeta_2 A_{(-ic,i\xi_2)}^{(3)} \left[R_{(+ic,i\xi_2)}^{(3)} R_{(+ic,i\xi_1)}^{(1)} - R_{(+ic,i\xi_2)}^{(1)} R_{(+ic,i\xi_1)}^{(3)} \right] \right.$$
$$\left. - \zeta_1 R_{(-ic,i\xi_2)}^{(3)} \left[A_{(+ic,i\xi_2)}^{(1)} R_{(+ic,i\xi_1)}^{(3)} - A_{(+ic,i\xi_2)}^{(3)} R_{(+ic,i\xi_1)}^{(1)} \right] \right\rangle, \tag{6.39}$$

$$\beta_{2,n}^{(+)} = \frac{-i\zeta_2}{c\left(\xi_3^2+1\right)\Delta} \times \left\langle \zeta_2 A_{(-ic,i\xi_2)}^{(1)} \left[R_{(+ic,i\xi_2)}^{(3)} R_{(+ic,i\xi_1)}^{(1)} - R_{(+ic,i\xi_2)}^{(1)} R_{(+ic,i\xi_1)}^{(3)} \right] \right.$$
$$\left. - \zeta_1 R_{(-ic,i\xi_2)}^{(1)} \left[A_{(+ic,i\xi_2)}^{(1)} R_{(+ic,i\xi_1)}^{(3)} - A_{(+ic,i\xi_2)}^{(3)} R_{(+ic,i\xi_1)}^{(1)} \right] \right\rangle, \tag{6.40}$$

We assume the notations:

$\Delta_1 = \zeta_2 \left(A_{(-ic,i\xi_2)}^{(1)} R_{(-ic,i\xi_3)}^{(3)} - R_{(-ic,i\xi_3)}^{(1)} A_{(-ic,i\xi_2)}^{(3)} \right) \left(R_{(+ic,i\xi_1)}^{(1)} R_{(+ic,i\xi_2)}^{(3)} - R_{(+ic,i\xi_1)}^{(3)} R_{(+ic,i\xi_2)}^{(1)} \right)$

$+\zeta_1\left(A^{(1)}_{(+ic,i\xi_2)}R^{(3)}_{(+ic,i\xi_1)}-A^{(3)}_{(+ic,i\xi_2)}R^{(1)}_{(+ic,i\xi_1)}\right)\left(R^{(1)}_{(-ic,i\xi_3)}R^{(3)}_{(-ic,i\xi_2)}-R^{(3)}_{(-ic,i\xi_3)}R^{(1)}_{(-ic,i\xi_2)}\right)$

$\Delta_2=\zeta_2\left(A^{(1)}_{(-ic,i\xi_2)}A^{(3)}_{(-ic,i\xi_3)}-A^{(1)}_{(-ic,i\xi_3)}A^{(3)}_{(-ic,i\xi_2)}\right)\left(R^{(1)}_{(+ic,i\xi_1)}R^{(3)}_{(+ic,i\xi_2)}-R^{(1)}_{(+ic,i\xi_2)}R^{(3)}_{(+ic,i\xi_1)}\right)$

$+\zeta_1\left(A^{(1)}_{(-ic,i\xi_3)}R^{(3)}_{(-ic,i\xi_2)}-A^{(3)}_{(-ic,i\xi_3)}R^{(1)}_{(-ic,i\xi_2)}\right)\left(A^{(1)}_{(+ic,i\xi_2)}R^{(3)}_{(+ic,i\xi_1)}-A^{(3)}_{(+ic,i\xi_2)}R^{(1)}_{(+ic,i\xi_1)}\right)$ in which $\Delta=A^{(3)}_{(-ic,i\xi_3)}\Delta_1-R^{(3)}_{(-ic,i\xi_3)}\zeta_2\Delta_2$. Coefficient γ^2 can be retrieved as:

$$\gamma^2=\frac{-\left[A^{(1)}_{(-ic,i\xi_3)}\Delta_1+R^{(1)}_{(-ic,i\xi_3)}\zeta_2\Delta_2\right]}{\Delta} \tag{6.41}$$

6.3.4 Numerical results

All the simulations are done with the parameters of: $d=2$; $\lambda=1$; $\xi_0=1.5$; $\xi_1=0.25$; $\xi_2=0.5$ and $\xi_3=0.6$.

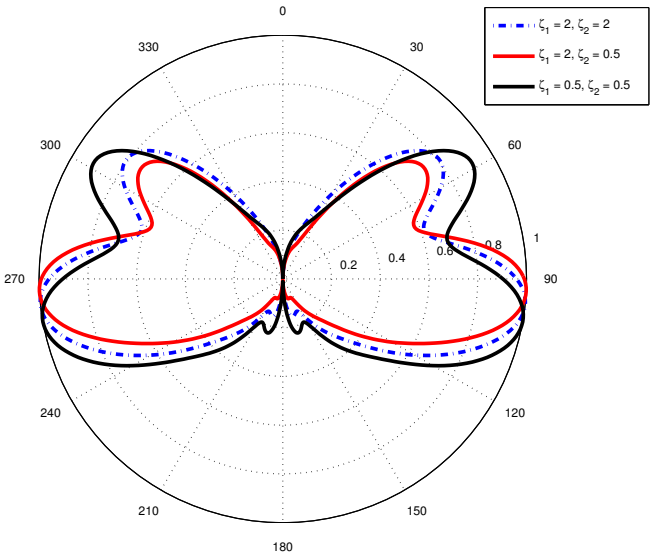

Figure 6.8: *The Scattered Electric far field of Magnetic Dipole when Layer 1 is Isorefractive and Layer 2 is Anti-Isorefractive with different* ζ_1, ζ_2

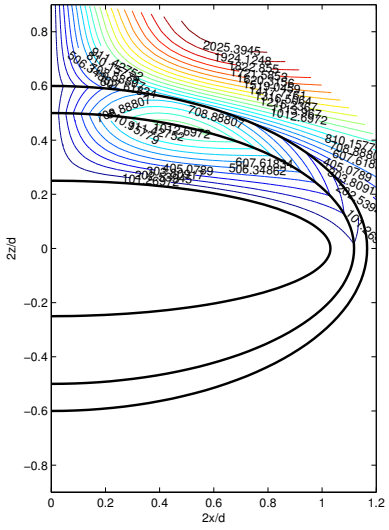

Figure 6.9: *Contour Plot of Electric field of Magnetic Dipole in the case layer 1 is Isorefractive and layer 2 is Anti-Isorefractive with* $\zeta_1 = 2$, $\zeta_2 = 2$

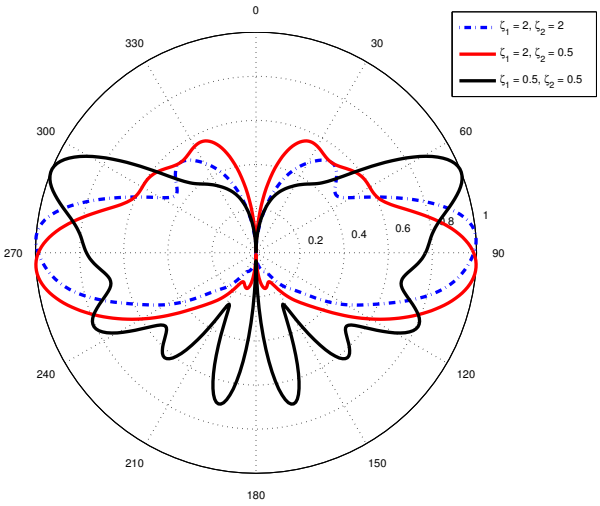

Figure 6.10: *The Scattered Electric far field of Magnetic Dipole when layer 1 is Anti-Isorefractive and layer 2 is Isorefractive with different* ζ_1, ζ_2

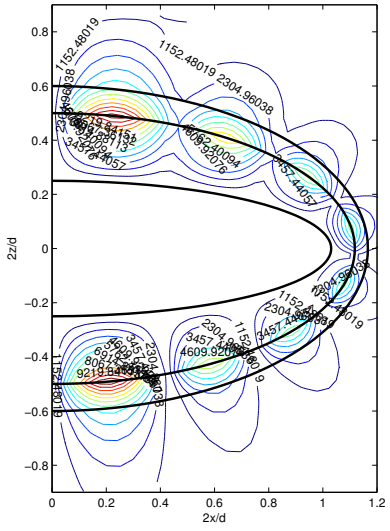

Figure 6.11: *Contour Plot of Electric field of Magnetic Dipole in the case layer 1 is Isorefractive and layer 2 is Anti-Isorefractive with* $\zeta_1 = 0.5$, $\zeta_2 = 0.5$

Conclusion

The aim of this thesis is to derive a fast and optimized solution for *Electromagnetic drive* by using *Computational Intelligence* techniques, which comprises evolutionary algorithms and Artificial Neural Network. A number of Electromagnetic components such as microstrip antennas and spatial filters have been optimized by successfully linking the global optimizer with commercial full-wave simulator. In the first part of my thesis, Electromagnetic problems have been seen in the viewpoint of *Computer Science*, which means every object is treated as arbitrary input-output system. The Electromagnetic fields were calculated by being properly modeled in available simulator. Afterwards, with the aim of reducing computational efforts, a new optimization mechanism has been implemented by the use of Artificial Neural Network (ANN). As an approximation model, a proper ANN can replace the full-wave analysis and this approach shows a good potential for application in large-scale problems. The results of this specific research activities have been published in some *IEEE* conferences and *Progress in Electromagnetic Research* (PIER) journal.

In the second part, the problems of radiation by axially oriented antennas in the presence of spheroidal structures were solved. Even though coated spheroids have been studied for many years, the new solutions enrich the catalog of exact analytical solutions for Electromagnetic boundary-value problems. The results can also be used to test and validate numerical codes developed for the numerical analysis of penetrable structures. At this point, Electromagnetic scattering problems can be constructed and Electromagnetic fields can be computed by series of special functions. The physical characterization by separations of variables was again employed to optimize scattered far field of multiple dipoles axially located

on the symmetry axis of prolate spheroids. The results of this specific research activities have been published in URSI general meeting and in preparation for submitting in *IEEE Transactions* on Antenna and Propagation.

Contributions

NAME: Linh Ho Manh

EDUCATION: B.S. eq., Hanoi University of Science and Technology,
Ha Noi, Vietnam, 2006-2011
PhD studentship at Politecnico di Milano, 2011-2014,
PhD internship student, University of Illinois at Chicago, 2014

EXPERIENCE: Teaching Assistant in "The principles of Electrical Engineering",
Politecnico di Milano
Research assistant,
University of Illinois at Chicago,
December 2013 to September 2014.

CONFERENCE PAPERS:

1) Linh H.M, M.Mussetta, P.Pirinoli, F.Grimaccia, R.E.Zich
Modeling of reflectarray elements by means of MetaPSO-based Artificial Neural Network,
7th European Conference on Antennas and Propagation
Gothenburg, Sweden, 8-12 April 2013

2) Linh H.M, M.Mussetta, F.Grimaccia, R.E.Zich
Differentiated Meta-PSO for rectangular ring antenna with proximity-coupled feed,
2013 IEEE International APS and URSI meeting
Orlando, Florida, July 7-13,2013.

3) Linh H.M, M.Mussetta, F.Grimaccia, Riccardo Zich

Multi-layer Antenna Design with Evolutionary Optimization
2013 IEEE International Conference on Electromagnetics
in Advanced Applications, Sept. 2013, Torino, Italy
4) Linh H.M, M.Mussetta, P.Pirinoli, F.Grimaccia, R.E.Zich
Antenna optimization based on Artificial Neural Network
8th European Conference on Antennas and Propagation
5) Linh H.M, M.Mussetta, F.Grimaccia, R.E.Zich
Neural Network Training Schemes for Antenna Optimization
2014 IEEE International APS and URSI meeting
Memphis, Tennessee, July 6-11,2014.
6) Piergiorgio L.E. Uslenghi, Linh H.M, Riccardo E.Zich
Exact Radiation from Dipole Antennas on Prolate and Oblate Spheroids Coated with Two Confocal Layers of Different Materials,
XXXI General Assembly and Scientific Symposium of the
International Union of Radio Science, Beijing, August 17-23,2014.
7) Linh H.M, M.Mussetta, P.Pirinoli, F.Grimaccia, R.E.Zich
Multi-Net ANN approach for improving antenna optimization,
XXXI URSI-GASS 2014, Beijing
8) Linh H.M, M.Mussetta, P.Pirinoli, F.Grimaccia, R.E.Zich
Splitted Neural Networks for better ,
performance of antenna optimization,
The 2014 International Joint Conference on
Neural Networks (IJCNN), Beijing, July 6-11,2014.
9) Linh H.M, M.Mussetta, R.E.Zich
Evolutionary Algorithm for Bandstop Frequency Selective Surface,
Fifth International Conference on Communications
and Electronics (ICCE), 2014 Danang, July 30- August 1,2014.

JOURNAL PAPERS: Linh H.M, P. L. E. Uslenghi, R.E.Zich
Exact Radiation From Dipole Antennas on Doubly-Coated Spheroids
IEEE Transactions on Antennas and Propagation,
in preparation, October 2014.
Linh H.M, Danilo Erricolo, P. L. E. Uslenghi, R.E.Zich
Exact Scattering From Plane Wave on Doubly-Coated Elliptical Cylinders
IEEE Transactions on Antennas and Propagation,
in preparation, October 2014.
Linh H.M, M.Mussetta, F.Grimaccia, R.E.Zich
Optimization of a dual ring antenna by means of

Artificial Neural Network,
Progress In Electromagnetics Research B
Vol. 58, 59-69, 2014.

HONORS: International mobility grant, 2014

MEMBERSHIPS: IEEE Antenna and Propagation society.

Bibliography

[1] A.Torn, A.Zilinskas. *Global Optimization*. New York: Springer-Verlag, 1989 vol.350, Lecture Notes in Computer Science.

[2] Kuwahara, Y. "Multiobjective optimization design of Yagi-Uda antenna," *IEEE Transactions on Antennas and Propagation*, vol.53, no.6, pp.1984,1992, June 2005

[3] Cui, S.; Mohan, A.; Weile, Daniel S. "Pareto optimal design of absorbers using a parallel elitist nondominated sorting genetic algorithm and the finite element-boundary integral method," *IEEE Transactions on Antennas and Propagation*, vol.53, no.6, pp.2099,2107, June 2005

[4] Fonseca, C.M.; Fleming, P.J.. "Multiobjective optimization and multiple constraint handling with evolutionary algorithms. I. A unified formulation" *IEEE Transactions on Systems, Man and Cybernetics, Part A: Systems and Humans*, vol.28, no.1, pp.26,37, Jan 1998

[5] Fonseca, C.M.; Fleming, P.J.. "Multiobjective optimization and multiple constraint handling with evolutionary algorithms. II. Application example" *IEEE Transactions on Systems, Man and Cybernetics, Part A: Systems and Humans*, vol.28, no.1, pp.38-47, Jan 1998

[6] Thomas Back; Hans-Paul Schwefel. "An overview of evolutionary algorithms for parameter optimization" *Evol. Comput. 1*, vol.1, pp.1-23, March 1993

[7] Wolpert, D.H.; Macready, W.G. "No free lunch theorems for optimization," *IEEE Transactions on Evolutionary Computation*, vol.1, no.1, pp.67-82, April 1997

[8] J.Kenedy and R.Eberhart. "Particle Swarm Optimization" *, International Conference on Neural Network*, pp.1942-1948, 1995

[9] J.Kenedy. "The Particle Swarm: Social adaption of knowledge" *, International Conference on Evolutionary Computation*, Idianapolis, IN, April 1997, pp 303-308

[10] J.Kenedy; R.C.Eberhart. "Swarm Intelligence" *, San Francisco, CA: Morgan Kaufmann*, 2011.

[11] Clerc, M.; Kennedy, J. "The particle swarm - explosion, stability, and convergence in a multidimensional complex space," *IEEE Transactions on Evolutionary Computation*, vol.6, no.1, pp.58-73, Feb 2002

[12] Ciuprina, G.; Ioan, D.; Munteanu, I. "Use of intelligent-particle swarm optimization in electromagnetics," *IEEE Transactions on Magnetics*, vol.38, no.2, pp.1037-1040, Mar 2002

[13] Gies, D.; Rahmat-Samii, Y.. "Reconfigurable array design using parallel particle swarm optimization," *, IEEE Antennas and Propagation Society International Symposium, 2003*, vol.1, pp.177-180 vol.1, June 2003

[14] Boeringer, D.W.; Werner, D.H. "Particle swarm optimization versus genetic algorithms for phased array synthesis," *IEEE Transactions on Antennas and Propagation*, vol.52, no.3, pp.771-779, March 2004

[15] Robinson, J.; Rahmat-Samii, Y. "Particle swarm optimization in electromagnetics," *IEEE Transactions on Antennas and Propagation*, vol.52, no.2, pp.397,407, Feb. 2004

[16] Matekovits, L.; Mussetta, M.; Pirinoli, P.; Selleri, S.; Zich, R.E.. "Particle swarm optimization of microwave microstrip filters," *, IEEE Antennas and Propagation Society International Symposium, 2004*, vol.3, pp.2731-2734 June 2004

[17] R.J.W.Hodgson "Particle swarm optimization applied to the atomic cluster optimization problem" *, Proc. Genetic and Evolutionay Computation Conference*, pp.68-73 Feb 2004

[18] Nanbo Jin; Rahmat-Samii, Y. "Parallel particle swarm optimization and finite- difference time-domain (PSO/FDTD) algorithm for multiband and

wide-band patch antenna designs," *IEEE Transactions on Antennas and Propagation*, vol.53, no.11, pp.3459-3468, Nov. 2005

[19] Cui, S.; Weile, Daniel S. "Application of a parallel particle swarm optimization scheme to the design of electromagnetic absorbers," *IEEE Transactions on Antennas and Propagation*, vol.53, no.11, pp.3616-3624, Nov. 2005

[20] J.Kenedy "Stereotyping: Improving particle swarm performance with cluster analysis," *, Proc. Evolutionay Computation Conference*, pp.1931-1938 DC July 1999

[21] Gies, D.; Rahmat-Samii, Y.. "Vector evaluated particle swarm optimization (VEPSO): optimization of a radiometer array antenna," *, IEEE Antennas and Propagation Society International Symposium, 2004*, pp.2297-2300 June 2004

[22] Boeringer, D.W.; Werner, D.H. "Efficiency-Constrained Particle Swarm Optimization of a Modified Bernstein Polynomial for Conformal Array Excitation Amplitude Synthesis," *IEEE Transactions on Antennas and Propagation*, vol.53, no.8, pp.2662-2673, Aug 2005

[23] Khodier, M.M.; Christodoulou, C.G. "Linear Array Geometry Synthesis With Minimum Sidelobe Level and Null Control Using Particle Swarm Optimization," *IEEE Transactions on Antennas and Propagation*, vol.53, no.8, pp.2674-2679, Aug. 2005

[24] Eberhart, R.C.; Yuhui Shi "Particle swarm optimization: developments, applications and resources," *, Proceedings of the 2001 Congress on Evolutionary Computation*, pp.81-86, vol. 1, 2001

[25] Haupt, Randy L. "An introduction to genetic algorithms for electromagnetics," *IEEE Antennas and Propagation Magazine*, vol.37, no.2, pp.7-15, Apr 1995

[26] Y.Rahmat-Samii and E.Michielsen. *Electromagnetic Optimization by Genetic Algorithms*. New York: Wiley, 1999

[27] Ku, K.W.C.; Mak, M.W. "Exploring the effects of Lamarckian and Baldwinian learning in evolving recurrent neural networks," *, IEEE International Conference on Evolutionary Computation*, pp.617-621 Apr 1997

[28] Krasnogor, N.; Smith, J. "A tutorial for competent memetic algorithms: model, taxonomy, and design issues," *IEEE Transactions on Evolutionary Computation*, vol.9, no.5, pp.474-488, Oct 2005

[29] Randy L.Haupt and Sue Ellen Haupt. *Practical Genetic Algorithm*. John Wiley and Sons, 2004

[30] Robinson, J.; Sinton, S.; Rahmat-Samii, Y.. "Particle swarm, genetic algorithm, and their hybrids: optimization of a profiled corrugated horn antenna," *, IEEE Antennas and Propagation Society International Symposium, 2002*, vol.1, pp.314-317 2002

[31] Chia-Feng Juang "A hybrid of genetic algorithm and particle swarm optimization for recurrent network design," *IEEE Transactions on Systems, Man, and Cybernetics, Part B: Cybernetics*, vol.34, no.2, pp.997-1006, April 2004

[32] Gandelli, A.; Grimaccia, F.; Mussetta, M.; Pirinoli, P.; Zich, R.E. "Development and validation of different hybridization strategies between GA and PSO," *, IEEE International Conference on Evolutionary Computation*, pp.617-621 Apr 1997

[33] Grimaccia, F.; Mussetta, M.; Zich, R.E. "Genetical Swarm Optimization: Self-Adaptive Hybrid Evolutionary Algorithm for Electromagnetics," *IEEE Congress on Evolutionary Computation, CEC 2007*, pp.2782, 25-28 Sept. 2007

[34] Van den Bergh, F.; Engelbrecht, A.P. "A Cooperative approach to particle swarm optimization," *IEEE Transactions on Evolutionary Computation*, vol.8, no.3, pp.225,239, June 2004

[35] Kennedy, J. "Small worlds and mega-minds: effects of neighborhood topology on particle swarm performance," *, Proceedings of the 1999 Congress on Evolutionary Computation*, vol.3, pp.,1938

[36] Yuhui Shi; Krohling, R.A. "Co-evolutionary particle swarm optimization to solve min-max problems," *, Proceedings of the 2002 Congress on Evolutionary Computation*, vol.2, no., pp.1682-1687

[37] Selleri, S.; Mussetta, M.; Pirinoli, P.; Zich, R.E.; Matekovits, L. "Differentiated Meta-PSO Methods for Array Optimization," *IEEE Transactions on Antennas and Propagation*, vol.56, no.1, pp.67,75, Jan 2008

[38] Selleri, S.; Mussetta, M.; Pirinoli, P.; Zich, R.E.; Matekovits, L. "Some Insight Over New Variations of the Particle Swarm Optimization Method," *IEEE Antennas and Wireless Propagation Letters*, vol.5, no.1, pp.235-238, Dec 2006

[39] Ben Krose, Patrick van der Smagt. *Fundamentals of Neural Network*. Eight Edition, Nov 1996

[40] Mark Hudson Beale, Martin T.Hagan and Howard B.Demith. *Neural Network Toolbox User's Guide*. MATLAB R2014a

[41] M. Luo and K.-M. Huang, "Prediction of the electromagnetic field in metallic enclosures using artificial neural networks," Progress In Electromagnetics Research, Vol. 116, 171–184, 2011.

[42] Y. Zhang and L. Wu, "Weights optimization of neural network via improved BCO approach," Progress In Electromagnetics Research, Vol. 83, 185–198, 2008.

[43] Nesil, S.; Gunes, F.; Ozkaya, U., "Phase characterization of a reflectarray unit cell with Minkowski shape radiating element using Multilayer Perceptron Neural Network," Electrical and Electronics Engineering (ELECO), 2011 7th International Conference on , vol., no., pp. II-219,II-222, 1–4 Dec. 2011.

[44] Robustillo, P.; Encinar, J.A.; Zapata, J., "ANN element characterization for reflectarray antenna optimization," Antennas and Propagation (EUCAP), Proceedings of the 5th European Conference on , vol., no., pp. 957–960, 11–15 April 2011.

[45] E. Bermani, S. Caorsi and M. Raffetto, "An inverse scattering approach based on a neural network technique for the detection of dielectric cylinders buried in a lossy half-space," Progress In Electromagnetics Research, Vol. 26, 67–87, 2000.

[46] Caputo, D.; Pirisi, A.; Mussetta, M.; Freni, A.; Pirinoli, P.; Zich, R.E., "Neural Network characterization of microstrip patches for reflectarray optimization," 3rd European Conference on Antennas and Propagation, EuCAP 2009. pp.2520-2522, 23-27 March 2009.

[47] Washington, G., "Aperture antenna shape prediction by feedforward neural networks," Antennas and Propagation, IEEE Transactions on , vol.45, no.4, pp. 683–688, Apr 1997.

[48] P. Thiruvalar Selvan and S. Raghavan, "Neural model for circular-shaped microshield and conductor-backed coplanar waveguide," Progress In Electromagnetics Research M, Vol. 8, 119–129, 2009.

[49] De Vita, P.; De Vita, F.; Di Maria, A.; Freni, A., "An Efficient Technique for the Analysis of Large Multilayered Printed Arrays," Antennas and Wireless Propagation Letters, IEEE , vol.8, no., pp. 104–107, 2009.

[50] Hao Yu and B. M. Wilamowski, "Levenberg–Marquardt Training" Industrial Electronics Handbook, vol. 5 – Intelligent Systems, 2nd Edition, chapter 12, pp. 12-1 to 12-15, CRC Press 2011.

[51] S.-W. Cho and J.-H. Lee, "Efficient implementation of the capon beamforming using the levenberg-marquardt scheme for two dimensional aoa estimation," Progress In Electromagnetics Research, Vol. 137, 19–34, 2013.

[52] Mussetta, M.; Pirinoli, P.; Selleri, S.; Zich, R.E., "Meta-PSO techniques for multi-objective optimization of non-uniform planar arrays," International Symposium on Antennas and Propagation Society, APSURSI '09, pp.1,4, 1-5 June 2009

[53] Mussetta, M.; Pirinoli, P.; Selleri, S.; Zich, R.E., "Multi-objective Meta-PSO techniques for optimization of antenna arrays," 3rd European Conference on Antennas and Propagation, EuCAP 2009. pp.503-505, 23-27 March 2009.

[54] Mussetta, M.; Pirinoli, P.; Selleri, S.; Zich, R.E., "Development and validation of differentiated and undifferentiated Meta-PSO Techniques for electromagnetics," IEEE Congress on Evolutionary Computation, CEC 2008 (IEEE World Congress on Computational Intelligence), pp.3833,3836, 1-6 June 2008

[55] Grimaccia, F.; Mussetta, M.; Pirinoli, P.; Zich, R.E., "Genetical Swarm Optimization (GSO): a class of Population-based Algorithms for Antenna Design," First International Conference on Communications and Electronics, ICCE '06, pp.467-471, 10-11 Oct. 2006

[56] Grimaccia, F.; Mussetta, M.; Pirinoli, P.; Zich, R.E., "Optimization of a reflectarray antenna via hybrid evolutionary algorithms," 17th International Zurich Symposium on Electromagnetic Compatibility, EMC-Zurich 2006., pp.254-257, Feb. 27 -March 3, 2006

[57] Alfassio Grimaldi, E.; Grimaccia, F.; Mussetta, M.; Pirinoli, P.; Zich, R.E., "A new hybrid genetical-swarm algorithm for electromagnetic optimization," 3rd International Conference on Computational Electromagnetics and Its Applications, ICCEA 2004, pp.157-160, 1-4 Nov. 2004

[58] David M.Pozar. *Microwave Engineering*. Second Edition, John Wiley & Sons, 1998

[59] Constantine A. Balanis. *Advanced engineering electromagnetics*. Second Edition, John Wiley & Sons

[60] Constantine A. Balanis. *Antenna theory analysis and designs*. Third Edition, John Wiley & Sons

[61] Derneryd Anders G.. "A theoretical investigation of the rectangular microstrip antenna element," *, IEEE Transactions on Antennas and Propagation*, vol.26, no.4, pp.532-535, Jul 1978

[62] Carver, Keith R.; Mink, J.. "Microstrip antenna technology," *, IEEE Transactions on Antennas and Propagation*, vol.29, no.1, pp.2-24, Jan 1981

[63] Lo, Y.T.; Solomon, D.; Richards, W. "Theory and experiment on microstrip antennas," *, IEEE Transactions on Antennas and Propagation*, vol.27, no.2, pp.137-145, Mar 1979

[64] Ben A.Munk. *Frequency Selective Surfaces Theory and Design*. John Wiley & Sons

[65] Basaran, S.C.; Olgun, U.; Sertel, K., "Multiband monopole antenna with complementary split-ring resonators for WLAN and WiMAX applications," Electronics Letters , vol.49, no.10, pp.636,638, May 9 2013

[66] Rahmat-Samii, Y., "Metamaterials in Antenna Applications: Classifications, Designs and Applications," Antenna Technology Small Antennas and Novel Metamaterials, 2006 IEEE International Workshop on , vol., no., pp.1,4, March 6-8, 2006

[67] Hashemi, M.R.M.; Itoh, T., "Coupled Composite Right/Left-Handed Leaky-Wave Transmission Lines Based on Common/Differential-Mode Analysis," Microwave Theory and Techniques, IEEE Transactions on , vol.58, no.12, pp.3645,3656, Dec. 2010

[68] Si, L.-M.; Zhu, W.; Sun, H.-J., "A Compact, Planar, and CPW-Fed Metamaterial-Inspired Dual-Band Antenna," Antennas and Wireless Propagation Letters, IEEE , vol.12, no., pp.305,308, 2013

[69] Lai, Anthony; Leong, K. M K H; Itoh, T., "Infinite Wavelength Resonant Antennas With Monopolar Radiation Pattern Based on Periodic Structures," Antennas and Propagation, IEEE Transactions on , vol.55, no.3, pp.868,876, March 2007

[70] Hien Ba Chu; Shirai, H.; Chien Ngoc Dao, "High efficiency small antenna for WLAN application," Antennas and Propagation in Wireless Communications (APWC), 2013 IEEE-APS Topical Conference on , vol., no., pp.757,760, 9-13 Sept. 2013

[71] Jun Kamiya; Kenichi Shirota; Takahiro Yagi; Tetsuo Nakazawa, "Study of EBG Structures using Metamaterial Technology", OKI Technical Review April 20 2/ Issue 2 9 Vol. 79

[72] Bing-Jian Niu; Quan-Yuan Feng, "Bandwidth Enhancement of Asymmetric Coplanar Waveguide (ACPW)-Fed Antenna Based on Composite Right/Left-Handed Transmission Line," Antennas and Wireless Propagation Letters, IEEE , vol.12, no., pp.563,566, 2013.

[73] Ho Manh Linh; Mussetta, M.; Grimaccia, F.; Zich, R.E., "Optimization of Dual ring antenna by means of artificial neural network," *Progress In Electromagnetics Research*, 2014.

[74] V. G. Veselago. "The electrodynamics of substances with simultaneously negative values of ϵ and μ" *Sov. Phys.-Usp.*, vol 10, pp 509-514, 1968.

[75] Shelby, R. A.; Smith, D.R.; Nemat-Nasser, S.C. and Schultz, S.. "Microwave transmission through a two-dimensional, isotropic, left-handed metamaterial" *Applied Physics Letters*, vol. 78, pp 489-491, 2001.

[76] Engheta, N.. "An idea for thin subwavelength cavity resonators using metamaterials with negative permittivity and permeability" *Antennas and Wireless Propagation Letters, IEEE*, vol. 1, pp 10-13, 2002.

[77] Arslanagic S.; Ziolkowski R.W and Breinbjerg O.. "Analytical and numerical investigation of the radiation from concentric metamaterial spheres excited by an electric line source" *Radio Science*, vol. 42, p.RS6S15, Nov.-Dec.2007, 10.1029/2007RS003644

[78] Arslanagic S.; Ziolkowski R.W and Breinbjerg O.. "Analytical and numerical investigation of the radiation from concentric metamaterial spheres excited by an electric Hertzian dipole" *Radio Science*, vol. 42, p.RS6S16, Nov.-Dec.2007, 10.1029/2007RS003663

[79] Carson Flammer. *Spheroidal Wave Functions*. Stanford University Press, 1957.

[80] J. A Stratton, P. M. Morse, L. J. Chu and R. A Hunter. *Elliptic Cylinder and Spheroidal Wave Functions*. John Wiley and Sons, Inc.-New York, 1941.

[81] J. A Stratton, P. M. Morse, L. J. Chu, J. D. C. Little and F. J. Corbató. *Spheroidal Wave Functions*. John Wiley and Sons, Inc.-New York, 1956.

[82] Le Wei Li, Xiao Kang Kang and Mook Seng Leong. *Spheroidal Wave Functions in Electromagnetic Theory*. John Wiley and Sons, Inc.-New York, 2002.

[83] S. Zhang, J. M. Jin. *Computation of Special Functions*. John Wiley and Sons, Inc.-New York, 1996.

[84] J. J. Bowman and T. B. A. Senior and P. L. E. Uslenghi. *Electromagnetic and Acoustic Scattering by simple shapes*. North-Holland Publishing Company - Amsterdam, 1969.

[85] Uslenghi Piergiorgio L.E. "Exact scattering by isorefractive bodies" *, IEEE Transactions on Antennas and Propagation*, vol 45, pp. 1382-1385, 1997.

[86] Roy, S.; Uslenghi, P. L E. "Exact scattering for axial incidence on an isorefractive paraboloid," *, IEEE Transactions on Antennas and Propagation*, vol 45, pp 1563, Oct 1997.

[87] Uslenghi, P. L E; Zich, R.E.. "Radiation and scattering from isorefractive bodies of revolution," *, IEEE Transactions on Antennas and Propagation*, vol 46, pp. 1606-1611, Nov 1998.

[88] Daniele, V.G.; Uslenghi, P. L E. "Closed-form solution for a line source at the edge of an isorefractive wedge," *, IEEE Transactions on Antennas and Propagation*, vol 47, no 4, pp. 764-765, Apr 1998.

[89] Uslenghi, P. L E. "Exact penetration, radiation, and scattering for a slotted semielliptical channel filled with isorefractive material," *, IEEE Transactions on Antennas and Propagation*, vol 52, pp. 1473-1480, Jun 2004.

[90] Berardi, C.; Erricolo, D.; Uslenghi, P. L E. "Exact dipole radiation for an oblate spheroidal cavity filled with isorefractive material and aperture-coupled to a half space," *, IEEE Transactions on Antennas and Propagation*, vol 52, pp. 2205-2213, Sep 2004.

[91] Jing Liang; Uslenghi, P. L E. "Exact Scattering by Isorefractive Paraboloidal Radomes," *, IEEE Transactions on Antennas and Propagation*, vol 55, no 6, pp. 1546-1553, Jun 2007

[92] Akgol, O.; Erricolo, D.; Uslenghi, P. L E; Monopoli, D.; Zich, R.E.. "Electromagnetic scattering by an elliptic DNG metamaterial cylinder," , *International Conference on Electromagnetics in Advanced Applications, 2009(ICEAA '09)*, pp.833-836 , Sep 14-18 2009

[93] Akgol, O.; Erricolo, D.; Uslenghi, P. L E. "Electromagnetic scattering by a semielliptical trench filled with DNG metamaterial," *, International Conference on Electromagnetics in Advanced Applications, 2009(ICEAA '09)*, pp.1034-1037, Sep 14-18 2009

[94] Akgol, O.; Erricolo, D.; Uslenghi, P. L E. "Radiation of a line source by a slotted semielliptical trench filled with DNG metamaterial," *, IEEE International Symposium on Microwave, Antenna, Propagation and EMC Technologies for Wireless Communications, 2009 3rd* , pp.107-110, Oct 2009

[95] Jing Liang; Uslenghi, P. L E. "A paraboloidal lens made of double-negative material" *, Radio Science*, vol 42, p. RS6S14, Nov-Dec 2007, 10.1029/2007RS003701.

[96] Askarpour, A.N.; Uslenghi, P. L E. "Radiation from an electric dipole axially mounted above a spheroidal cavity filled with DNG metamaterial," *URSI International Symposium on Electromagnetic Theory (EMTS)*, pp. 918-921, 16-19 Aug 2010.

[97] Askarpour, A.N.; Uslenghi, P. L E. "Exact Dipole Radiation From an Oblate Semi-Spheroidal Cavity Filled With DNG Metamaterial," *IEEE Transactions on Antennas and Propagation*, vol.59, no.7, pp. 2473-2479, Jul 2011

[98] A.N. Askarpour and P.L.E. Uslenghi, "Exact Radiation From Dipole Antennas on Prolate Spheroids Coated With Isorefractive and Anti-Isorefractive Layers," *IEEE Trans. Antennas and Propag.*, vol.60, no.4, pp.2129-2133, Apr. 2012

[99] A.N. Askarpour and P.L.E. Uslenghi, "Exact Radiation From Dipole Antennas on Oblate Spheroids Coated With Isorefractive and Anti-Isorefractive Layers," *IEEE Trans. Antennas and Propag.*, vol.60, no.11, pp.5476-5479 Nov. 2012.

[100] P.L.E. Uslenghi, "Exact radiation from an antenna on an oblate metallic spheroid coated with layers of isorefractive and anti-isorefractive materials," Abstract in: *Days on Diffraction.* St.Petersburg, Russia, Jun. 2010